Dipartimento di Scienze della Terra e dell’Ambiente

Direttore: Prof. S. Seno

Laurea Magistrale in Geoscienze per lo Sviluppo Sostenibile

Hollows in Warhol, Hopper, Eminescu and Sander craters: a comparison of extended Hollow fields on crater floors

Relatore: Prof. Francesco ZUCCA
Co-relatore: Prof. Cristian CARLI

Tesi di Laurea Magistrale
In Geoscienze per lo Sviluppo Sostenibile

di FEDERICO CARMINATI

Matricola: 547612

Anno Accademico: 2024/25

Sommario

1. Introduction

In our Solar System, there are four terrestrial planets, primarily composed of silicate rocks and metals, among which there is Mercury, the smallest and closest to the Sun. Mercury is a little more than a third the width of the Earth, with a diameter of 4879,4 km. Mercury is 0,4 astronomical units away from the Sun and about 1,15 astronomical units away from the Earth. The planet's position places Mercury in an extreme thermal and gravitational environment. For this reason, the scientific community has long classified Mercury as a planet lacking in volatile elements and rich in refractory and metallic components. High temperatures near the Sun were thought to have prevented the condensation and retention of low boiling point elements. These peculiar characteristics distinguish Mercury from all other terrestrial planets.

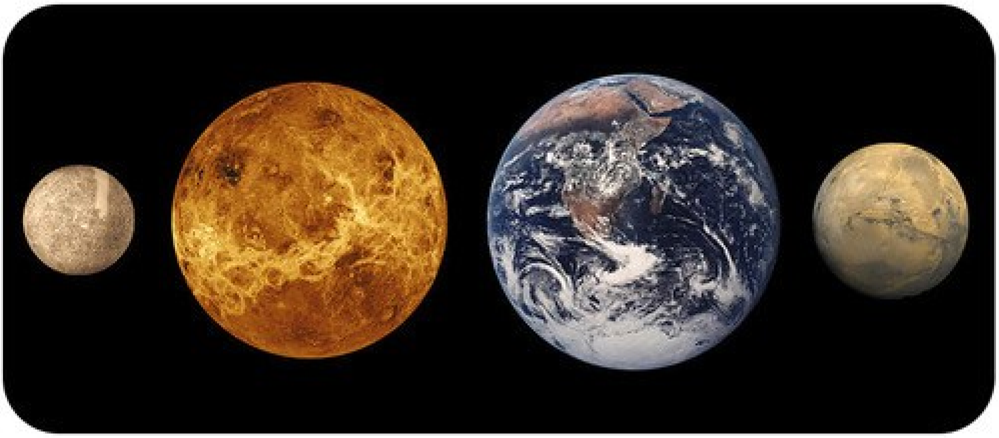

Fig. 1: The inner planets, or terrestrial planets, are the four planets closest to the Sun: Mercury, Venus, Earth, and Mars with the relative sizes of these four inner planets. Image from: https://courses.lumenlearning.com/suny-earthscience/chapter/inner-planets/.

Mercury has a relatively high mean density of 5,43 g cm^{-3}, which suggests that the planet has a large metallic core compared to silicate mantle and crust. It is also characterised by the presence of a magnetic field, indicating a partially molten metallic core (McCoy & Nittler, 2014).

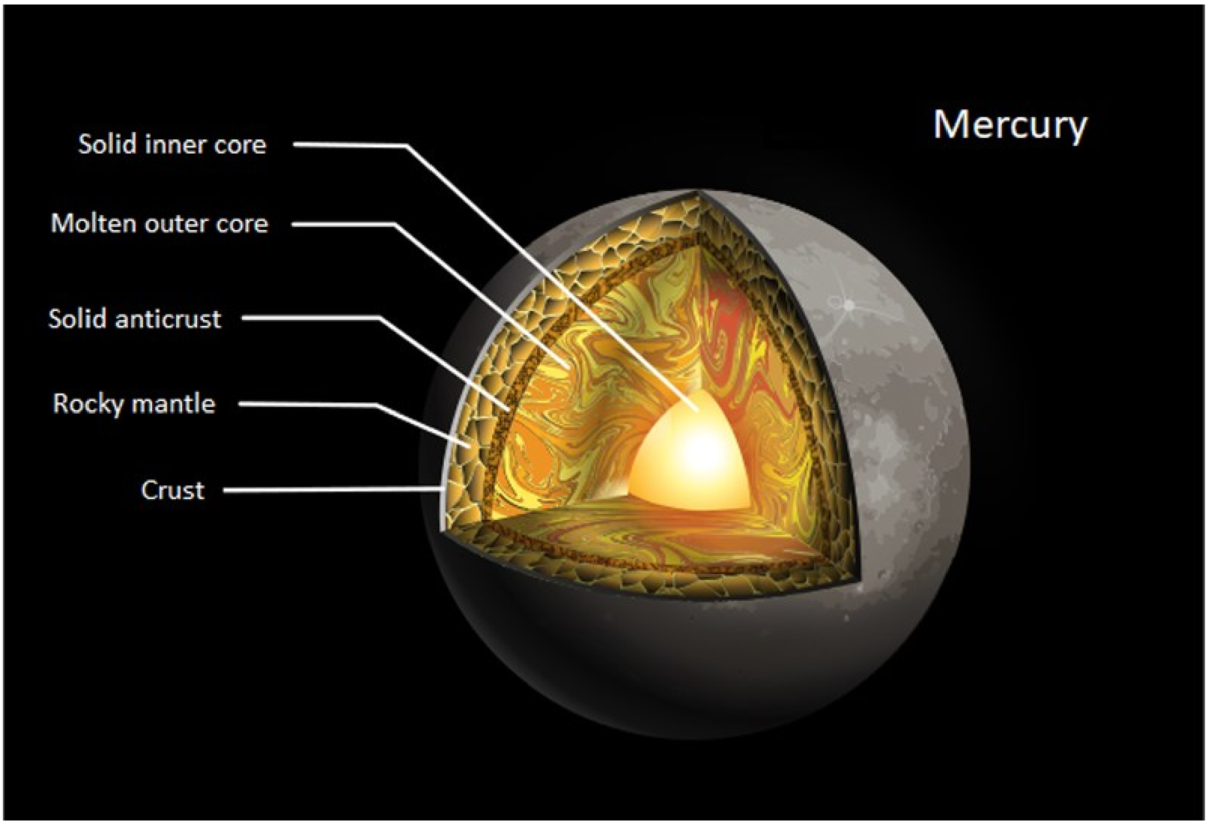

Fig. 2: Representation of the inner structure of Mercury. Image from: https://britastro.org/2021/mercury-the-iron-planet

Mercury's surface is heavily cratered with a variety of smooth plain deposit that could either have a volcanic or impact-melt origin (McCoy & Nittler, 2014). Mercury's surface also shows a variety of smooth plain deposits about whose origin there has been extensive debate in the scientific community. Among the most accredited hypotheses, the first one confers a volcanic origin to Mercury's smooth plain deposits while the second one validates that these smooth plains have an impact-melt origin (Head et al., 2008; Dzurisin, 1978; Hapke et al., 1980; Keiffer & Murray, 1987; Murray, 1975; Murray et al., 1975). Radar observations and early reflectance spectroscopy data suggested a low surface content in FeO, implying a formation scenario involving high-temperature differentiation or catastrophic mantle stripping (Benz et al., 1988; Cameron et al., 1988; Wetherill, 1988).

As the nearest planet to the Sun, the most difficult to observe from Earth, and for its differences from other terrestrial planets, Mercury has always raised great interest. The origin of Mercury is one of the most largely theorised arguments for which several models were developed. Models for Mercury's origin developed before direct spacecraft exploration of the planet considered a variety of mechanisms: great impacts removing silicate material, preferential condensation of metal-rich materials in a hot Solar nebula, accretion from ultra refractory components such as Bencubbin-like or enstatite chondrites are some examples (Taylor & Scott, 2023; Wasson, 1988). Many of these hypotheses predicted that Mercury should be rich in refractory elements (such as Al, Ca, Th) and depleted in volatile elements (such as S, Na, K and Cl). It is possible to divide all models in four main classes (McCoy & Nittler, 2014).

The surface of Mercury is composed of highly reduced volcanic igneous rocks, rich in magnesium and sulfur, poor in oxidised iron and titanium, and containing volatile elements in unexpectedly high concentrations (McCoy & Nittler, 2014).

Physical Models for Metal Enrichment in Mercury

To account for the high metal/silicate ratio on Mercury that results in a relatively high density, some scientists used physical mechanisms of metal enrichment. Weidenschilling (1976) theorised about aerodynamic fractionation separating metal and silicate while Mercury's accretion was taking place. Another model appeals to a giant impact that took place after Mercury had differentiated that caused a major stripping of the silicate mantle off the planet (Benz et al., 1988; Cameron et al., 1988; Wetherill, 1988). Unfortunately, neither model can explain Mercury's FeO limited surface composition, compared to other terrestrial planets, such as Earth and Mars that exhibit higher FeO surface contents.

High-Temperature Evaporation and Condensation Models for Mercury

The second class comprises models for which the low distance of Mercury from the Sun is particularly important. Lewis (1972, 1974) elaborated an outdated scenario in which Mercury assembled in the closest and thus hottest region of the Solar nebula, to account for the low FeO content on Mercury's surface. If Mercury had formed in that region of the Solar nebula, its composition could be affected by high temperatures. First of all, most of the iron would be in its metallic state rather than in its oxidized state. Secondarily, much of the silicate content would be lost due to vaporization to increase the metal/silicate ratio. Eventually, this model predicts that Mercury should have high concentrations of refractory elements, among which there are calcium, aluminum and thorium, and low content of volatile elements, such as sodium and potassium, if compared to other terrestrial planets.

Refractory-Volatile Mixtures

The presence of FeO on Mercury and the idea that planetary accretion involved mixing throughout the inner Solar System motivated models involving mixing of refractory and volatile materials, with relative proportions affecting the planet composition (Goettele 1988; Morgan & Anders 1980).

Formation of Mercury from Known Chondritic Meteorites

Chondrites were long considered as the building blocks of the planets, but recently enthusiasm for this notion has waned, also considering that no match has been found between any known chondrite group and the bulk Earth. Nonetheless, several authors have studied the origin of Mercury in light of a clan of meteorites rich in metal and poor in FeO. This clan comprises CR chondrites (Renazzo-like chondrites), CH chondrites (highly rich in metal) and CB chondrites (Bencubbin-like chondrites), recognized among Antarctic meteorites (Grossman et al., 1988; Krot et al., 2001; Scott, 1988; Weisberg et al., 1993, 1995). These types of chondrites are richer in metallic iron and poorer in volatile elements like sodium, potassium and sulfur than other chondrites, while maintaining similar contents of refractory elements and FeO. Enstatite chondrites have also been accounted as potential building blocks for Mercury. Wasson (1988) suggested this match because of Mercury's location close to the Sun, where enstatite chondrites were formed.

1.1 MESSENGER mission

Important insights into the geochemistry of Mercury were provided by NASA's MESSENGER mission (MErcury Surface, Space ENvironment, GEochemistry and Ranging), which entered orbit around the planet in 2011. MESSENGER was the second mission to reach Mercury, after MARINER 10, in 1974 and 1975, which was able to do three flybies around the planet, thanks to the calculation of prof. Giuseppe Colombo from the University of Padua. Mariner 10 gives the first information about part of the Hermean surface and the environment, suggesting some similitude and several differences with the Moon (Strom & Sprague, 2003).
In particular, MESSENGER was equipped with a set of spectrometers and imaging systems that led scientists to provide the first global datasets of surface elemental abundances, mineralogy and geological context (Solomon et al., 2001). One of its most groundbreaking findings was the detection of unexpectedly high contents of some volatile elements. Sulfur concentrations on the surface measured by X-ray spectrometry ranged from 1 to 4% (Nittler et al, 2011; Weider et al., 2016). Observations of K/Th and Cl/K ratios on Mercury suggest that Mercury retained a significant amount of its original volatile repertoire (e.g. Peplowski et al., 2011). These results clearly oppose Mercury's high-temperature formation and start a fundamental new evaluation of Mercury's origin and thermal evolution.

Mercury's high-resolution imaging revealed further surprises. Extensive smooth plains were identified, which now appear to be largely of volcanic origin, as well as pyroclastic deposits that imply explosive volcanic activity, probably driven by volatile-rich magmas (Blewett et al., 2011). Rimless, shallow depressions associated with bright, spectrally distinct materials, called hollow formations are believed to develop through the loss of surface-bound volatiles, likely via sublimation or outgassing (Blewett et al., 2018). Mercury's features denote a dynamic geologic past, in which endogenous processes, including effusive and explosive volcanism, modified the surface well into the planet's middle to late geologic history.

Geological mapping of different quadrangles, such as the Kuiper region (H06) (Giacomini et al., 2022), provided stratigraphic and morphotectonic information for interpreting Mercury's surface evolution. These maps uncover a complex interplay between ancient, cratered terrains and younger volcanic plains, as well as tectonic landforms such as lobate scarps and wrinkle ridges (Watters et al., 2009), thus revealing that a global contraction took place, that could have been originated by many phenomena among which a core cooling (Byrne et al., 2014). Crater retention ages indicate the existence of resurfacing events dating from ~3.9 to 3.6 billion years ago, supporting the idea that volcanic activity persisted beyond the Late Heavy Bombardment (Marchi et al., 2013).

With its gravity and libration data, MESSENGER mission has also confirmed the presence of a large, partially molten metallic core and a solid silicate mantle-shell of ~410 km thickness (Margot et al., 2007; Smith et al., 2012). Some models also suggest that the core-mantle boundary presents a stratified FeS layer, consistent with Mercury's formation under highly reducing conditions. This idea supports an iron-rich and oxidatively reduced planet that still retained a complex array of volatile elements in both its interior and its surface layers (Smith et al., 2012).

MESSENGER cumulative data began to shift the paradigm under which volatile depletion is inevitable with the proximity to the Sun. Indeed, Mercury results as a planet that either formed from volatile-bearing materials despite the proximity to the Sun or acquired and preserved volatiles through processes still little investigated (Blewett et al., 2011, 2013; Helbert et al., 2013). These results have impactful implications for models of planetary formation throughout the Solar System and in extrasolar environments, and not only for Mercury. It hints that highly reducing conditions, rather than high temperatures alone, may play a critical role in defining a planet's volatile repertoire. Furthermore, differentiation paths among terrestrial planets are challenged by the lack of anorthositic crust, the abundance of magnesium-rich silicates and the deduced composition of Mercury's mantle (Stockstill-Cahill et al., 2012).

1.2 Hollows on Mercury

The discovery of hollows on Mercury represents one of the most important findings from NASA's MESSENGER mission. Hollows are landforms that were never observed before on other planetary surfaces, which seriously challenged well established assumptions about Mercury's geological quiescence and volatile-depleted nature. Hollows are morphologically distinct depressions: shallow, with irregular shapes, rimless and often flat-floored, with unusually bright interiors and halos contrasting with the surrounding terrain (Blewett et al., 2011, 2013; Thomas et al., 2014). Hollows are also characterised by a recent appearance and the lack of superposed craters that suggest that they are among the youngest features on Mercury (Blewett et al., 2018).

Hollows are typically located on craters central peaks, walls, floors and rims and are often associated with regions of Low Reflectance Material (LRM) (Blewett et al., 2011, 2013; Thomas et al, 2014), spectral units that exhibit an albedo even lower than that of the average crust of Mercury and whose origin is hypothesized to be the carbon-rich endogenic sources of magma ocean flotation (Klima et al., 2018; Vander Kaaden & McCubbin, 2015; and reference therein). Their well defined distribution and spatial clustering suggest a compositional control on their formation (Villas et al., 2016). The leading interpretation about hollows states that they are the result of a devolatilization process in which subsurface volatile-rich materials sublimate or chemically dissociate under Mercury's extremely high diurnal temperatures and powerful Solar radiation, thus leaving behind collapsed structures and bright residues (Blewett et al., 2018; Lucchetti et al., 2018).

Despite being limited by the resolution of remote sensing instruments, spectral analyses of Mercury's hollows have revealed diagnostic absorption bands between 559-828 nm and at ~629 nm, which have been experimentally attributed to magnesium and calcium sulfides (MgS, CaS) and graphite (e.g. Vilas et al., 2016; Wang et al., 2020). These compounds are volatile under Mercury's surface temperatures and may have been concentrated through magmatic, impact-related or depositional processes in the crust (Asphaug & Reufer, 2014; Kerber et al., 2009, 2011). However, spectral features alone are still not sufficient for a conclusive identification of materials, due to several reasons, such as mixing with devolatilized substrate and regolith, surface weathering and the sub-kilometric scale of most hollows (Wang et al., 2020).

From a geological approach, hollows represent a unique surface expression of volatile loss processes. Unlike pyroclastic deposits and volcanic vents, hollows lack evidence of explosive eruption, thus suggesting a different degassing mechanism, probably a combination of sublimation, thermal deposition, micrometeoroid impact vaporization and chemical sputtering (Blewett et al., 2011). Hollows association with tectonic and impact-related features suggests that structural weaknesses may act as channels for volatile migration or as loci for mechanical breakdown of unstable mineral phases (Blewett et al., 2013).

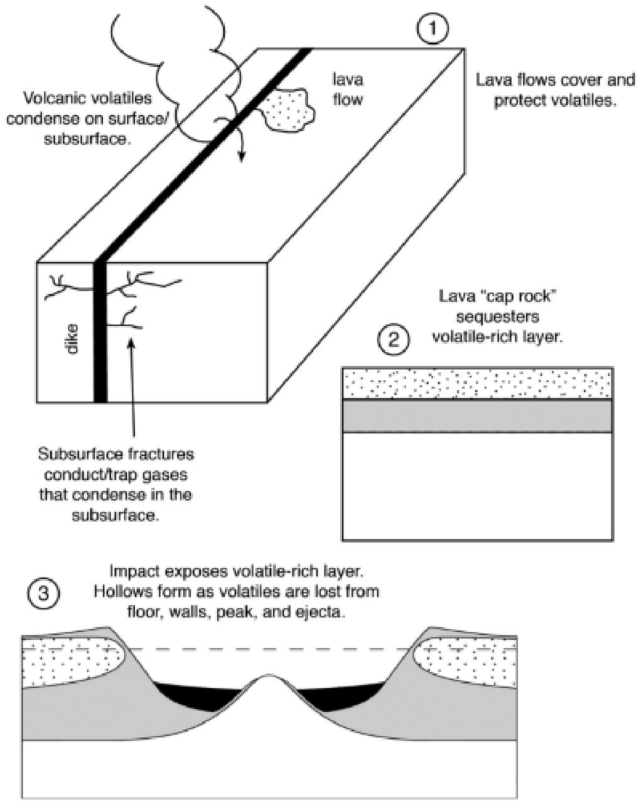

Fig. 3: Modified by Blewett et al (2013). Schematic illustration of hollow formation by sequestration, impact exposure, and loss of magmatic volatiles.

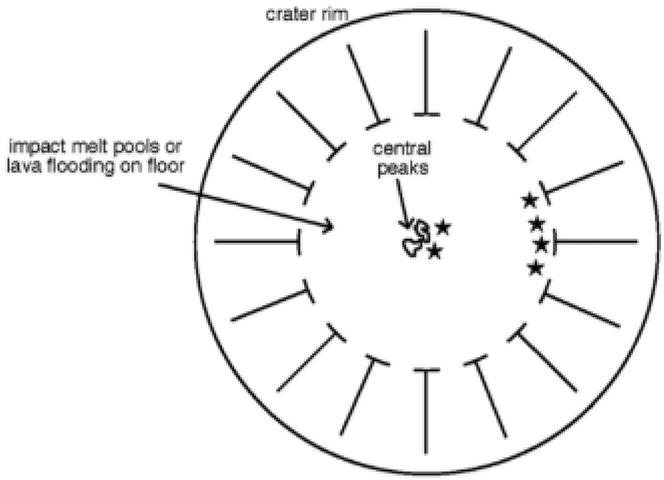

Fig. 4: Modified by Blewett et al (2013). Schematic illustration of hollow formation by contact metamorphism. Heating of wall and peak material by shock, impact melt, volcanic flows, or intrusions could decompose volatile-bearing minerals, leading to the formation of hollows by mechanical failure of the remaining matrix. Hollows (stars) are initiated around topographic highs (walls and central peaks).

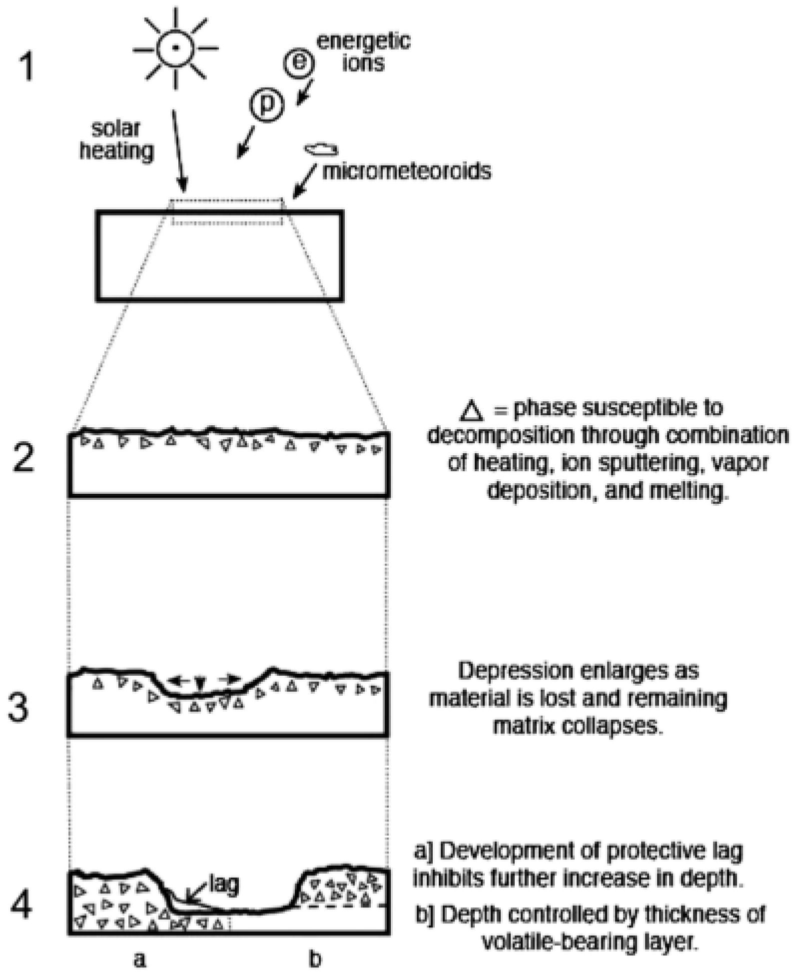

Fig. 5: Modified by Blewett et al (2013). Schematic illustration of hollow formation by solar heating or space weathering. Some combination of high temperatures, ion sputtering, and

micrometeoroid melting and vaporization decomposes volatile-bearing minerals, leading to formation of hollows by failure of the remaining matrix (sequence from 1 to 3). The depression stops increasing in depth when (4a) a protective armour of remnant material builds up, or (4b) the volatile-bearing layer has been consumed.

Through high-resolution imaging and spectral clustering analyses it was possible to observe that hollows across various craters share consistent spectral behaviours and geological settings, denoting a shared formation mechanism. Lucchetti et al. (2018) suggested that hollows absorption features could also be affected by the bedrock itself, especially by pyroxenes containing transition metals, where Fe is very low, such as Cr, Ti and Ni, asserting for a hybrid origin involving both residual degassed materials and original crustal components (Lucchetti et al., 2018).

From the temporal perspective, hollows are even more complex than what discussed up to here. Based on crater counting and degradation state analyses methods (introduced by Arvidson et al., 1979; Neukum et al., 2001; Le Freuve & Wieczorek, 2011), most Mercury's hollows appear to be less than 100000 years old, with some of them possibly still active. Estimates of the total volume of volatiles lost through hollows formation exceed 1200 km^3 (Wang et al., 2020), inferring a remarkable inventory of volatile-rich materials in Mercury's shallow crust and an occurring or recent internal redistribution of volatiles. Such active or recently active processes share awareness about Mercury as a dynamic planet, long thought to be geologically inert.

Implications of these features extend beyond Mercury because hollows represent an unprecedented surface process driven by volatile loss in the absence of an atmosphere. Studying hollows could provide a deeper comprehension about volatile retention, loss mechanisms and space weathering on airless planetary bodies. It could also lead to interpretations of similar features observed on the Moon or asteroids. In addition, the investigation of the mineralogical and structural factors affecting hollows formation could contribute to acquiring a better understanding of planetary differentiation and crustal evolution in the early Solar System.

1.3 Aim

This thesis aims to extensively investigate the nature of Mercury's hollows by integrating geomorphological mapping and spectral data analysis. The work seeks to better understand hollows origin and their importance in the context of Mercury's geological evolution. Indeed, hollows offer a unique opportunity to explore the dynamic interaction between volatiles, planetary crust and surface processes under extreme environmental conditions. To do this we chose four different craters hosting a wide distribution of hollows on the crater floor: the Warhol crater (353° N, 2° O, Kuiper quadrangle H-06, 91 km diameter), the Hopper crater (304° N, 12° W, Kuiper quadrangle H-06, 36 km diameter), the Eminescu crater (114° N, 10° E, Eminescu quadrangle H-09, 129 km diameter), the Sander crater (154° N, 42° E, Raditladi quadrangle H-04, 47 km diameter). All these craters have been mapped from a morphostratigraphic point of view (chapter 3.1) at the best scale possible. Then we investigate the spectral variability (chapter 3.2) of the hollows for each site, as well as, the surrounding terrains, to highlight the mineralogical variability and the potential influence of the material from the surrounding terrains where hollows are imposed. We discussed (chapter 4) the results comparing the different investigated cases with respect to the literature.

2. Data and Methods

2.1 Base Maps, images and derived products

When MESSENGER went into orbit around Mercury in 2011, the MDIS (Mercury Dual Imaging System, Hawkins et al., 2007) instrument collected images with much higher resolution than those acquired during flybys, providing high-resolution targeted observations. Those data can be combined to lower resolution images providing global monochrome and multispectral base maps. The MDIS instrument consists of the narrow angle camera (NAC), with a 1.5° field of view and of the wide-angle camera (WAC), with a 10.5° field of view (Hawkins et al., 2007). We use both NAC and WAC monochrome images and WAC multispectral images to provide detailed geomorphological map of craters hosting hollows and to characterize the spectral behaviour of these features (similar to what done e.g. in Lucchetti et al., 2018).
The MDIS NAC provided high-resolution images for the study of the detailed morphology of hollows, and different morphological facies are classified. Eight-band MDIS Wide Angle Camera (WAC) images were used to analyse the reflectance spectra in the wavelengths of ~430–1,000 nm. (Denevi et al., 2018).

The first step for mapping the selected Mercury's craters was to download the MDIS-NAC (Narrow-Angle Camera) images for a much higher resolution, and, where the images were not accessible, the MDIS-WAC (Wide-Angle Camera) with a lower resolution, were a valuable option. In addition to these data, the BDR (Basemap reduced Data Records)[resolution of 256 pixels per degree (~166 m/p)], Enhanced Colour Global Mosaic (resolution of 665 m/pixel) and LOI (LOw Incident)[resolution of 256 pixels per degree (~166 m/p)] basemaps, that are mosaics of both WAC and NAC were used as a background where there is no cover of the NAC selected. These basemaps were used for all the sites of study and the NAC used were specifically 3 for Warhol crater, 4 for Hopper crater, 4 for Eminescu crater and 4 for Sander crater as well. They permit to have a context on which to superpose the high resolution images as well as the 8 colour mosaics.

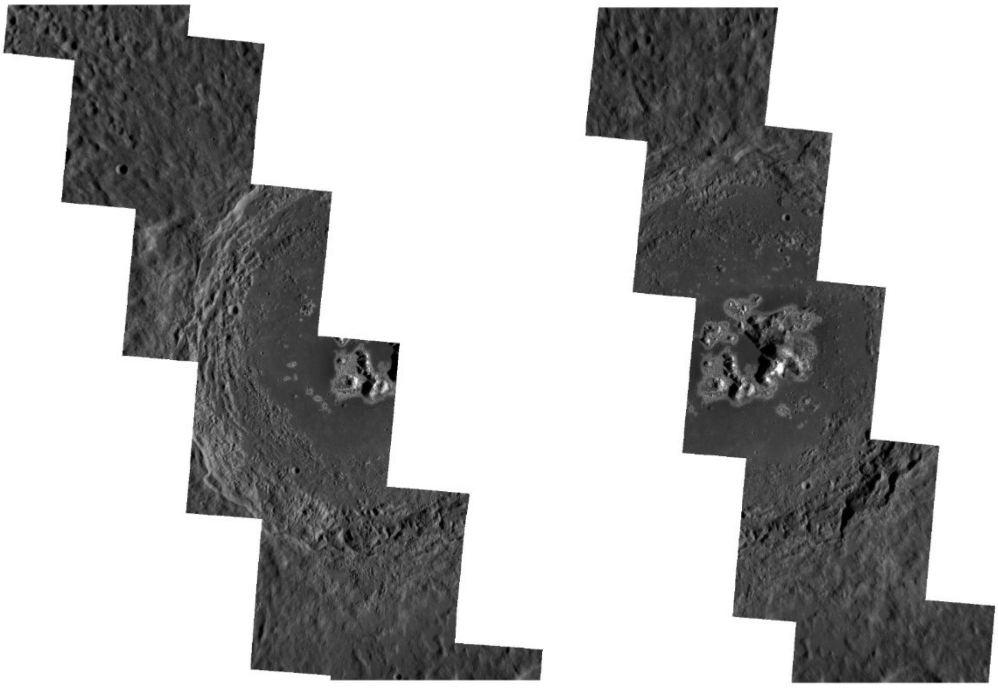

Fig. 6: Examples of NACs mosaics released by MESSENGER team of two portions of Eminescu crater at resolution of 130 m/pixel.

These data can be downloaded from different platform, here we used the PDS, NASA node call “Mercury ODE” (Orbital Data Explorer) (Fig. 7) where it is possible to search considering the specific instrument, data level and geography regions the existing images.

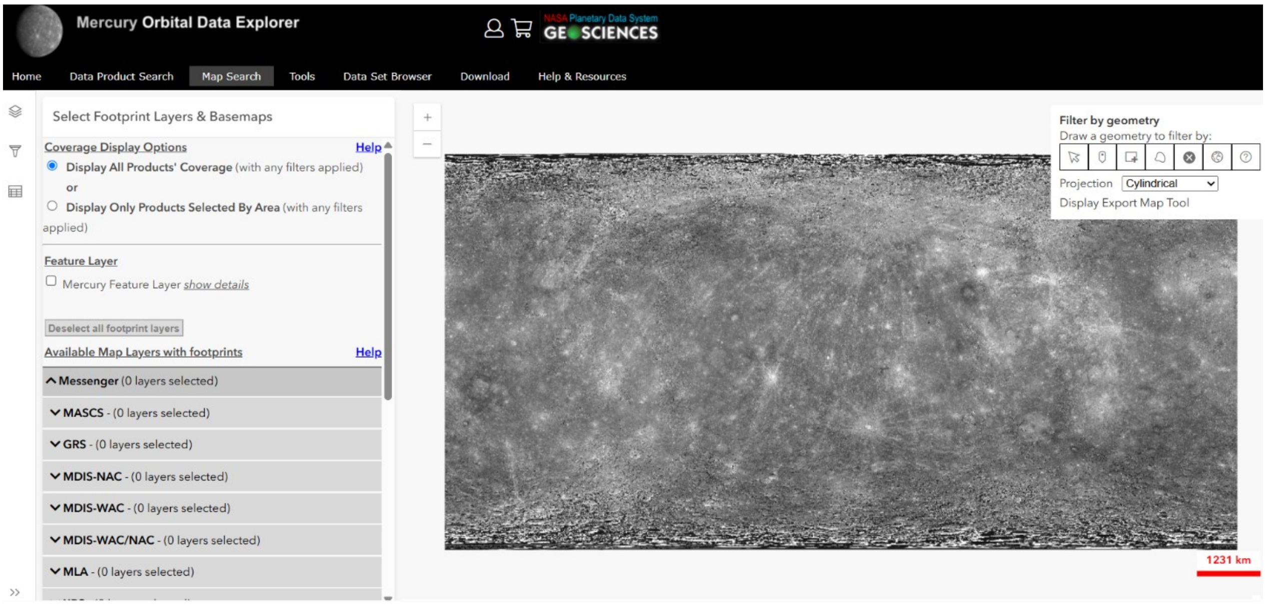

Fig. 7: ODE layout for downloading Mercury’s data, among which NAC and WAC-MDIS images

Once we selected the area of interest (Fig. 8), and the specific required data set, it's possible to send the request for downloading the desired products of the selected areas.

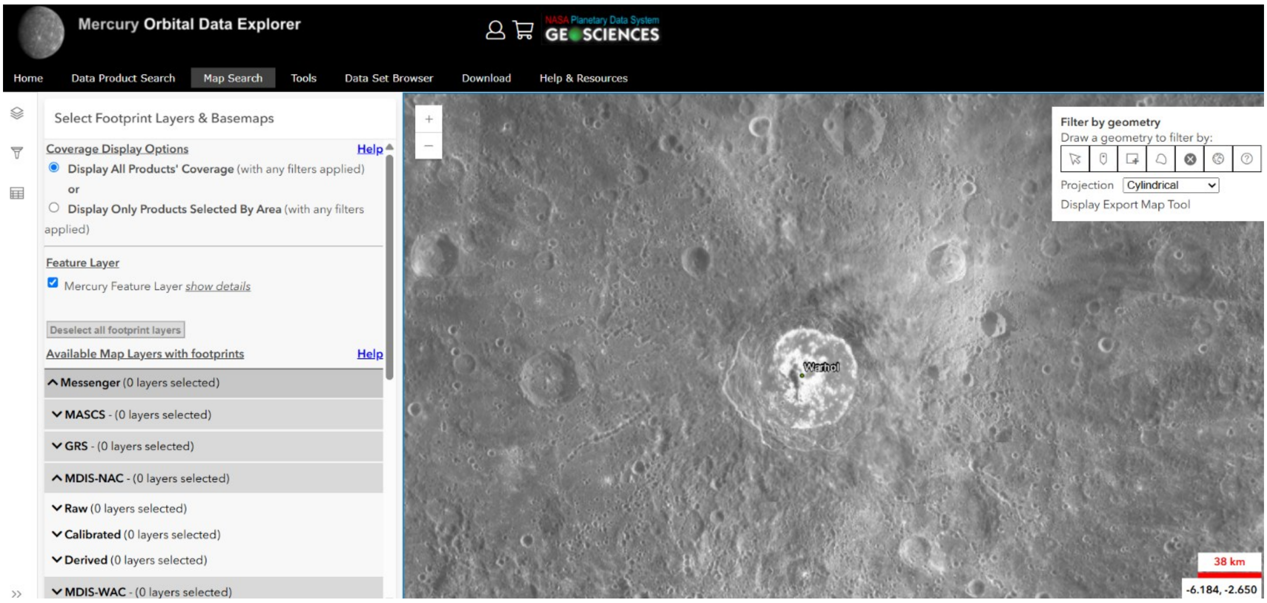

Fig. 8: Warhol crater in ODE's map search tool

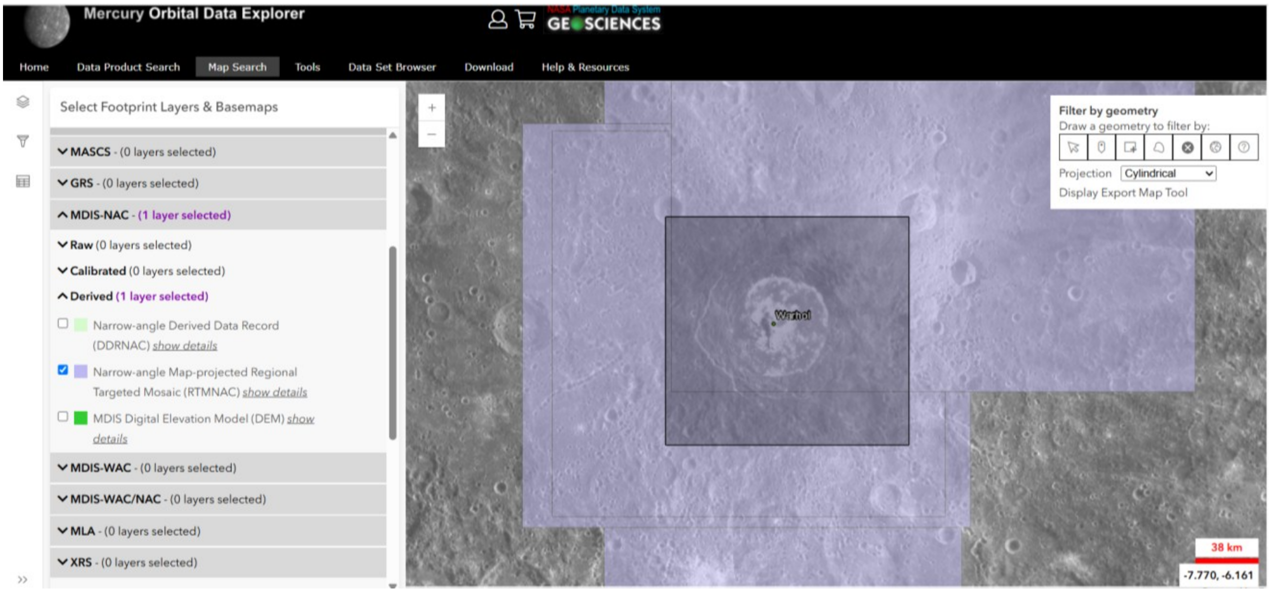

Fig. 9: Warhol crater in ODE's map search tool with the available products for the selected area.

2.2 Geomorphological mapping

For this study the software used were QGIS (QGIS Development Team (YEAR). QGIS Geographic Information System. Open-Source Geospatial Foundation Project. http://qgis.osgeo.org) and ENVI (ENVI® is a registered trademark of NV5 Global, Inc. https://www.nv5geospatialsoftware.com), respectively for the geological mapping and for the spectral analysis of four craters on the surface of Mercury: Warhol, Hopper, Eminescu and Sander.
After downloading the data, they can be opened in QGIS (Fig. 10) where the mapping work can be done. The first step was to find an appropriate georeferencing system that can assign real-world coordinates to a raster dataset, such as a scanned map or aerial photograph, so it can be displayed and analysed alongside others geographic data. For this work, the one used is "Mercury (2015) ESRI: 104974" as a coordinates system. All the NAC images and the mosaics were manually translated to the same coordinates system to grant an overlay between all the images obtained from different sources. When all the dataset was set, the mapping of the craters was done with a tool of QGIS called Mappy (This plugin simplifies the generation of polygonal geological maps from lines (contacts) and points (identifying the units). This plugin was developed as the result of the PLANMAP project (N 776276) and is now maintained thanks to the EUROPLANET-GMAP infrastructure (N 871149) and supported by the JANUS camera team of the JUICE mission (ASI-INAF 2018-25-HH.0). https://plugins.qgis.org/plugins/mappy/) (Fig. 11), with which was possible to create polygons of the desired features recognized and then to create a categorized map on the images with a legend of the features.

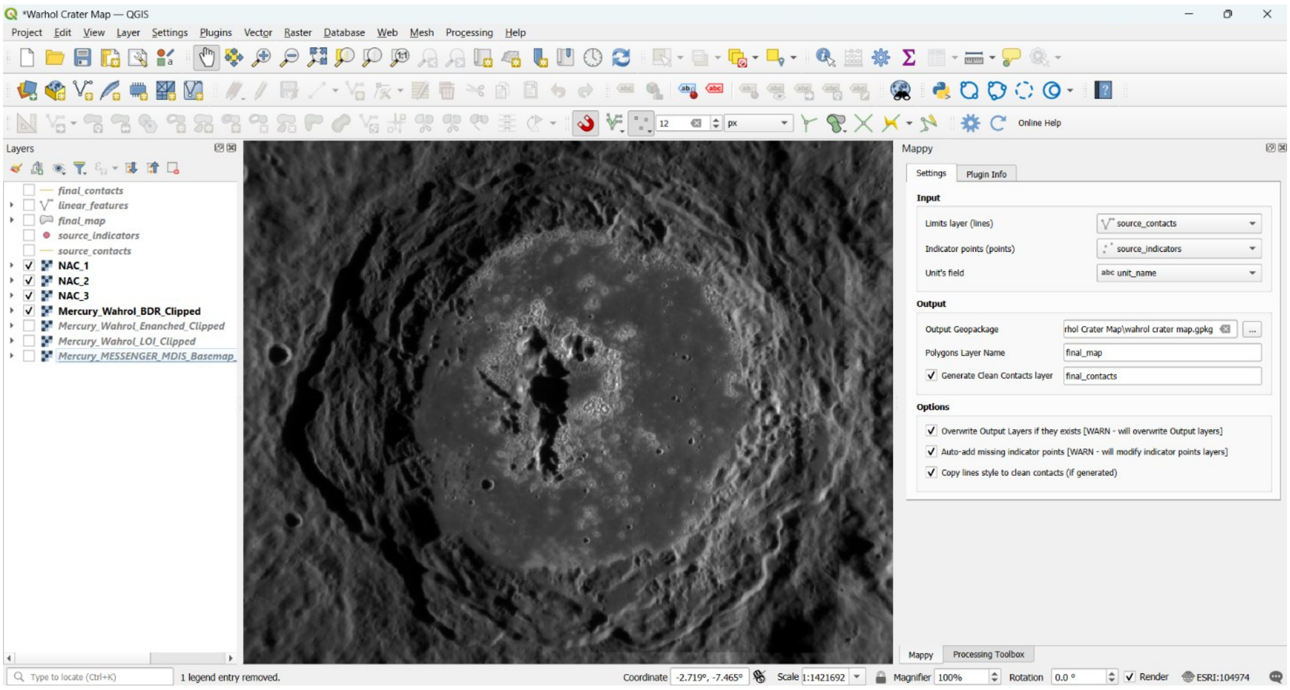

Fig. 10: The visualization of a NAC in QGIS

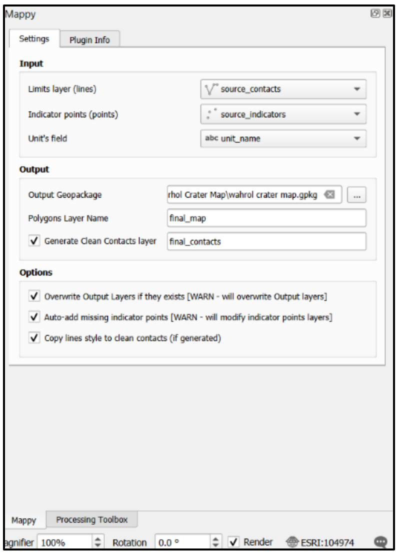

Fig. 11: Mappy tool parameters

Moreover, with it was possible to point out some linear features such as “crater rim”, “terrace”, “peak crest”, “small secondary crater rim” to make a more detailed map of the craters.
For the hollow’s identification, the Enhanced map was used to see where the cyan/blue portions of the crater were, with a greater resolution compared to the previous work of literature, except for Hopper.
To better identify the hollows, they were divided in “isolated hollows” where the feature was clearly visible and isolated from the others, “cluster hollows” where a number of hollows was near each other in a well-defined group, “hollow field” when the analysis with the enhanced map pointed out the same or similar spectral firm without having geomorphological evidence on the surface.
This led to the creation of a map with the desired features (Fig. 12) for all the four craters.

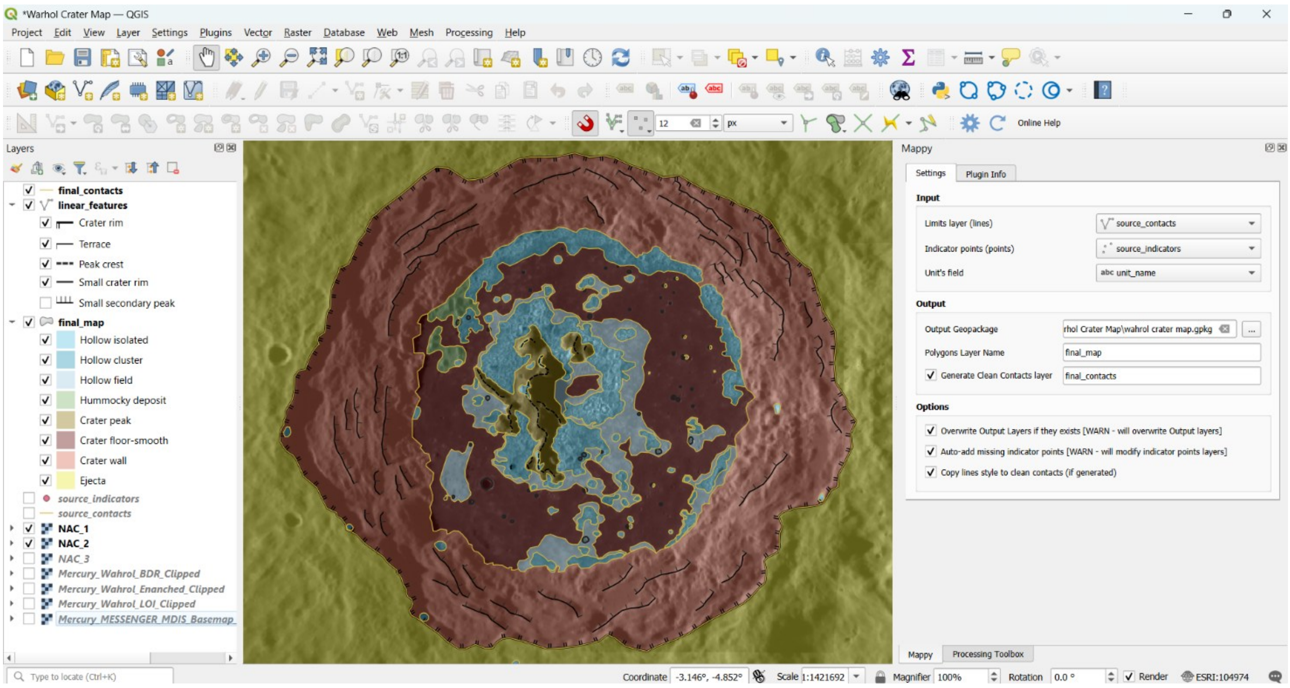

Fig. 12: Warhol crater map and legend with the tool mappy.

After this work was done, it was easier to better understand the hollows distributions in the studied craters, to make a more precise spectral analysis thanks to the high-resolution product made.

2.3 Spectral analysis

Regarding the spectral analysis, the aim of this investigation was to enlighten the different spectra of hollows, crater floor, and regions outer the floor of the crater (e.g. wall, proximal ejecta) and some segments with characteristic features in it, between each crater.
To do this we considered the Enhanced color global mosaic, a RGB with PC2 (principal component 2), PC1 and 430/1000 reflectance ratio in the three channels, for a “regional” framework. Then we downloaded the best spatial resolution 8 color images covering each selected crater and an 8 color mosaic for each of them has been produced by IAPS-INAF researcher F.Zambon using ISIS (Integrated Software for Imagers and Spectrometers) tool following the process done by Zambon et al. (2022).
This 8 color mosaic is characterized by filters at a resolution of 460 nm/px for Eminescu and 133 m/px for Sander.
After opening the images (example in Fig. 13), the first step involved the enhancement and the stretching of the RGB images produced considering the PC2, PC1 and 430/1000 parameters, where the stretching was measurable by the variation in the histograms (Fig. 14).

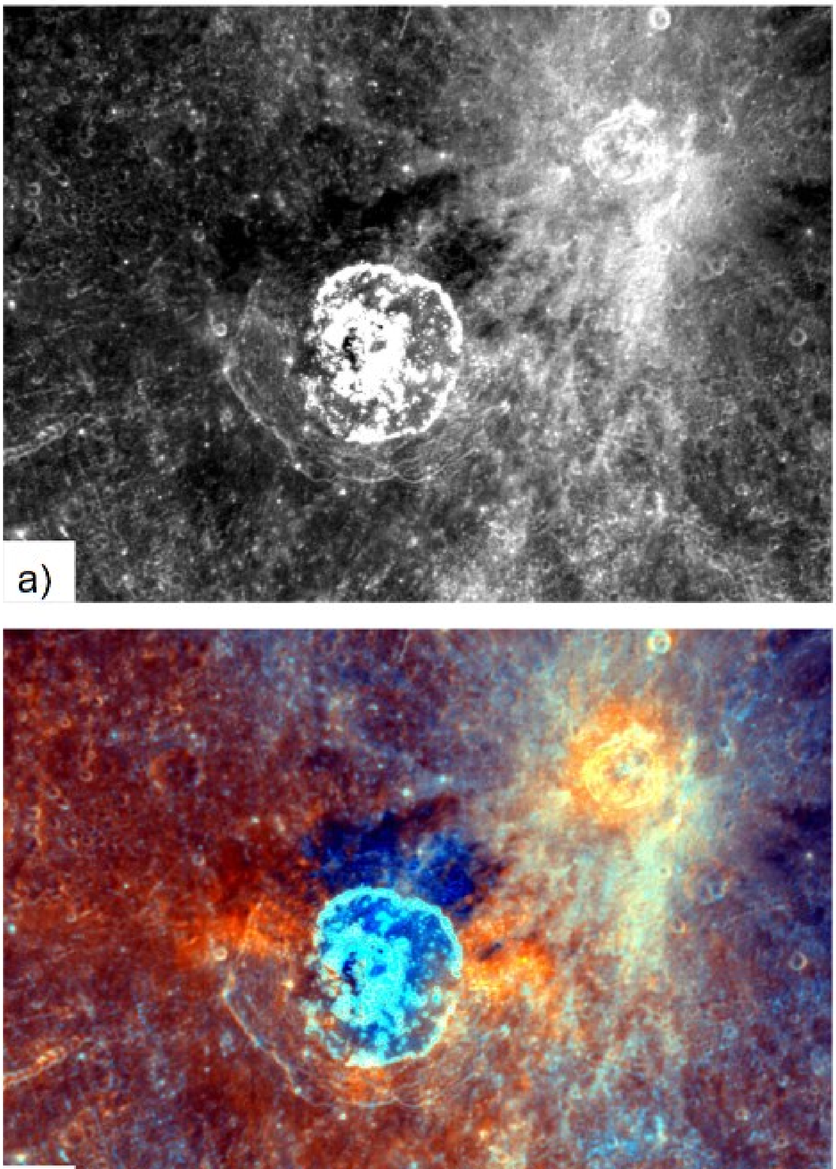
a)
b)
c)

Fig. 13: Respectively, a) images in grey scale of the band 4 at 630 nm, b) enhanced color based on PC2, PC1, 430/1000 RGB and c) the same RGB within a zoom on the Hollows dominated region on Warhol crater.

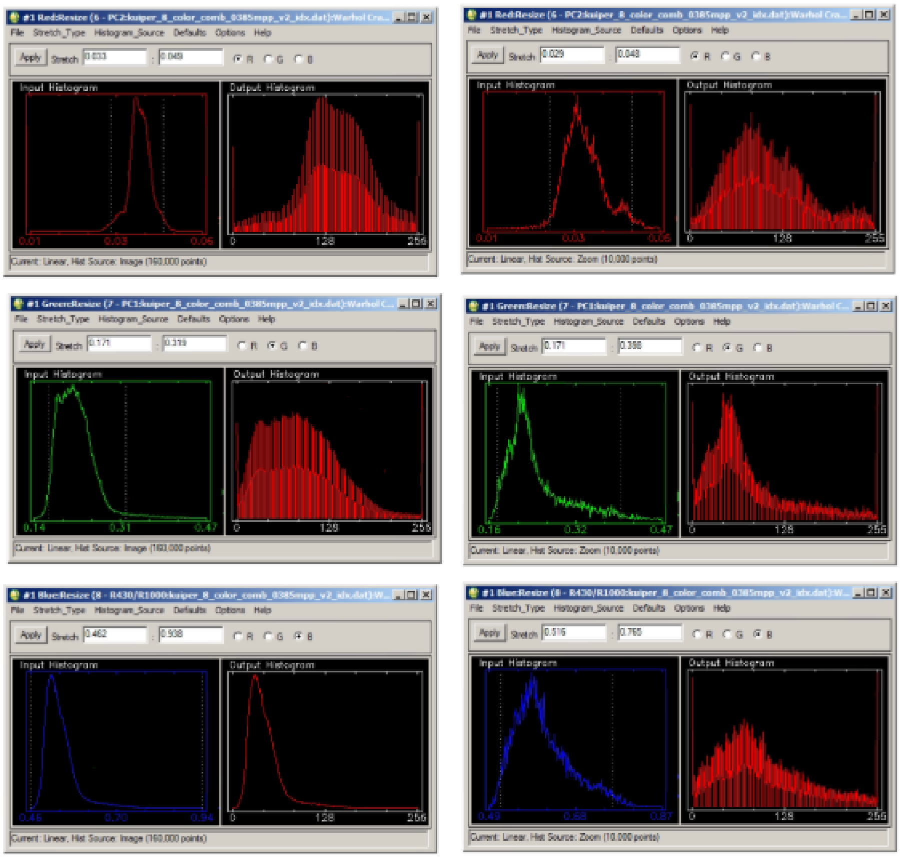

Fig. 14: Examples of Histograms of the RGB enhanced at 8 color mosaic image level (left) and then stretched (right) on Hollows field region of the Warhol crater.

Linking the grey-scale display where the multispectral dataset was present to the enhanced RGB was possible to analyse the spectra of all the craters in which, by the function "collect spectra", the desired pixels can be collected specifically for the type of study needed. After the first outcome that shows the different spectra (Fig. 15), by the function "continuum removed", the spectra were plotted to maximize the potential differences in the main spectral features looking at the trend of the hollows (Fig. 16) and comparing them with the material characterizing the rest of the craters.

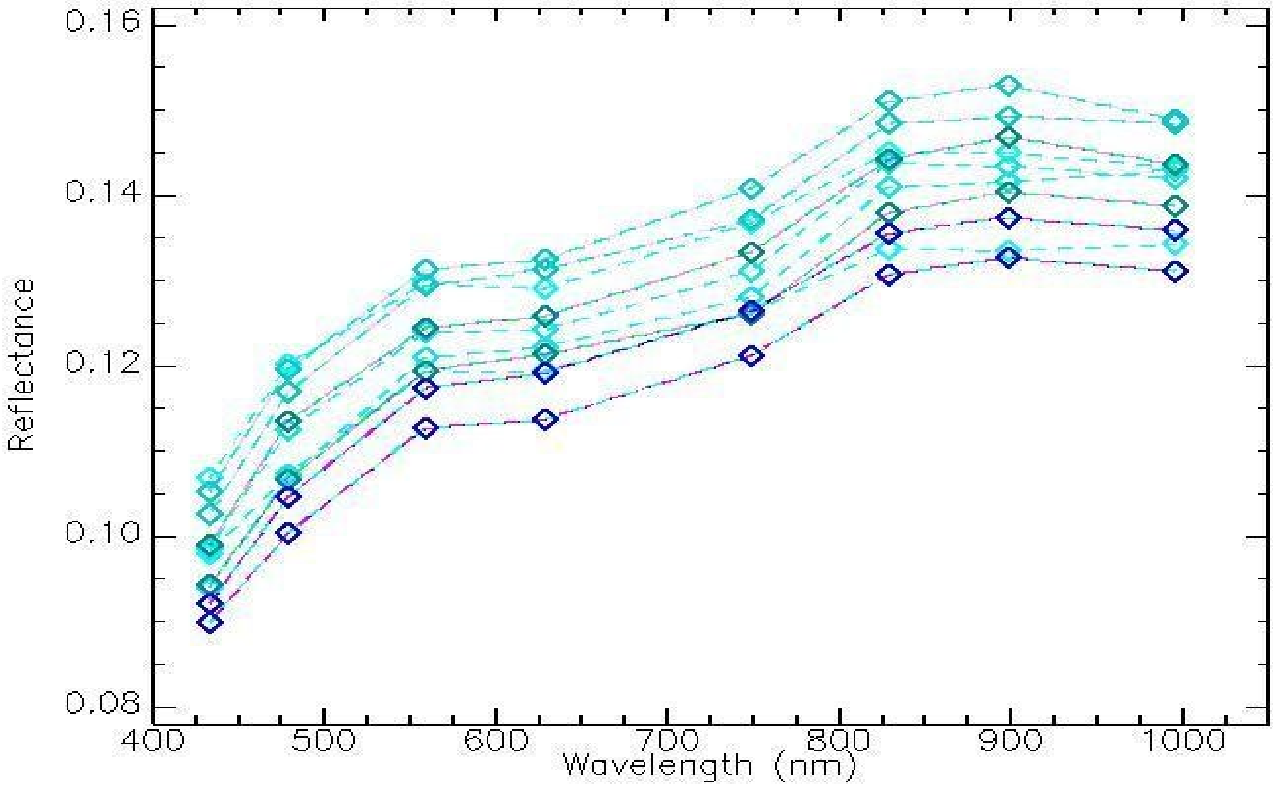

Fig. 15: Example of spectra collection for a hollow cluster in Warhol crater

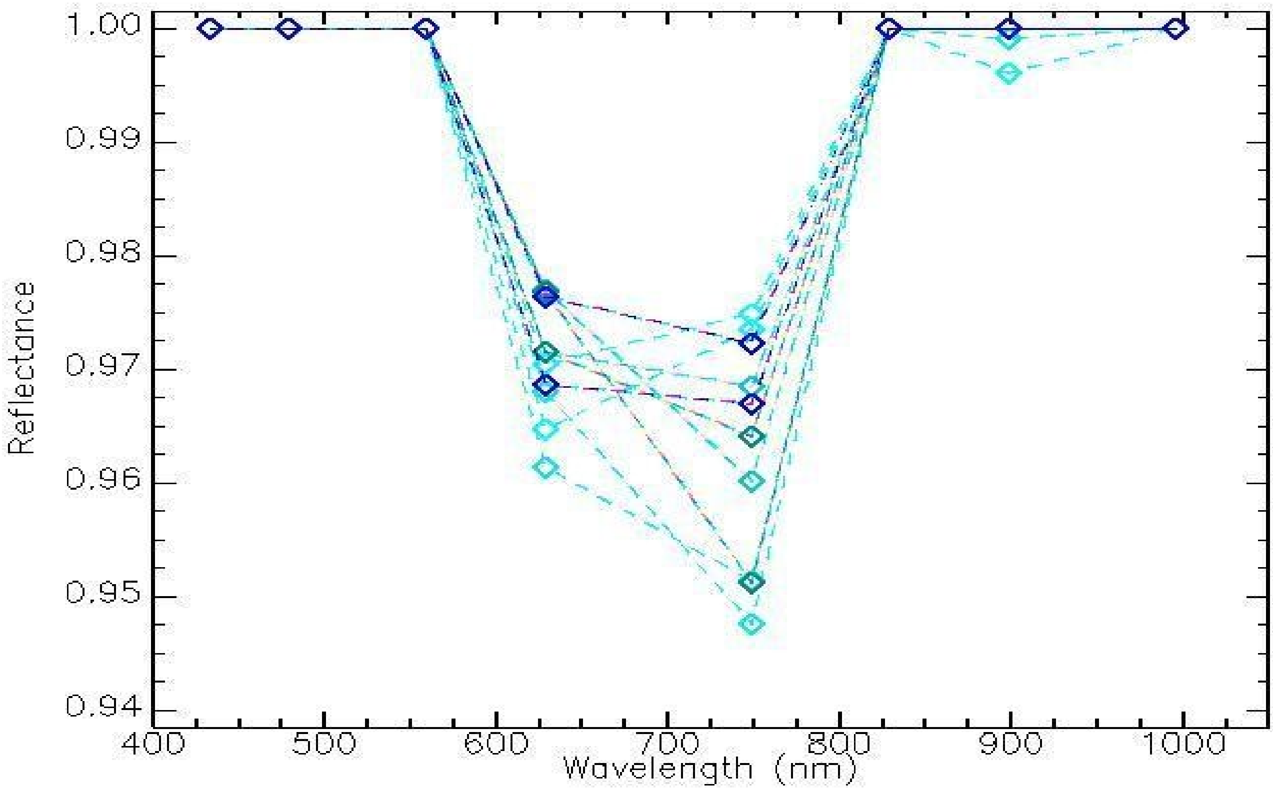

Fig. 16: Example of automatic continuum removed spectra of the hollow cluster in Warhol, from the same spectra in figure 9.

The second step was to identify some ROIs (Region Of Interest) (Fig. 17) of homogeneous spectra in a specific color unit, suitable for the spectral comparison, thanks to which a statistic study can be computed by the software and return the spectral average with the maximum and minimum as well as standard deviation for every collected ROI (Fig. 18).

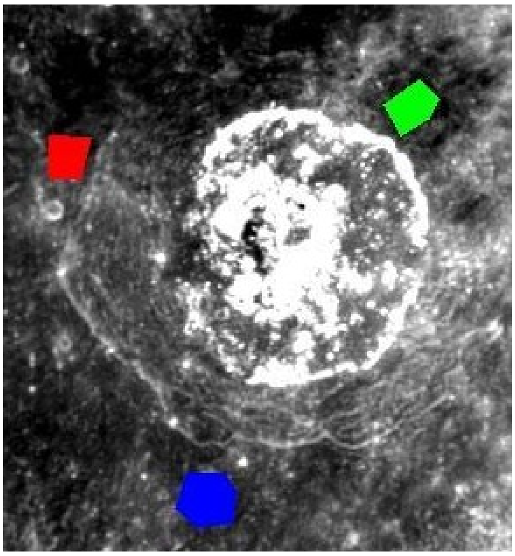

Fig. 17: Examples of ROI of 3 polygons collected on the proximal ejecta of Warhol crater

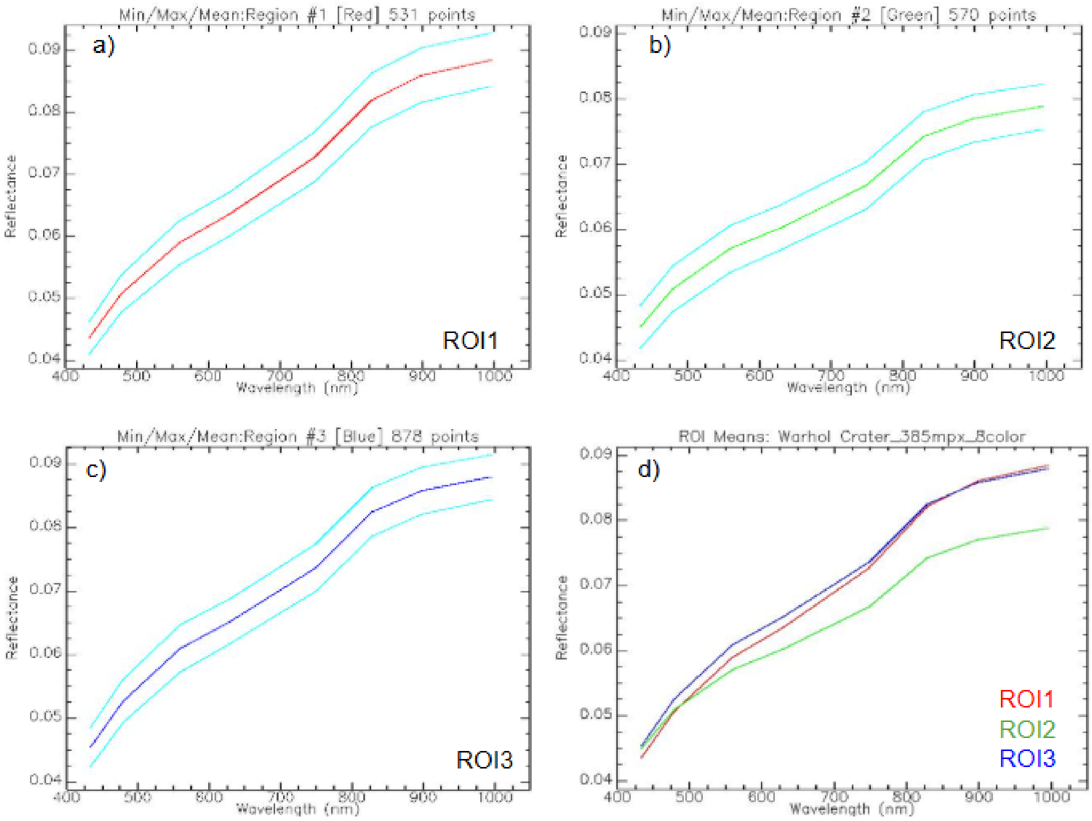

Fig. 18: Example of ROI's statistics of the (a) red, (b) green, (c) blue polygons and (d) the outcome with all 3 average cases compared. In a), b) and c) the average spectrum is plotted together with the specific standard deviation.

3. Results

3.1 Geomorphological maps of craters

The work with QGIS led to the results of a high resolution well-defined map that allowed to identify, for all the craters under consideration, the main morpho stratigraphic units which help to locate the hollows, distinguish hollow clusters from hollow field, and on the other hand, permit to compare the different cases with each other. Following we report the results of all the four investigated craters:

3.1.1 Warhol crater

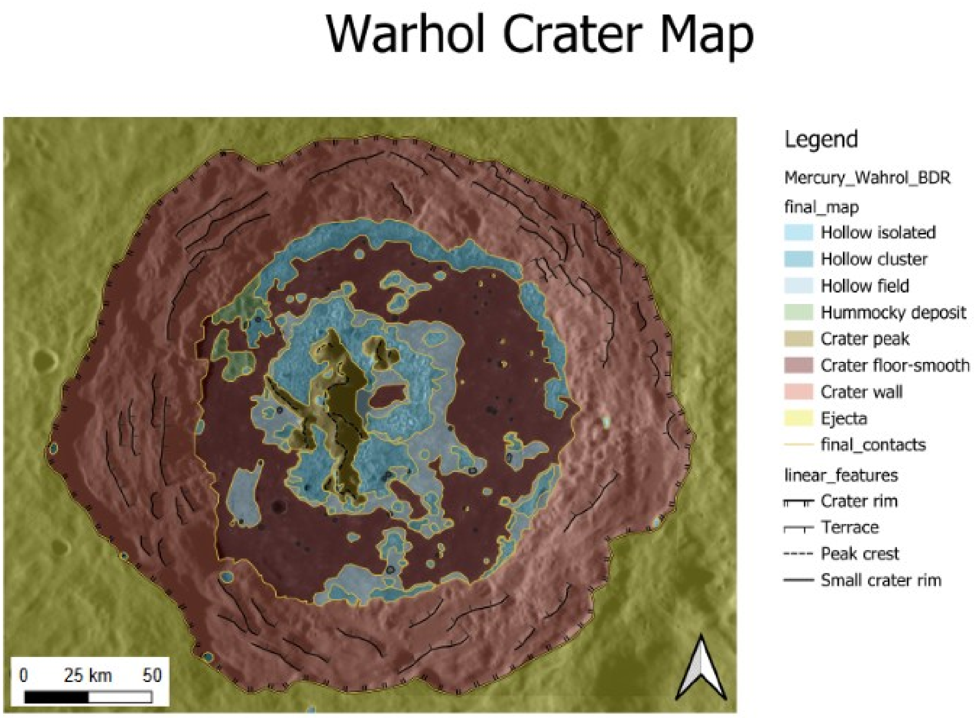

Fig. 19: High-resolution geological map of the Warhol crater (353° N, 2° O, Kuiper quadrangle H-06, 91 km diameter) created with the tool mappy in QGIS using a monochrome BDR base map (256 pixels per degree, ~166 m/p) and NACs (230 m/px) as a background.

Warhol crater map (Fig. 19) shows a well defined rim and wall, permitting to consider this crater as a relative fresh one in accordance with the previous identification a C3, indicative for craters with sharp, intact rims and well-preserved central peaks (Giacomini et al., 2022). This was identified using the yellow colour for the proximal ejecta that was mapped here. The ejecta shows themself rayed and bright and can extend for over 1 diameter from the crater rim.

The wall is characterized by a large number of terraces distributed all along the crater wall, mainly localized in the north and south portion. The wall hosts few isolated hollows with the diameters that vary from 2.88 km to 4.56 km.
The crater shows the central peak which is characterized by a predominant central crest in the middle of the crater with a North-South alignment, and smaller outcrops coming on the North-East side.
The floor shows a rough surface, moderately affected by secondary craters or it is covered by smooth deposits and is characterized by a large infilling of a very smooth unit which can be attributed to upwelling of effusive volcanic material immediately following the impact that formed the crater, although, a second hypothesis of formation due to a secondary impact origin cannot be completely excluded (Denevi et al., 2013; Whitten et al., 2014). Moreover, in the North-West section it can be noted that there are more roughly/irregular terrains which can be indicated as hummocky deposits similar to the case of Dominici crater reported by Lucchetti et al. (2018) (Fig. 20).
The crater floor also shows a small distribution of narrow craters ranging from 5.56 km to 1.41 km of diameter, probably secondary.

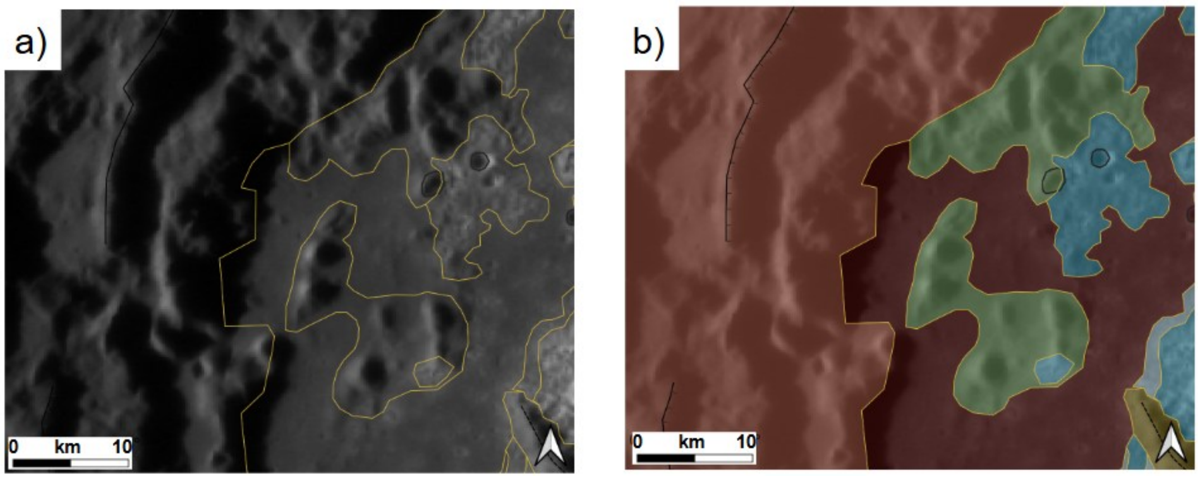

Fig. 20: Focus of the Warhol crater map for a comparison between a NAC image and the created map to see the contact (a) among geomorphological units. In the right (b) image an inset of the final map permit to highlight the units like crater wall (bright brown), crater floor-smooth (dark brown), hummocky deposit (green) and hollow cluster (cyan).

The hollows here are present wider in the floor, superimposed to the smooth infilling, near the central peak but even around the contact from the floor and the wall and partially on other points of the floor. We defined two main different portions among the, in general, hollow field with a different relative density. The hollow field here is indicated as a contour of the denser hollow cluster (see Fig. 21); where the enhanced mosaic map identifies the same or similar spectral feature, but it’s not visible on the NAC’s crater floor, whereas we identify the portion with a higher density of hollows, which are identified with rougher surface, as hollow cluster. The same approach was used by Lucchetti et al., (2018), about the hollows present in Dominici crater.
Moreover, few isolated hollows were identified present on both crater floors and few cases on the wall.

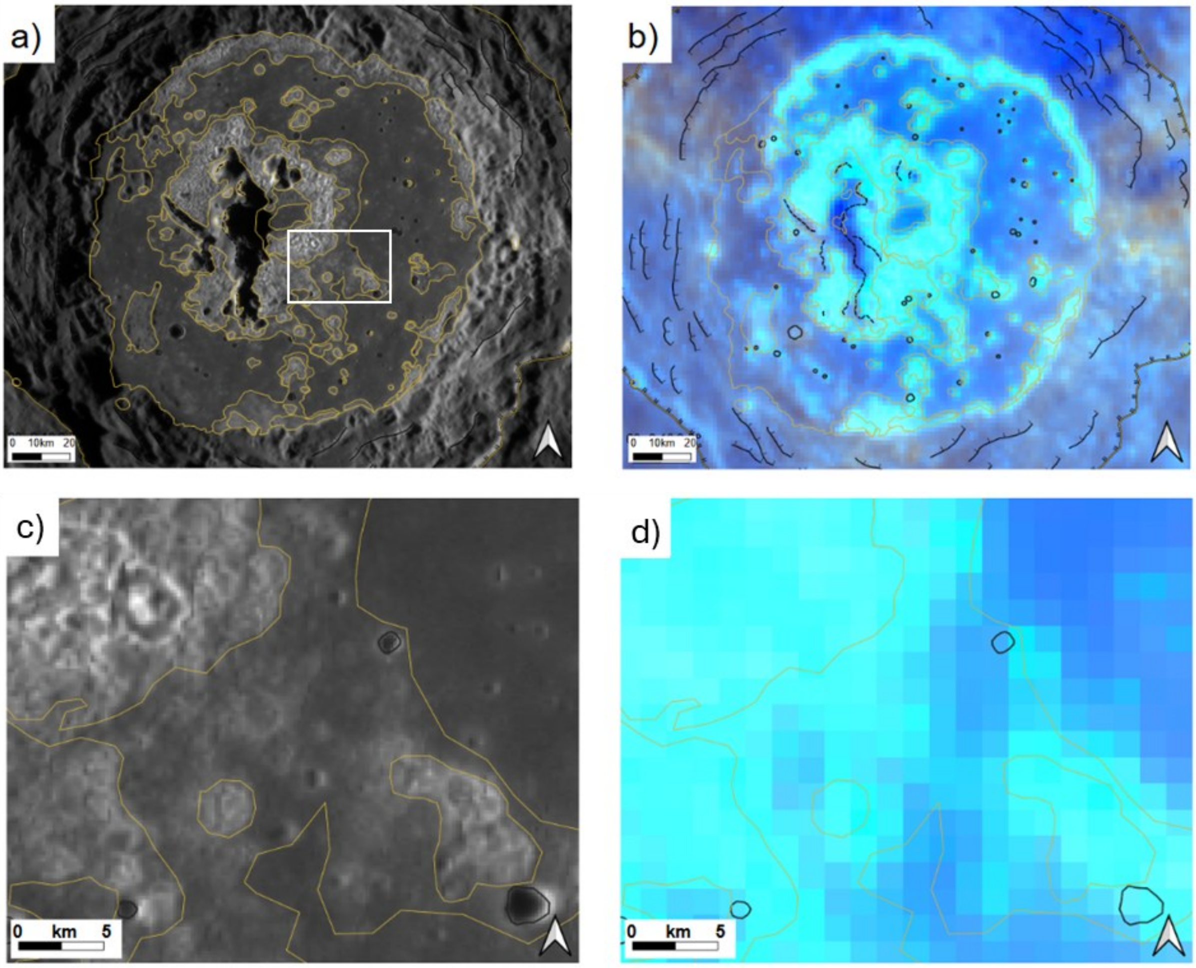

Fig. 21: Focus of the Warhol crater map for a comparison between a NAC image (a) and the global scale enhanced color base map on PC2, PC1, 430/1000 RGB (b) to show how the hollow clusters were selected and separated from the hollow fields. Can be observed that the color variation in the enhanced colour mosaic map doesn't make a clear distinction between the two different hollows categories, thus making the comparison with the NACs crucial to highlight those differences. c) Detail of Fig. 14a with a zoom (white box in Fig. 14a) to make more clear how the hollow clusters were separated from the hollow field in a NAC image and d) the relative enhanced colour mosaic RGB.

3.1.2 Hopper crater

The Hopper crater map (Fig. 22) shows a well defined rim and wall, permitting to consider this crater as a relative fresh one in accordance with the previous identification a C3, indicative for craters with sharp, intact rims and well-preserved central peaks (Giacomini et al., 2022).

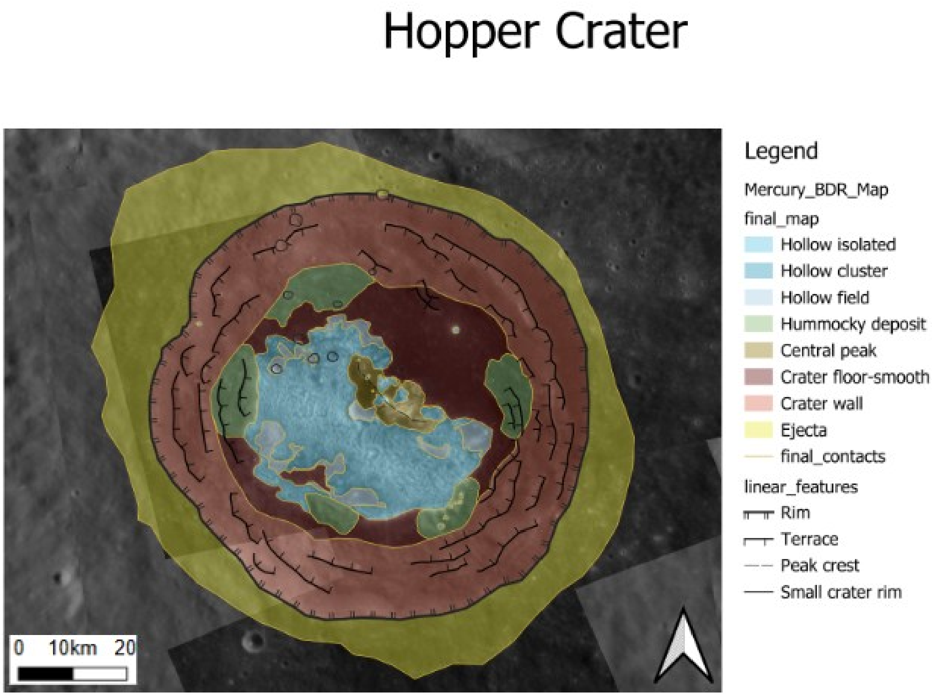

Fig. 22: High-resolution geological map of the Hopper crater (304° N, 12° W, Kuiper quadrangle H-06, 36 km diameter) created with the tool mappy in QGIS using a monochrome BDR base map (256 pixels per degree, ~166 m/p) and NACs (70 m/px) as a background.

The ejecta, identified in the map with a yellow colour only as its proximal ejecta, show a relative reduce extension than the others, coherent with the smaller dimensions of the crater itself.
The terraces homogeneously spread all around the crater wall, which host a small isolated hollow of an 800 m diameter. A small central peak crest orientated North-West with 5 hollow cluster with a mean diameter of around 3 km.
The floor shows a rough surface, moderately affected by secondary craters or it is covered by smooth deposits, where above there are very few small secondary craters with a diameter ranging from 1.44 km to 2.35 km. The floor hosts some hummocky deposit in the north-west and south-west areas near the contact between the floor and the wall of the crater (see Fig. 23 for comparison).
Note that Hopper crater is the smallest studied and the Southern, which imply, for how the orbit of MESSENGER was designed (e.g. Denevi et al. 2018), the lowest resolution of the images. This has an impact on the resolution of the outcome of the morphostratigraphic map and the enhanced RGB.

There are few isolated hollows heterogeneously distributed between the crater wall, floor and the peak. The central portion is characterized by a massive hollow cluster around the central peak (Fig. 24). Mostly in the south-west portion of the area, marginally to the cluster there are small portions of hollow fields.

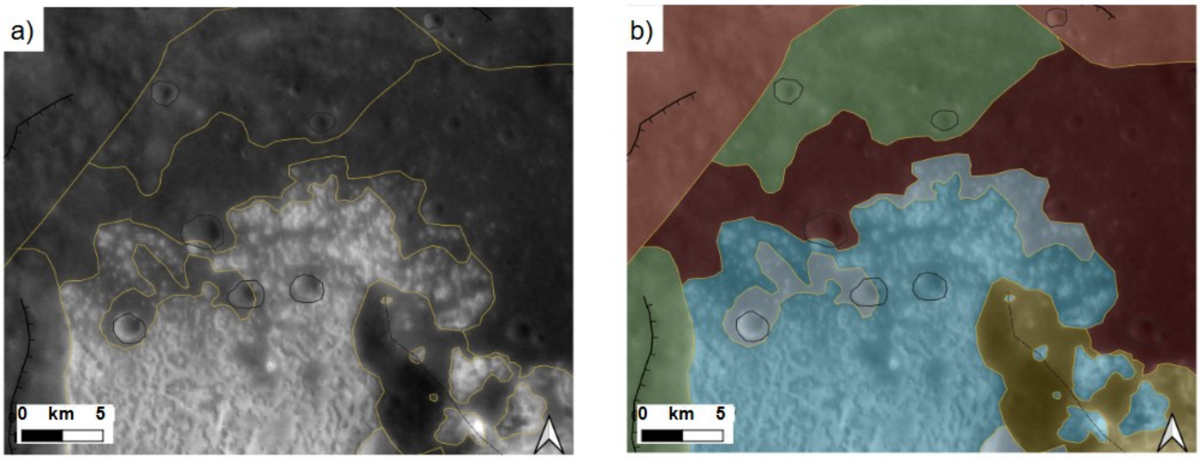

Fig. 23: Focus of the Hopper crater map for a comparison between a NAC image (a) and the created map to see the contact among geomorphological units. In the right (b) image an inset of the final map permit to highlight the units like crater wall (bright brown), crater floor-smooth (dark brown), hummocky deposit (green), crater peak (yellow), hollow cluster (cyan) and hollow field (light cyan).

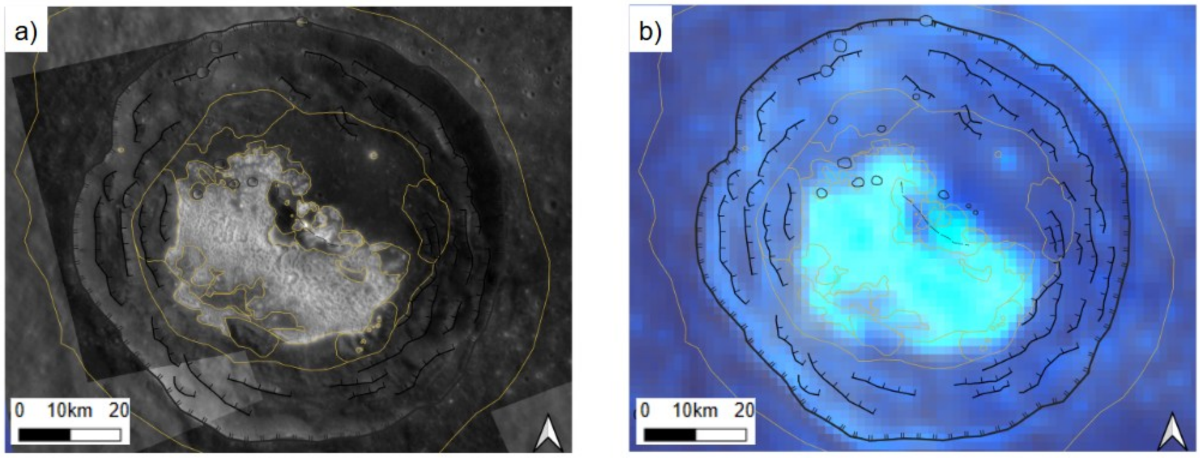

Fig. 24: Focus of the Hopper crater map for a comparison between a NAC image (a) and the global scale enhanced color base map on PC2, PC1, 430/1000 RGB (b) to show how the hollow clusters were selected and separated from the hollow fields. Can be observed that the spectra in the enhanced colour mosaic map don't make a clear distinction between the two different hollows categories, thus making crucial the comparison with the NACs to highlight those differences.

3.1.3 Eminescu crater

Eminescu crater map (Fig. 25) shows a well defined rim and wall, permitting to consider this crater as a relative fresh one in accordance with the previous identification a C3, indicative for craters with sharp, intact rims and well-preserved central peaks (El Yazidi et al., 2024).

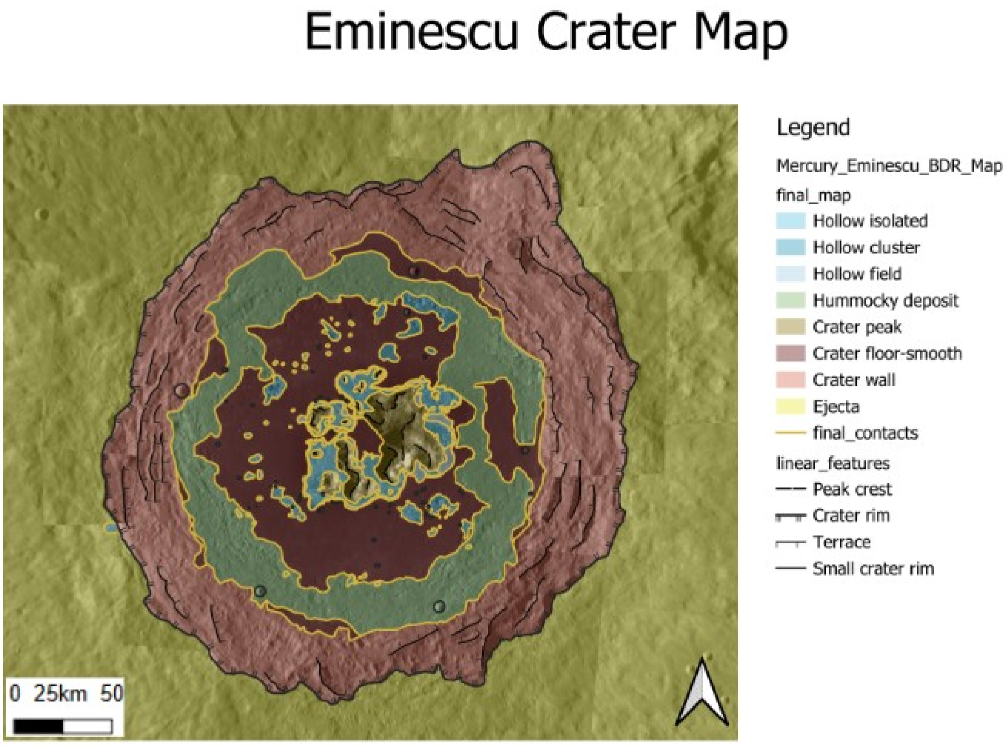

Fig. 25: High-resolution geological map of the Eminescu crater (114° N, 10° E, Eminescu quadrangle H-09, 129 km diameter) created with the tool mappy in QGIS using a monochrome BDR base map (256 pixels per degree, ~166 m/p) and NACs (130 m/px) as a background.

Eminescu is the biggest studied crater and so it can be easily visible that the yellow proximal ejecta covers a vaster area in comparison with the other craters. The wall is characterized by a more irregular rim, less rounded, and many terraces distributed all along the crater wall, mainly localized in the North-West and South-East portion.
The crater shows the central peak which is characterized by two predominant central crests in the middle of the crater with a North-South alignment, and smaller outcrops coming on the North-East side (e.g. see a zoom of the map in fig. 26).

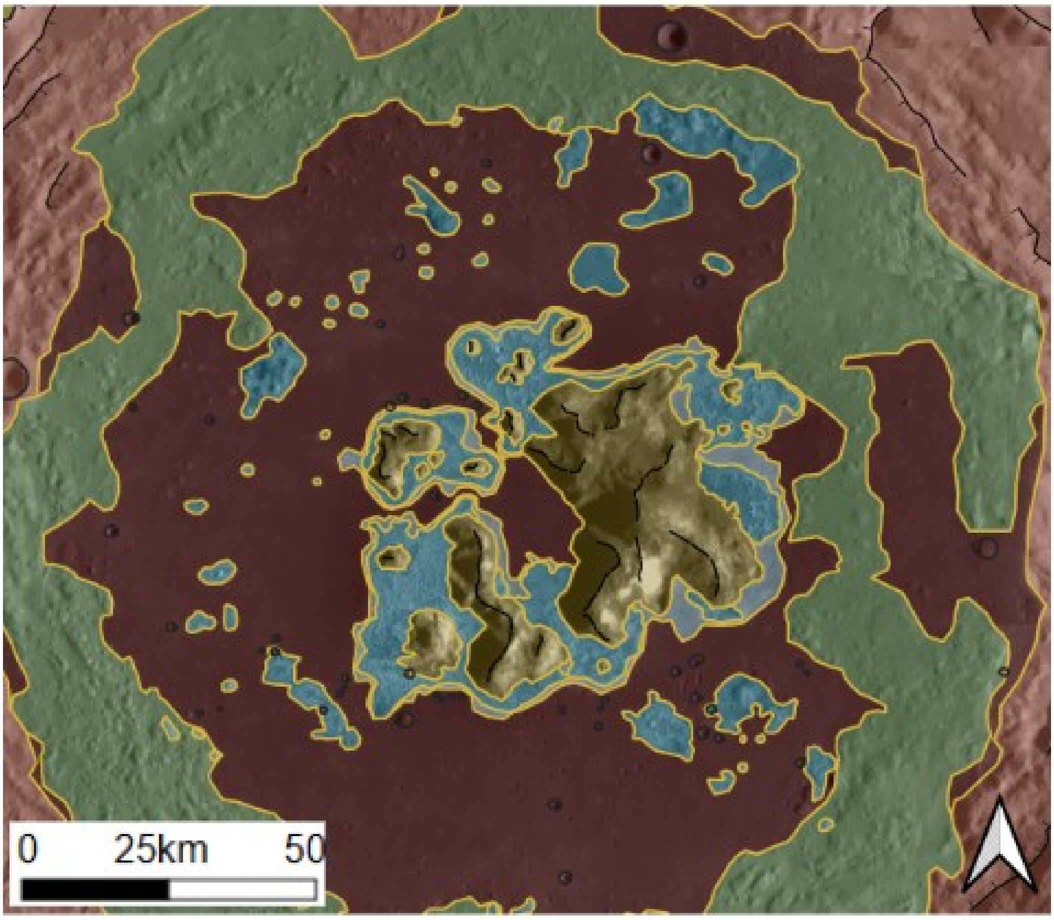

Fig. 26: Detail on the innermost part of the Eminescu crater map (Fig. 25) created with the tool mappy in QGIS.

The floor shows a rough surface, moderately affected by secondary craters with a mean diameter of 2.5 km, or it is covered by smooth deposits and is characterized by a large infilling of a very smooth unit which can be attributed to effusive volcanic deposit although an impact origin cannot be excluded (Denevi et al., 2013; Whitten et al., 2014). Moreover, all around the contact between crater wall and floor can be noted that there are more roughly/irregular terrains which can be indicated as hummocky deposits similar to the case of Dominici crater reported by Lucchetti et al. (2018) (see Fig. 27 for comparison between units).
The crater floor also shows a heterogeneously spread distribution of secondary narrow craters ranging from 7 km to 1.8 km of diameter.

Concerning the hollows features (Fig. 28), we can note that the isolated are mostly in the floor area between peak crest and the crater wall, the cluster hollows are mainly in the central part surrounding the central peaks, but some of them can be seen between the hummocky deposit and the central peak. The hollow field makes a contour to the central hollow cluster that are around the central peaks. Following the same approach used by Lucchetti et al., 2018, about the hollows present in Dominici crater.

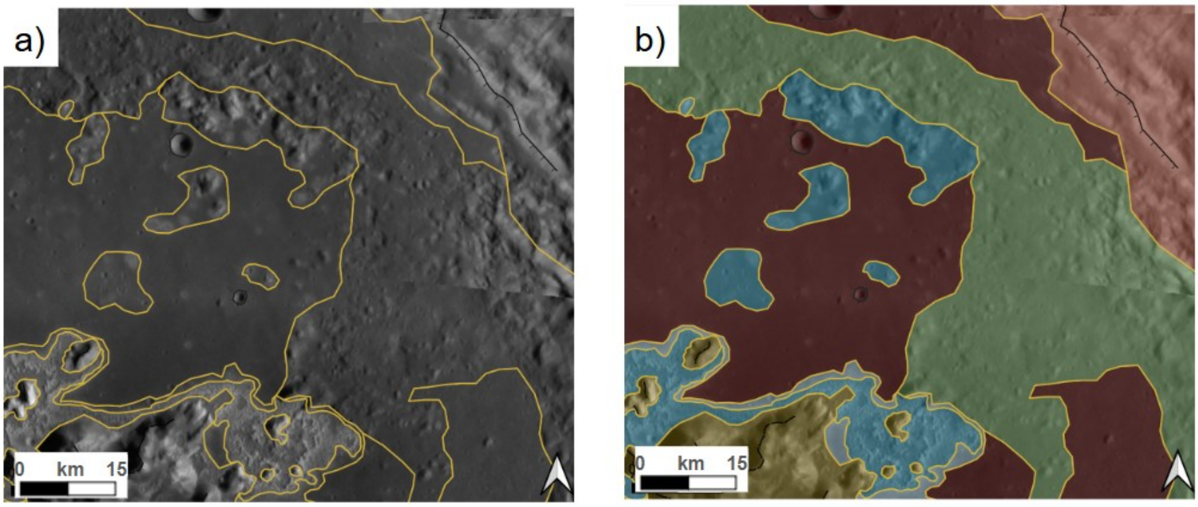

Fig. 27: Focus of the Eminescu crater map for a comparison between a NAC image (a) and the created map to see the contact among geomorphological units. In the right (b) image an inset of the final map permit to highlight the units like crater wall (bright brown), crater floor-smooth (dark brown), hummocky deposit (green), crater peak (mustard yellow), hollow cluster (cyan) and hollow field (light cyan).

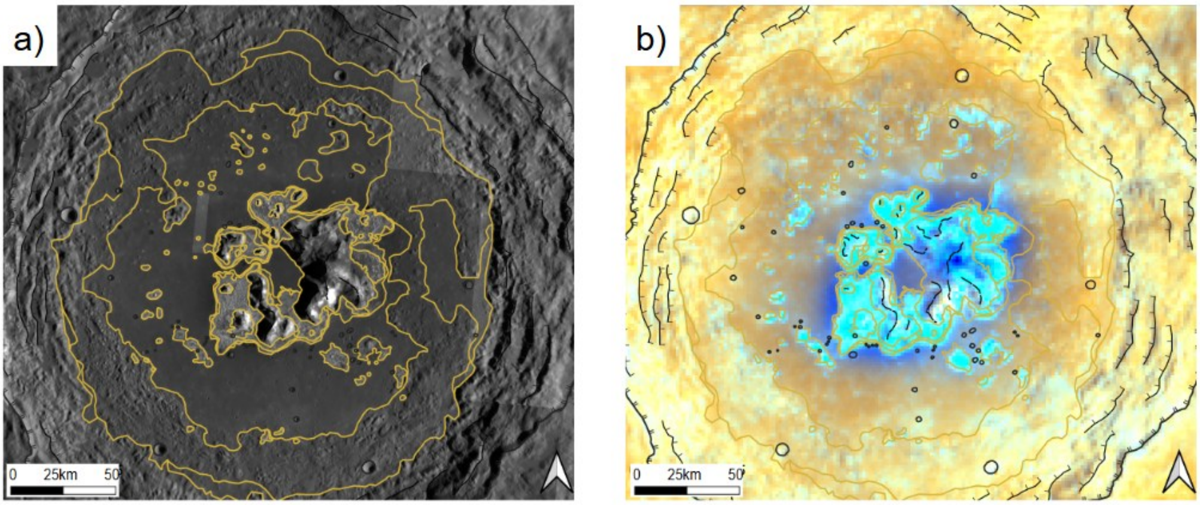

Fig. 28: Focus of the Eminescu crater map for a comparison between a NAC image (a) and the global scale enhanced color base map on PC2, PC1, 430/1000 RGB (b) to show how the hollow clusters were selected and separated from the hollow fields. Can be observed that the spectra in the enhanced colour mosaic map don’t make a clear distinction between the two different hollows categories, thus making crucial the comparison with the NACs to highlight those differences.

3.1.4 Sander crater

The final map is the one of the Sander' crater (Fig. 29), which exhibit a well defined rim and wall, permitting to consider this crater as a relative fresh one in accordance with the previous identification a C3, indicative for craters with sharp, intact rims and well-preserved central peaks (Macinelli et al., 2016).

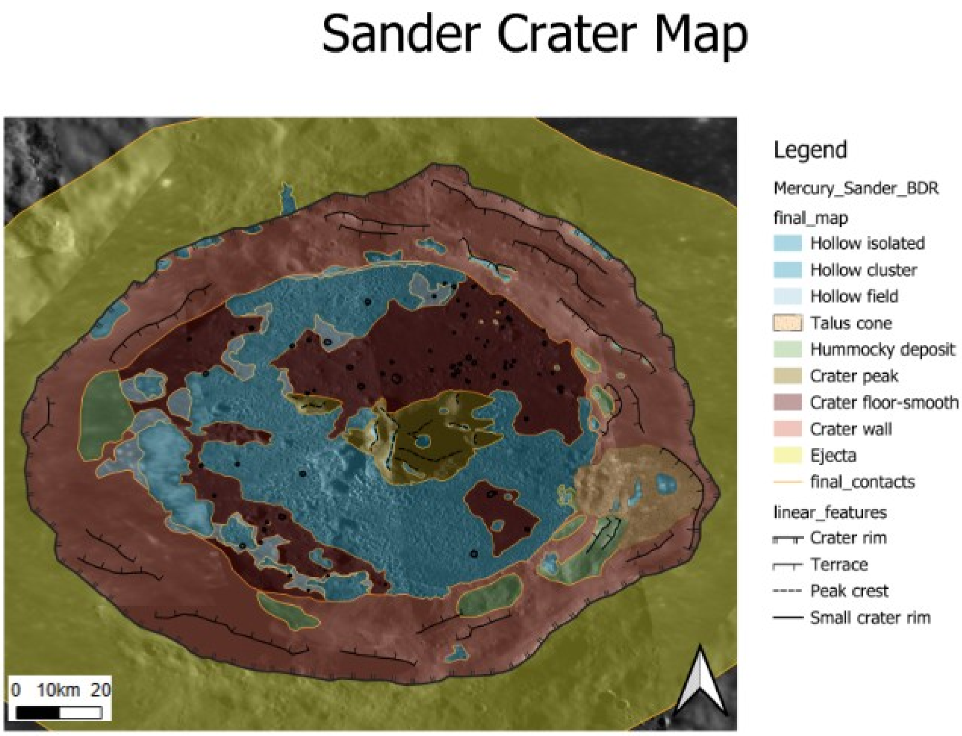

Fig. 29: High-resolution geological map of the Sander crater (154° N, 42° E, Raditladi quadrangle H-04, 47 km diameter) created with the tool mappy in QGIS using a monochrome BDR base map (256 pixels per degree, ~166 m/p) and NACs (45 m/px) as a background.

The ejecta, represented with a yellow coloration as proximal ejecta, shows themself rayed and bright and can extend for over 100 km from the crater rim.
The wall is characterized by few terraces distributed all along the crater wall, mainly localized in the North-East portion. The wall hosts few isolated hollows and even hollow cluster with the diameters that vary from 1.25 km to 5.53 km.
Fig. 30 shows some of the different morphologies present in the crater, which are described in the following lines.
On the East / South-East portion of the wall there are some hummocky deposit deposits similar to the case of Dominici crater reported by Lucchetti et al. (2018), associated with a talus cone, defined as a gravitational deposit that is uniformly distributed along the foot of the scarp and shows no defined source of origin (Lucchetti et al., 2018).

The crater shows the central peak which is characterized by three predominant central crests in the middle of the crater where, two with a North-South alignment, one with an East-West alignment and smaller outcrops with the alignment of East-West and North-South, coming on the East side.
The floor shows a rough surface, moderately affected by secondary craters or it is covered by smooth deposits and is characterized by a large infilling of a very smooth unit which can be attributed to effusive volcanic deposit although an impact origin cannot be excluded (Denevi et al., 2013; Whitten et al., 2014). Moreover, in the North-West section it can be noted that there are more roughly/irregular terrains which can be indicated as hummocky deposits similar to the case of Dominici crater reported by Lucchetti et al. (2018).
The crater floor also shows a wide distribution of narrow craters ranging from 440 m to 2.5 km of diameter, probably secondary.

The hollows here are present wider in the floor (see Fig. 31), superimposed to the smooth infilling, near the central peak but even around the contact from the floor and the wall and partially on other points of the floor. The isolated hollows are heterogeneously spread mainly on the crater wall and some on the crater floor, there is a big portion of the floor that host hollow clusters that covers the floor from the North to the South passing near the central peak, other than a big cluster on the West-most portion of the floor. The hollow field surround the clusters especially in the North and West parts. This distinction was the same used by Lucchetti et al., 2018, about the hollows present in Dominici crater.

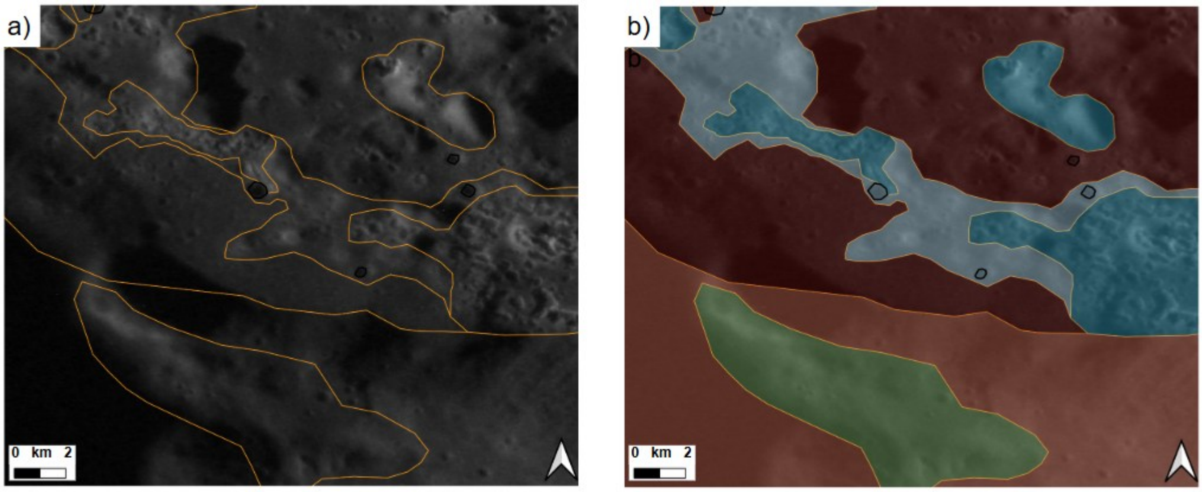

Fig. 30: Focus of the Sander crater map for a comparison between a NAC image (a) and the created map to see the contact among geomorphological units. In the right (b) image an inset of the final map permit to highlight the units like crater wall (bright brown), crater floor-smooth (dark brown), hummocky deposit (green), hollow cluster (cyan) and hollow field (light cyan).

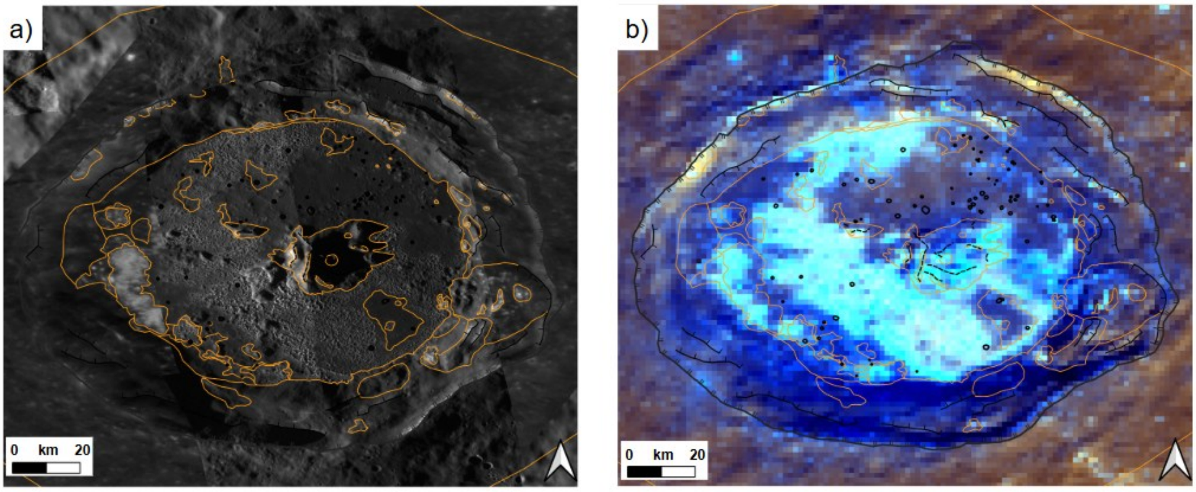

Fig. 31: Focus of the Sander crater map for a comparison between a NAC image (a) and the global scale enhanced color base map on PC2, PC1, 430/1000 RGB (b) to show how the hollow clusters were selected and separated from the hollow fields. Can be observed that the colour variations in the enhanced global colour mosaic map don't make a clear distinction between the two different hollows categories, thus making crucial the comparison with the NACs to highlight those differences.

3.2 Spectral

The spectral analysis was done with the ENVI software that enlightened some interesting results for each crater.

3.2.1 Spectral analysis of Warhol crater

The studied areas for spectral analysis of Warhol crater (Fig. 32) involved some regions among the crater, considering the hollow clusters as well as other peculiar regions where we performed spectra collection. These spectra collections aim to investigate the variability of:

1. Hollows clusters vs hollows fields.
2. Hollows spectral signature degradation in function of the surroundings material.
3. The different terrains in the area of the craters.

These investigations have been developed as single pixel comparison moving from a region to another and collecting region of interest (ROI) of several points on the different terrains or cross-cutting more than one terrain. We plot the comparison as both reflectance spectra and ENVI automatic continuum removed with the aim to highlight the main differences and attempt attribution of potential absorptions. (Fig. 34); a spectral analysis for the portion of area number 3 and ROI's analysis for the portion of area number 7 and 8. Other than that two more ROIs were collected for studying the crater floor and the outer region of the crater that exhibit an interesting coloration.

The selections of the different regions were based on a first wide survey of all the crater, moving in different places and acquiring experience on the spectral variability, in addition we used the color variability of the ad-hoc produced enhanced color mosaics, with variable stretching of the R, G and B channels, for different sites. In Fig. 33 we report the results of two of them with a grey scale image of the investigated region.

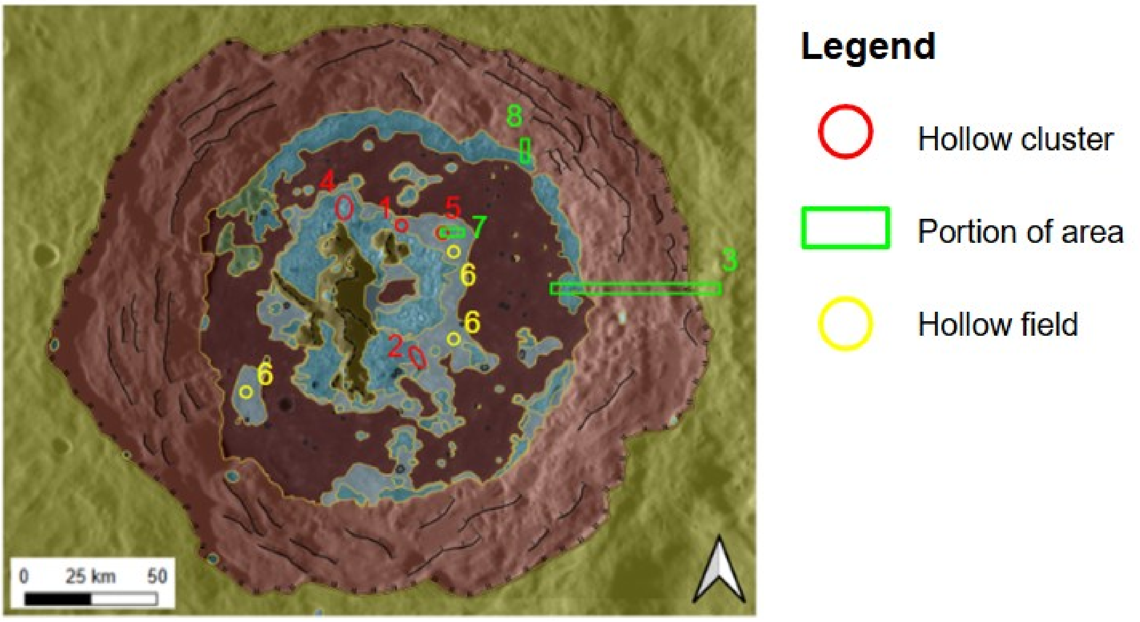

Fig. 32: Modified after figure 19, with implemented the site where spectral acquisition was detailed, done and discussed in the following figures.

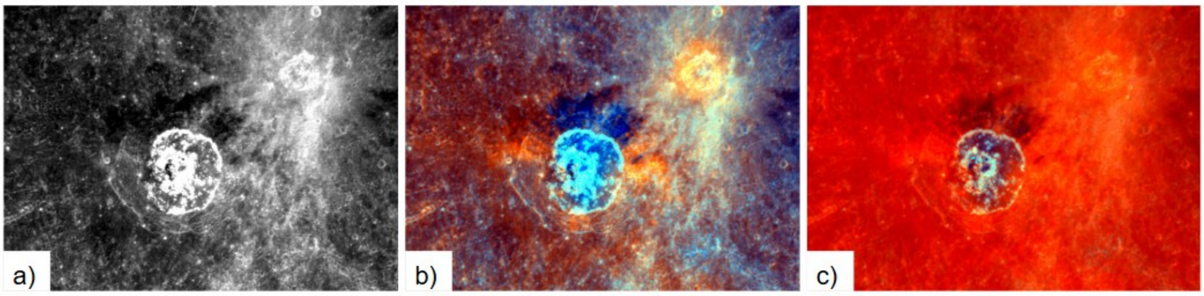

Fig. 33: Respectively, a) image in grey scale of the band 4 at 630 nm, b) enhanced color mosaic obtained on a high resolution cube based on PC2, PC1, 430/1000 with the RGB stretch values of 0.033, 0.049 for R; 0.171, 0.319 for G; 0.462,0.938 for B and c) the same RGB within a stretch on the Hollows dominated region on Warhol crater with the RGB stretch values of 0.029, 0.048 for R; 0.171, 0.398 for G; 0.516. 0.765 for B. The color mosaic for Warhol crater has been produced at 650 m/px.

Hollows:

For the hollows the differences in coloration were applied for collected spectra from a lighter cyan coloration to a darker one till blue, always indicating the west-to-east sampling.
For the hollows the differences in coloration on enhanced color images were applied for collected spectra from a lighter cyan coloration to a darker cyan, which in our case is always indicating the west-to-east sampling and from the inner to outer of the crater.
The 4 selected hollows cluster show always the same spectra signature with a slight variegation in reflectance level and with a possible trend from the “inner” region (cyan) vs the “external” regions (dark-cyan to blue). Nevertheless, all the investigated cases (Fig.34-37) show the presence of a relative bluer slope with respect other regions, due to a relative higher visible reflectance with respect to the near-infrared, a general high reflectance for Mercury terrains and the presence of a putative absorption around wavelengths 630-750 nm, with an inflation towards the longer wavelengths (900-1000 nm).
These spectral properties are evident in the single pixel transects shown in the following Fig. 34-37 as well as in the ROIs averages spectra of tens of pixels.

1) *Hollow cluster 1:*

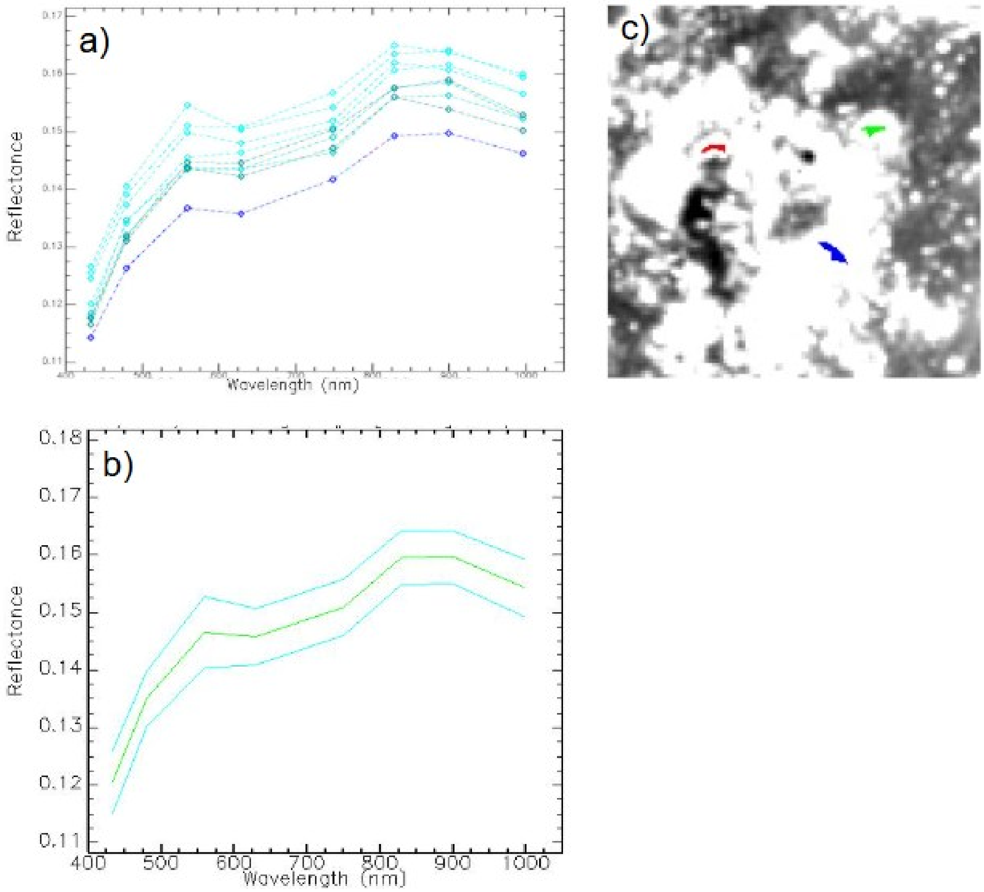

Fig. 34: Spectral analysis of the hollow cluster 1 (a) and ROI’s mean (green) between standard deviation (cyan) and the (c) ROI’s actual coverage (green area). Well visible absorption at 630 nm, typical of hollows with an inflection around 1000 nm wavelength.

2) Hollow cluster 2:

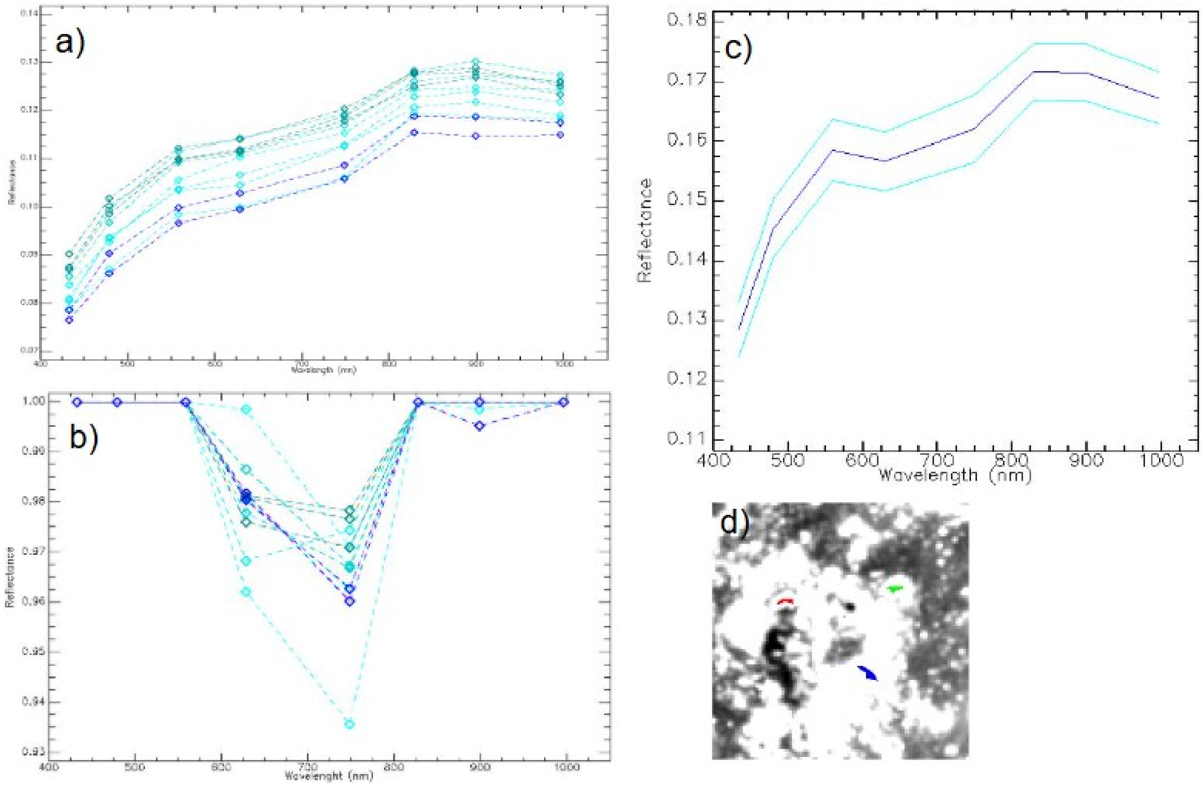

Fig. 35: Spectral analysis of the hollow cluster 2 (a) with continuum removed (b) and ROI's mean (blue) between standard deviation (cyan) in c). In (d) ROI's actual coverage (blue area).

3) Hollow cluster 4:

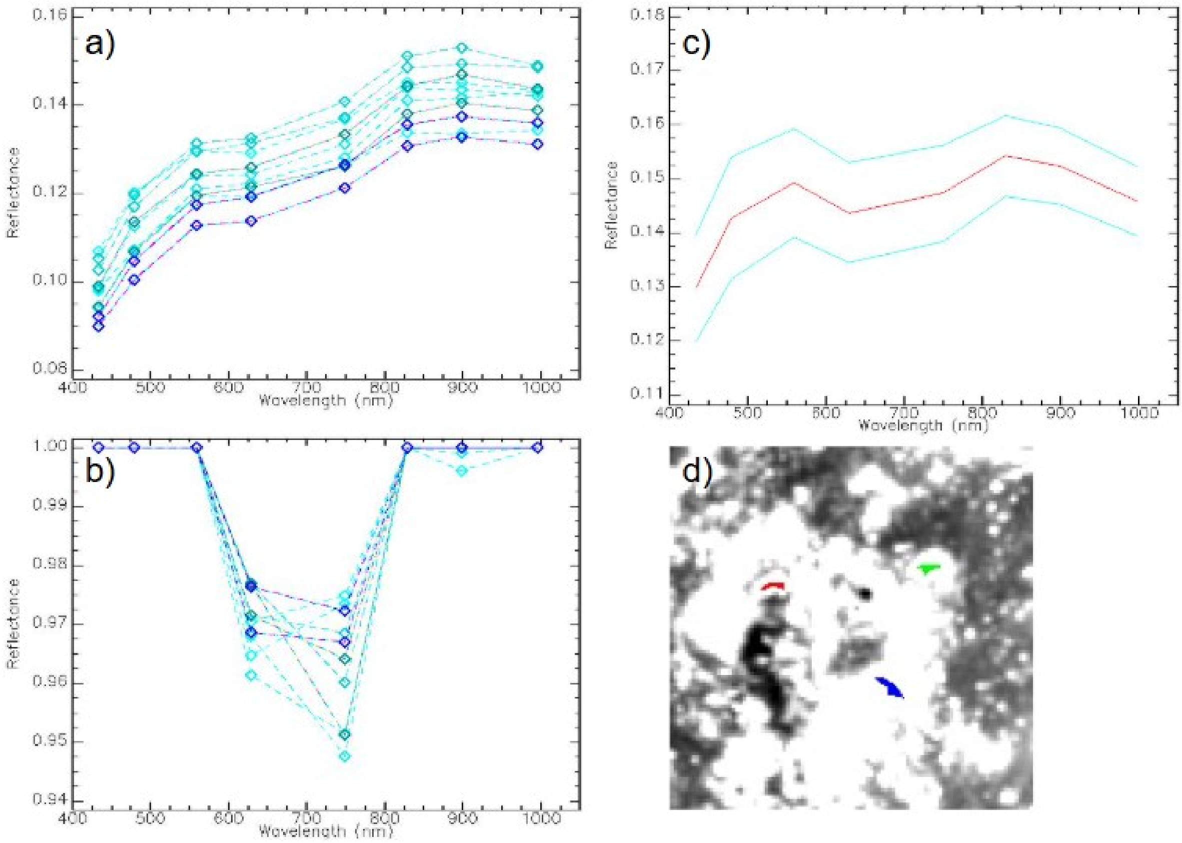

Fig. 36: Spectral analysis of the hollow cluster 4 in a) with continuum removed in b) and ROI’s mean (red) between standard deviation (cyan) and the in c). In d) ROI’s actual coverage (red area).

4) Hollow cluster 5:

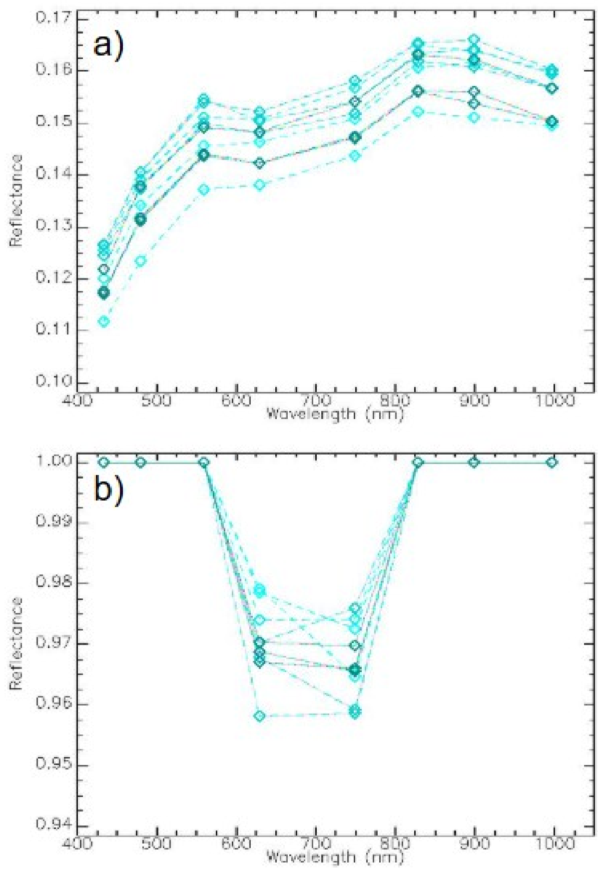

Fig. 37: Spectral analysis of the hollow cluster 5 in a) with continuum removed in b). This spectra was taken by selecting pixel per pixel only the ones that were clearly identifiable as hollows (avoiding the surroundings). It can be noted that the plot is characterized by homogeneous spectra following the same trend; notable even in b) the continuum removed analysis. Generally, the reflectance is higher than the other hollows spectra collected.

<u>ROIs:</u>

We select some region of interest to investigate the spectral properties of other areas among the crater regions, to compare the variability with respect to the hollows cluster, as well as the heterogeneity in the nearby material of the hollows.
First, we considered three regions among those areas identified as hollow fields, so a portion of the hollow's dominated area but with a lower hollow density and more characterized by the halo surrounding the hollows. Fig. 38 shows their variability, 38a-c for the three different ROI with the respective standard deviations, whereas in Fig.38d we compare the three averages. All of them are relatively dark (ROI1 and 2 are the darker), with respect to the spectra of Hollows cluster, slightly redder, with absent (or very weak) absorption, which can clearly be detected only in ROI3, and no inflation towards 1000 nm.
Nevertheless, when we investigate a transect from hollow cluster to hollow field, we clearly evidence a higher variation of the standard deviation moving from spectra common to the two different areas, but the average still characterized the region as a hollow-like (Fig.39). Conversely when we characterized a ROI from a hollow cluster to the surrounding material of

the wall, we can clearly highlight a higher contribution on the average of the material external to the hollows, which is strongly darker (Fig.40).
In Fig. 41 we consider a larger transect with respect to the previous and so instead to show only the average we highlight a collection of spectra from the different crossed portions. The spectra vary from the crater floor where can be identified in because they don't show inflection at 1000 nm and have a weaker absorption dominated by the 750 nm wavelength (Fig.41b). This wavelength has often a lower reflectance all around the planet at it is not considered as a true absorption if present alone since it is suggested as a possible instrument artifact (Denevi et al. 2018). From the border of the hollows cluster up to the end of this unit the spectra show the higher reflectance as well the most characterizing absorption at 630-750 nm as well as the inflation at longer wavelengths. Moving toward the wall the spectra are darker (reported in orange in the figure) we have the darker spectra with a weak absorption at 630 nm due probably to the "contamination" with the proximity of the hollow cluster; they do not have inflection at 1000 nm as well.
Finally, we characterized the material from outside the crater among the crater ejecta, highlighting as they are quite homogeneous, dark and red, without evidence of absorption, with a region at N-NW (green spectra in Fig.42) showing the darker spectra also in the near-infrared, and so a bluer slope.

5) Hollow field (6):

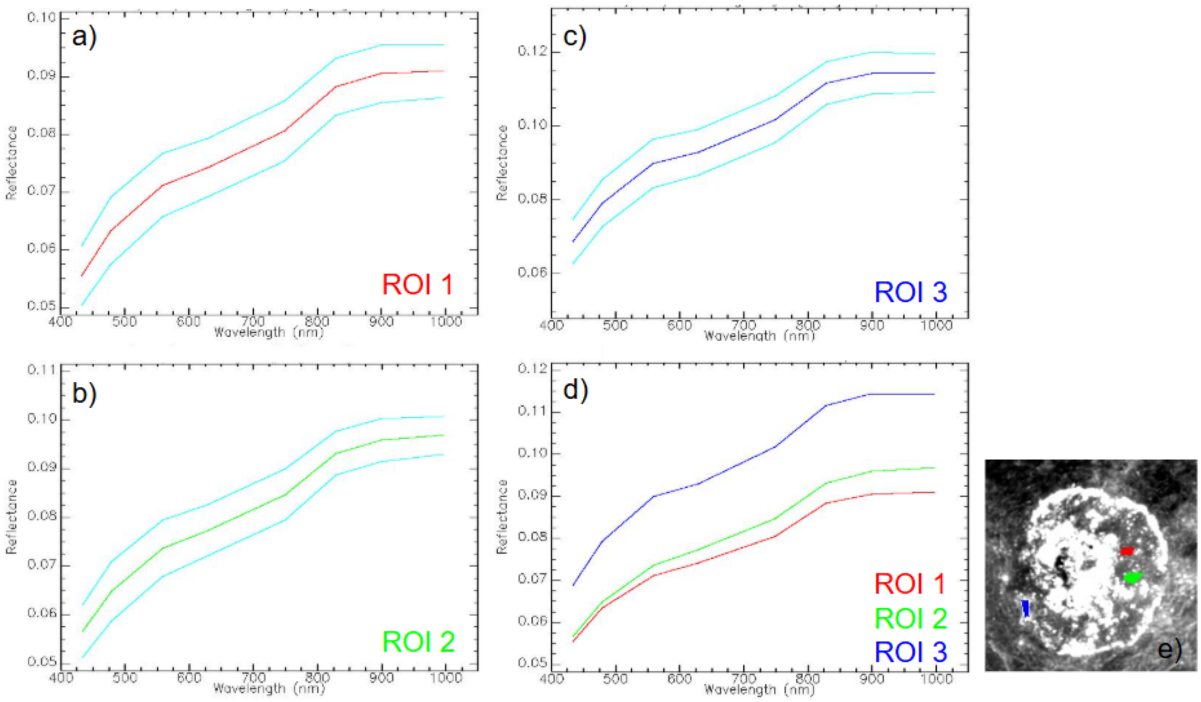

Fig. 38: ROI's mean for the site a (red), b (green), c (blue) between standard deviation (cyan); ROIs comparison in d) and in e) ROI's actual coverage of the hollow fields.

6) ROI of hollow cluster to hollow field (7):

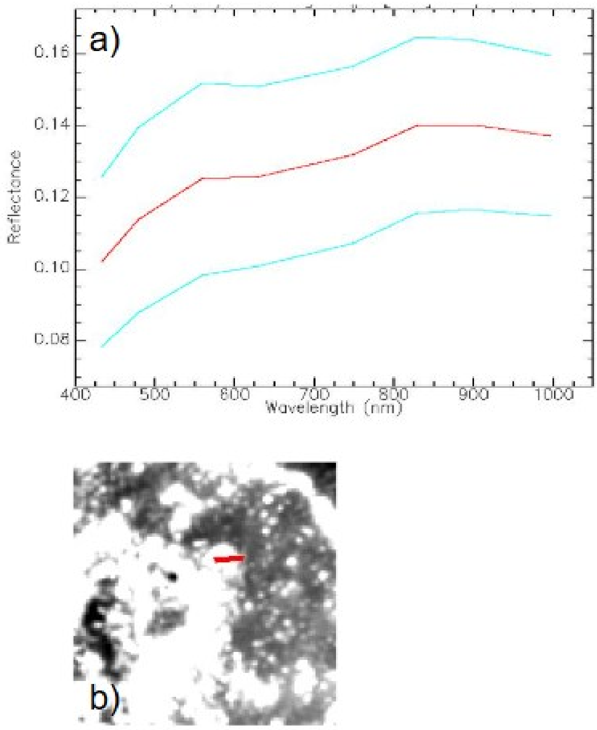

Fig. 39: ROI's mean (red) between standard deviation (cyan) and the (c) ROI's actual coverage (red area) that goes from an area of hollow cluster to the adjacent hollow field.

7) ROI of hollow cluster to crater wall (8):

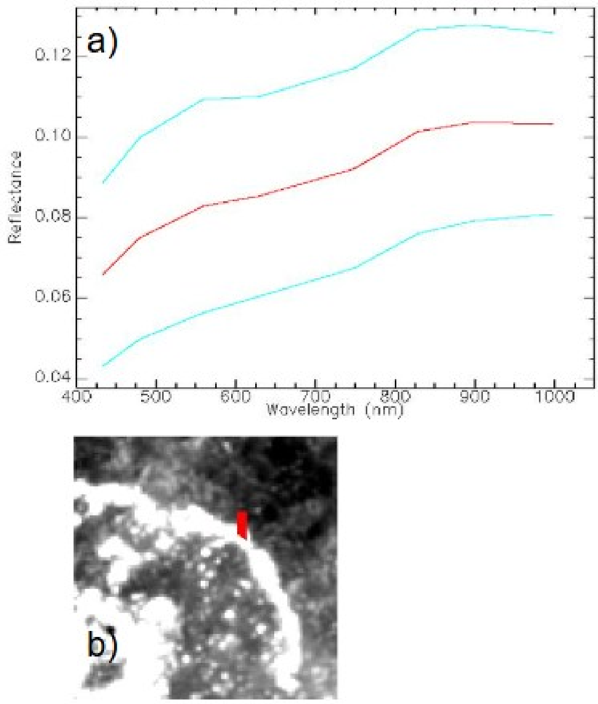

Fig. 40: ROI's mean (red) between standard deviation (cyan) and the (c) ROI's actual coverage (red area) that goes from an area of hollow cluster to the adjacent crater wall.

8) Portion of area from crater floor to proximal ejecta (3):

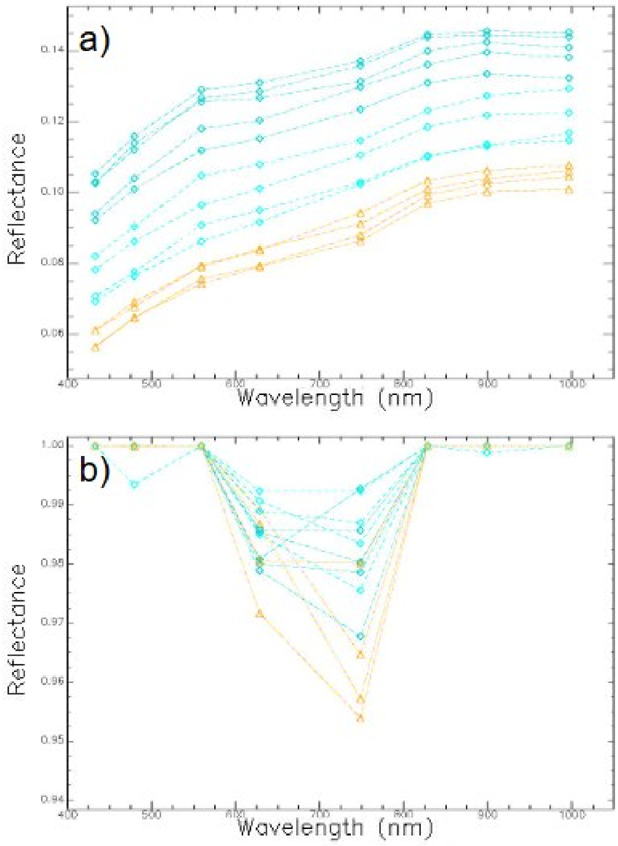

Fig. 41: Spectral analysis of the portion of area that goes (West to East) from the crater floor to proximal ejecta (a) with continuum removed (b).

9) ROI of Proximal ejecta:

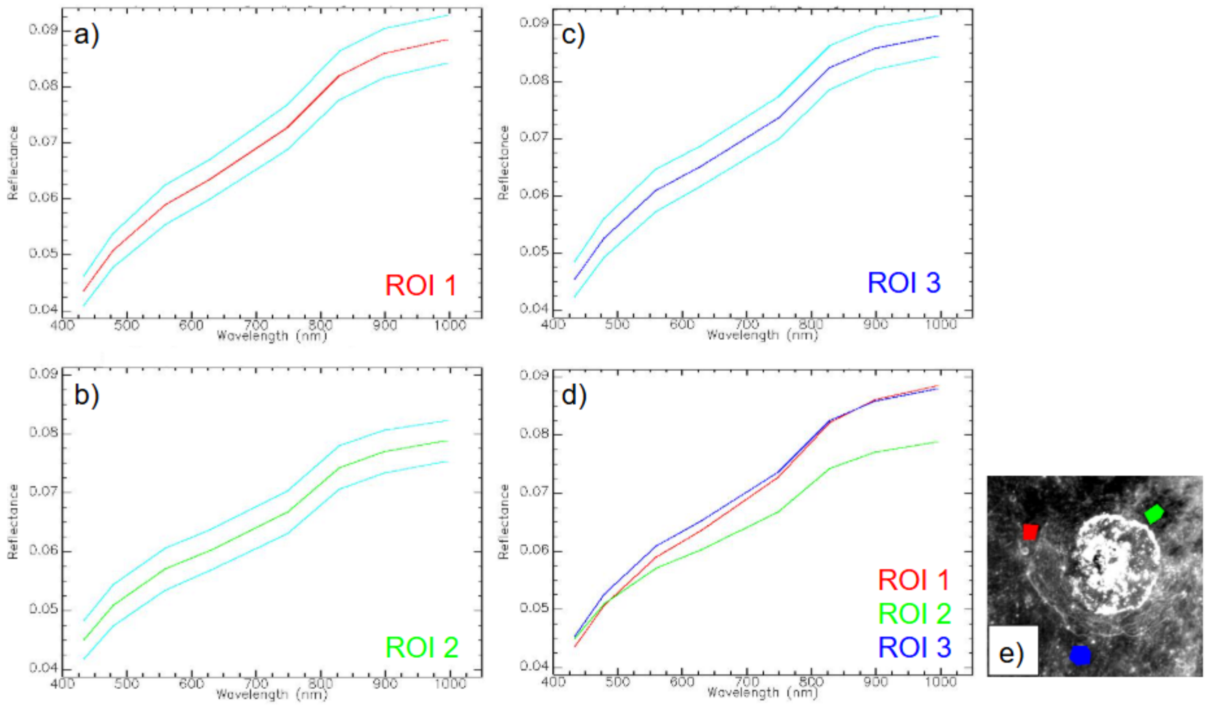

Fig. 42: ROI's mean for the site a (red), b (green), c (blue) between standard deviation (cyan); ROIs comparison in d) and in e) ROI's actual coverage of different sites in the proximal ejecta.

3.2.2 Spectral analysis of Hopper crater

Hopper crater spectral analysis sites (**Fig. 43**) were studied following the approach described in Warhol crater 3.2.1 section. The resolution of the multispectral image for this case is the lower at 1600 m/px. Here we investigated (Fig. 43a) 3 hollow clusters, of which, the hollow cluster number 4 were taken considering pixel per pixel the hollows recognizable because of the low resolution and a higher heterogeneity of the hollows than the ones in Warhol. Then we considered the area (3) where we collected some spectra for, from west to east, hollow cluster, crater floor, crater wall and proximal ejecta. ROIs of all the above locations were taken (Fig. 43b) and, moreover, other ROIs were selected to study the proximal ejecta, the transition from hollow cluster, hummocky deposit, crater wall and proximal ejecta. Finally, a ROI consisting of a portion of the crater smooth-floor and a portion near the inner crater wall where the spectral signature was brighter. These chosen areas were guided by a systematic comparison among the images in Figure 44).

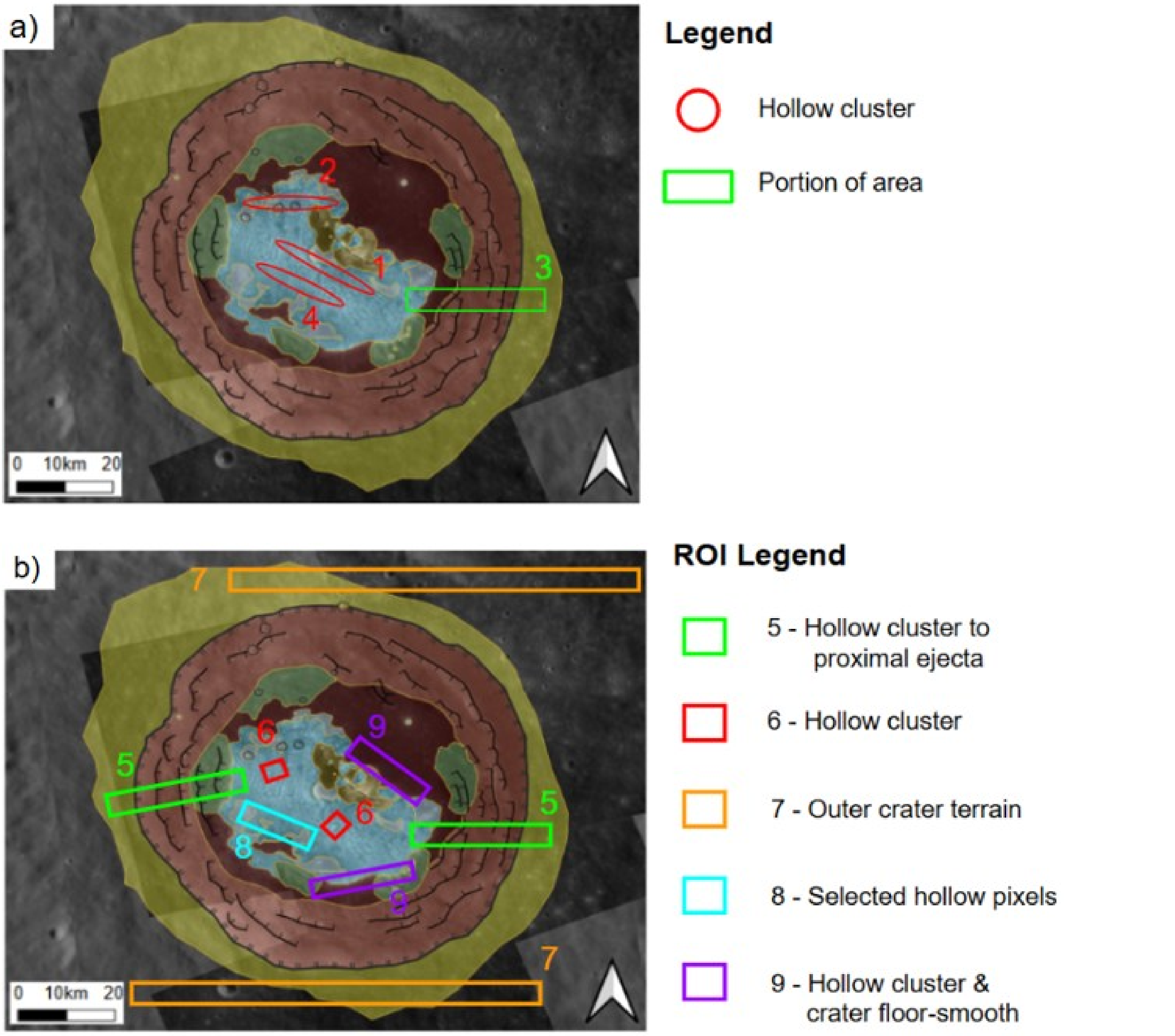

Fig. 43: a) Modified after figure 22, which implemented the site where spectral acquisition was detailed, done and discussed in the following figures.
b) Modified after figure 22, with only where the ROIs were taken for a more clean visualization.

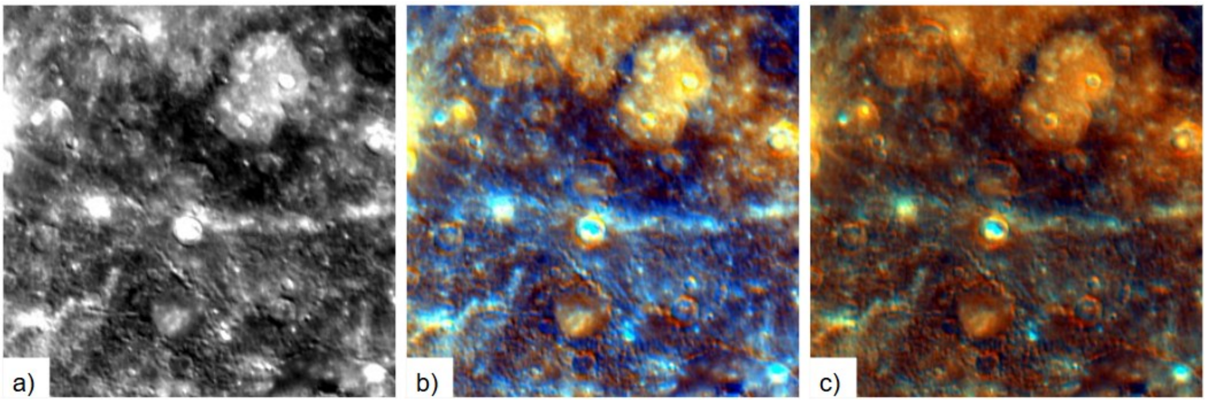

Fig. 44: Respectively, a) image in grey scale of the band 4 at 630 nm, b) enhanced color mosaic obtained on a high resolution cube based on PC2, PC1, 430/1000 with the RGB stretch values of 0.033, 0.041 for R; 0.153, 0.204 for G; 0.485, 0.554 for B; and c) the same RGB within a stretch on the Hollows dominated region on Warhol crater with stretch values of RGB

of 0.033, 0.146 of R; 0.162, 0.277 of G; 0.486, 0.658 of B. The color mosaic for Hopper crater has been produced at 1600 m/px.

<u>Hollows:</u>

For the hollows the differences in coloration on enhanced colour images were applied for collected spectra from a lighter cyan coloration to a darker cyan, which in our case is always indicating the west-to-east sampling and from the inner to outer of the crater.
The selected hollow clusters reported in Fig. 45, 46 and 47 show always similar spectra signature with a slight variegation in reflectance level and with a possible trend from the “inner” region (cyan) vs the “external” regions closer to the central peak (dark-cyan to blue spectra). Nevertheless, all the investigated cases (Fig.45-47) show the presence of a relative bluer slope, a general high reflectance, the presence of a putative absorption around wavelengths 630-750 nm, with an inflation towards the longer wavelengths (900-1000 nm) as already seen for Warhol Crater.

In particular the shown case of the cluster 4 (Fig. 43a and Fig. 49) show almost the identical spectral features attributed to the hollows in Warhol in this work as well in Dominici in previous work (e.g. Vilas et al. 2016), whereas in Cluster 1 and 2, closer to the central peak we clearly see some spectra with a weak absorptions around 830 nm, in some cases coupled with an absorption at 550 nm
In Fig. 48 instead we explored the variability from part of an hollows cluster moving out-side the crater (see site 3 in Fig.43a). The spectra colours go to cyan to a darker cyan proceeding to East for hollows, whereas orange is used for the crater wall and become darker on the proximal ejecta. It can be observed that the spectra with a higher reflectance are collected into the hollow cluster with a minimum at 630 nm and inflation towards 1000 nm. The spectra related to the crater floor-smooth are bright oranges that show an absorption band at 500 nm and 830 nm, similar to the one seen on the spectra closer to the central peak. Proceeding towards the ejecta of the crater with spectra reported in darker shades of orange are present dark spectra with no peculiar features, apart the 750 nm. As well as in the ROIs averages spectra of Fig. 52 where pixels of certain hollows were collected.

1) Hollow cluster 1:

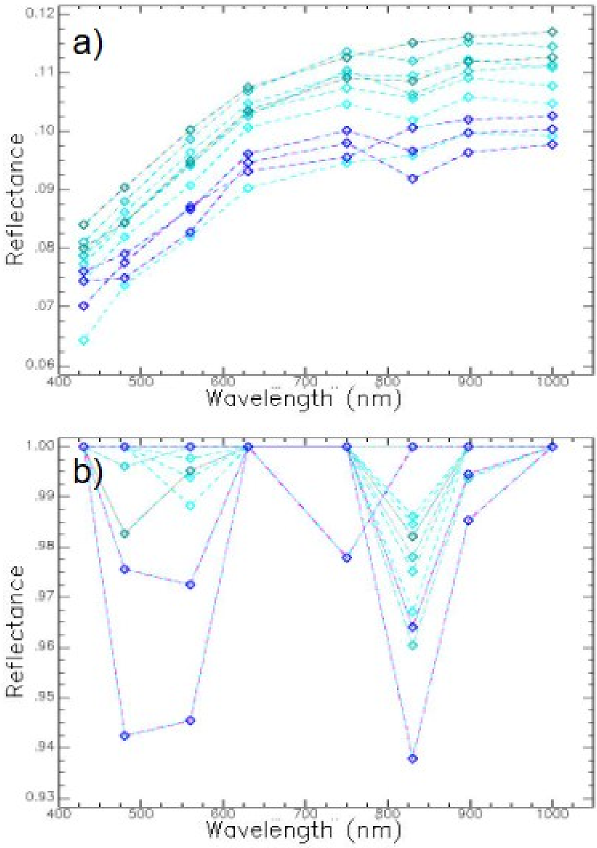

Fig. 45: Spectral analysis of the hollow cluster 1 in a) with continuum removed in b).

2) Hollow cluster 2:

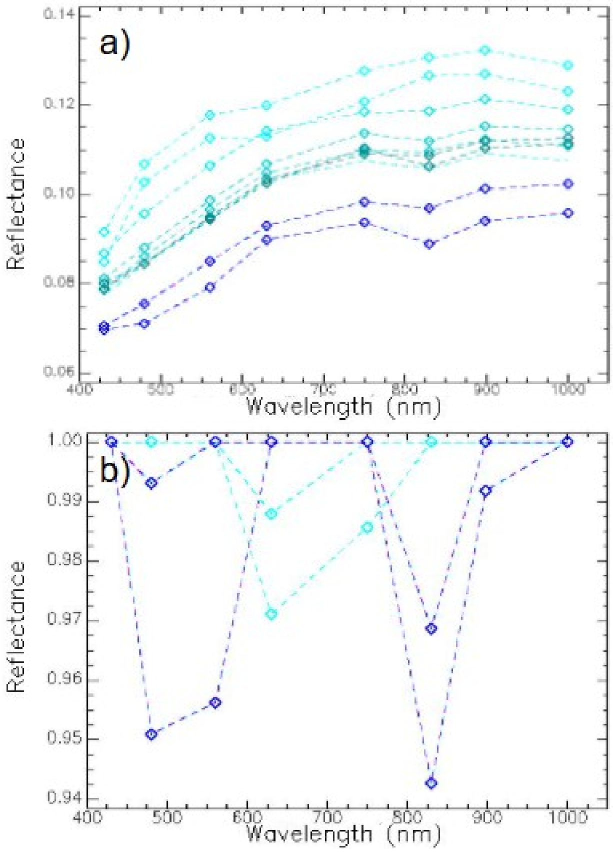

Fig. 46: Spectral analysis of the hollow cluster 2 (a) with continuum removed of the most indicative spectra (b). More heterogeneous reflectance in spectra is shown with a clearer absorption band at 630 nm for the cyan signatures with the classic inflection at 1000 nm. The blue spectra should be hollow field possibly contaminated by the crater floor-smooth.

3) Hollow cluster 4:

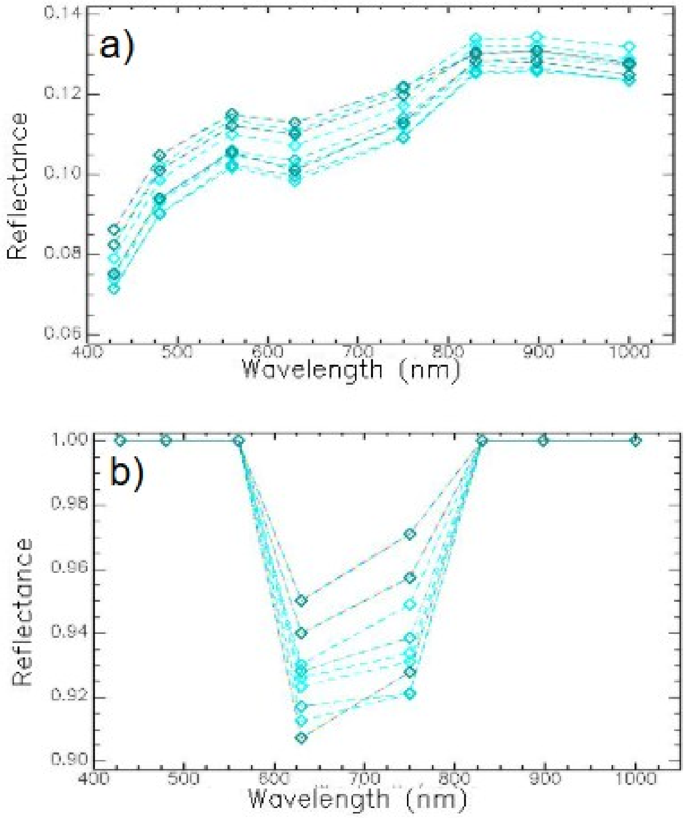

Fig. 47: Spectral analysis of the hollow cluster 4 (a) with continuum removed (b). Collected with precise pixels of recognizable hollow spectral signature. This type of sampling permit to show a more homogeneous spectra signatures collection with visible absorption band at 630 nm and the inflection at 1000 nm in a range from 0.07 to 0.13 reflectance values.

4) Portion of area from hollow cluster to proximal ejecta (3):

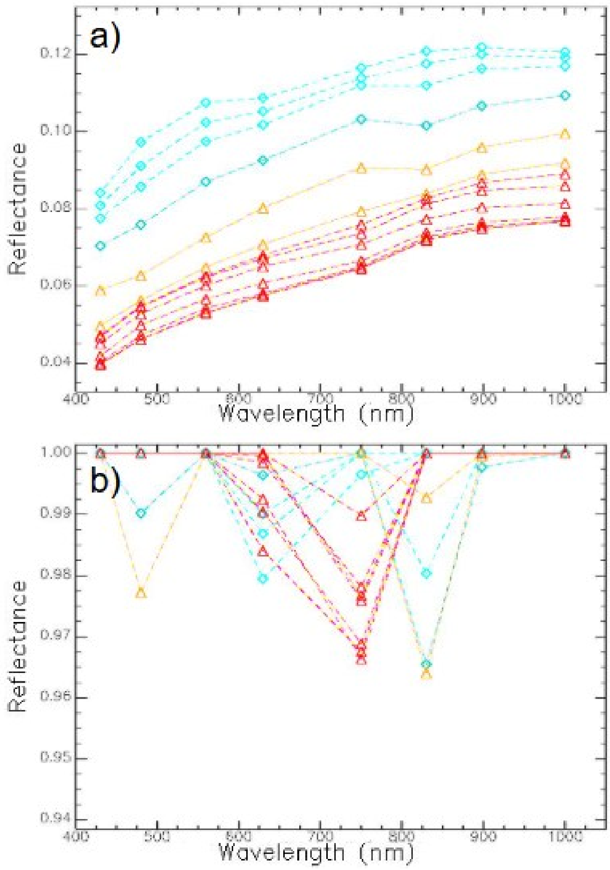

Fig. 48: Spectral analysis of the portion of area that goes (West to East) from hollow cluster, crater floor-smooth, crater wall to proximal ejecta (a) with continuum removed (b).

ROIs

Even for Hopper we investigate the spectral variability due to the different terrains external to the Hollows.
Fig.49 clearly shows how the relative lower resolution, which imply for similar distances a lower number of spectra attributable to Hollows alone, the spectral properties are dominated by spectral signature attributable to other material, generally darker and without peculiar spectral features. Conversely, ROIs acquired among the Hollows clusters identify spectral properties more reliable with the hollows, with the portion closer to the peak ring in the N area of the crater are dominated by spectral features at 830 nm (ROI1), whereas the ROI2 acquired on other portions of the hollow clusters are similar to the spectra shown for Warhol crater (see Fig. 50).

To better understand the Hollow clusters properties, we investigate them by considering a selection of pixels (Fig.51) instead a polygon and two different thinner polygons (Fig.52)

In fig.51 in particular the studied pixels were taken on the south-east portion of the cluster to avoid the presence of material closer to the central peak, closer to the border with the crater floor-smooth. This ROI shows the absorption at 630-750 nm and the inflection around 1000 nm, even if with values of reflectance generally lower than the ones in Warhol.
In Fig.52 the first ROI (red area) covers a portion of the hollow cluster near the crater wall in the South part, it shows spectra coherent with the one for the hollows described also in Warhol crater. Conversely the second ROI (green area) characterised the crater floor-smooth In this area despite a lower reflectance, the spectra are similar to the blue spectra shown in the Fig.45 and 46 attributed to some pixels of Hollows cluster closer to the central peak, dominated by the absorption at 830 nm and a possible absorption around 550-600 nm.
The ROIs attributable to the other terrains on the surrounding of the crater show featureless spectra, relatively darker with just slightly brighter spectra on the north-west proximal ejecta.

5) ROI of portions of area from hollow cluster to proximal ejecta:

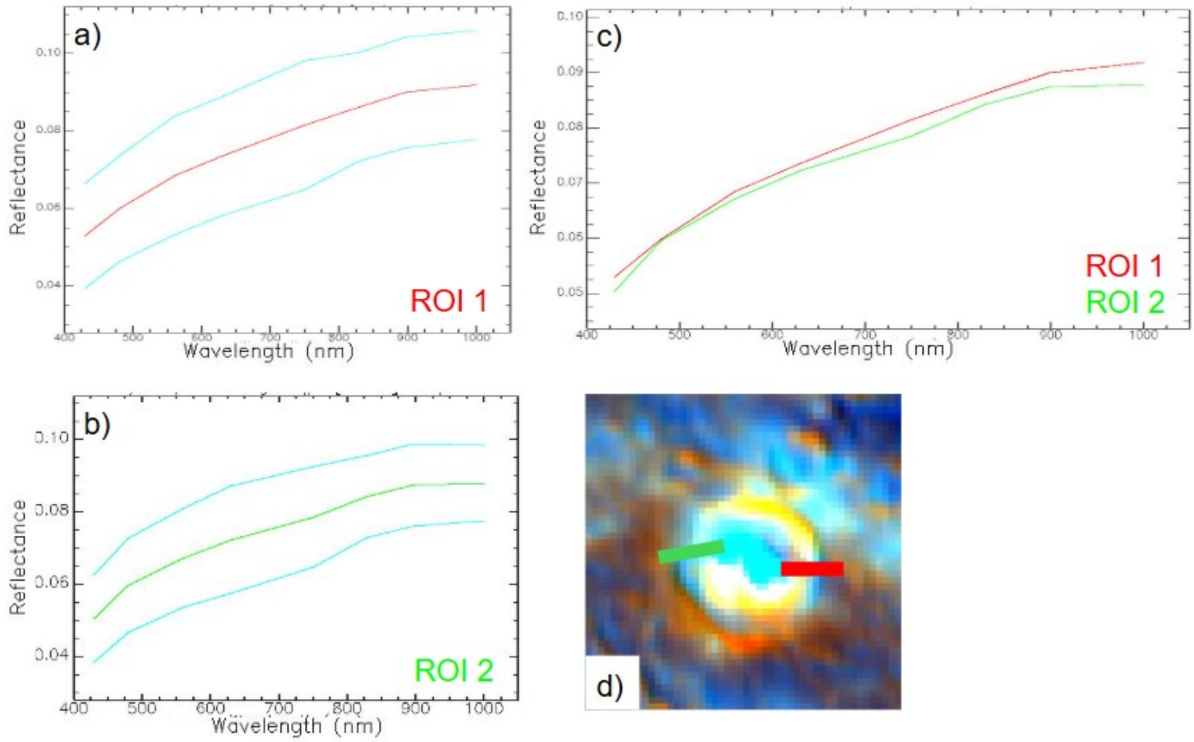

Fig. 49: ROI's mean for the site a (red), b (green), between standard deviation (cyan); ROIs comparison (c) and the (d) ROI's actual coverage of the selected hollow cluster. The red (a) one covers the spectral analysis of Fig. 35 and goes (West to East) from hollow cluster, crater floor-smooth, crater wall to proximal ejecta. The green polygon (b) covers hollow cluster, hummocky deposit, crater wall and proximal ejecta. We can observe that the two ROIs are very similar to each other.

6) ROI of hollow cluster 1 and 2:

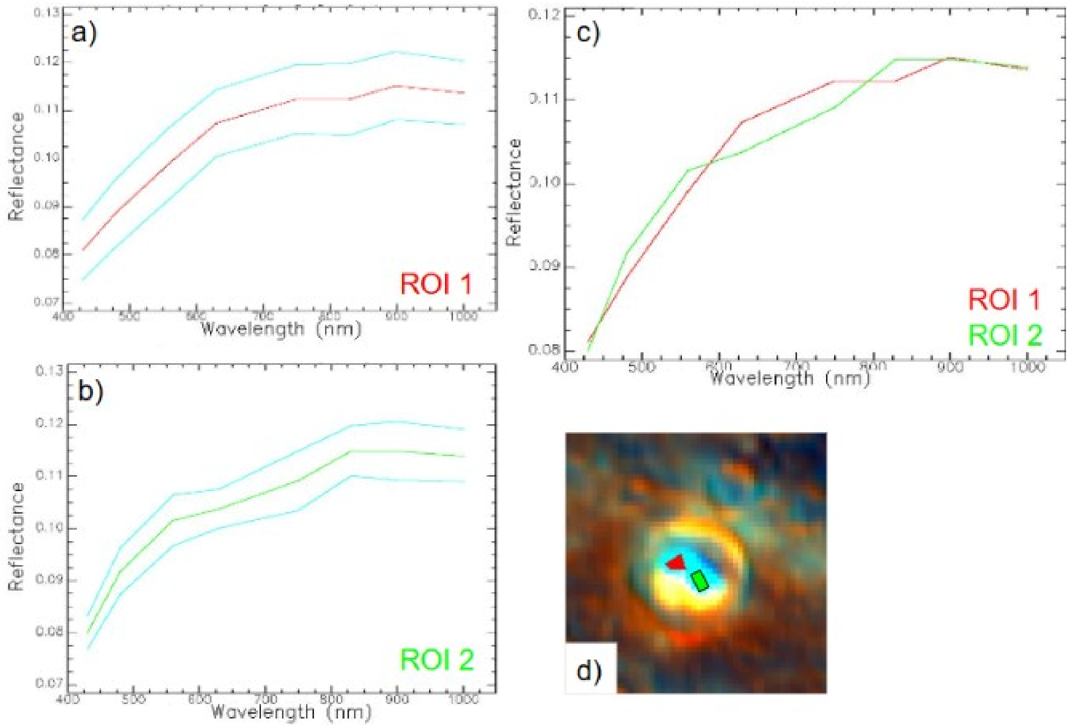

Fig. 50: ROI's mean for the site a (red), b (green), between standard deviation (cyan); ROIs comparison (c) and the (d) ROI's actual coverage of the selected hollow cluster. The hollows' ROIs are very different; we have an absorption from maxima around 550 nm and 800 nm for the b) and absorption at 830 nm in a).

5) ROI of pixels of hollows in a hollow cluster:

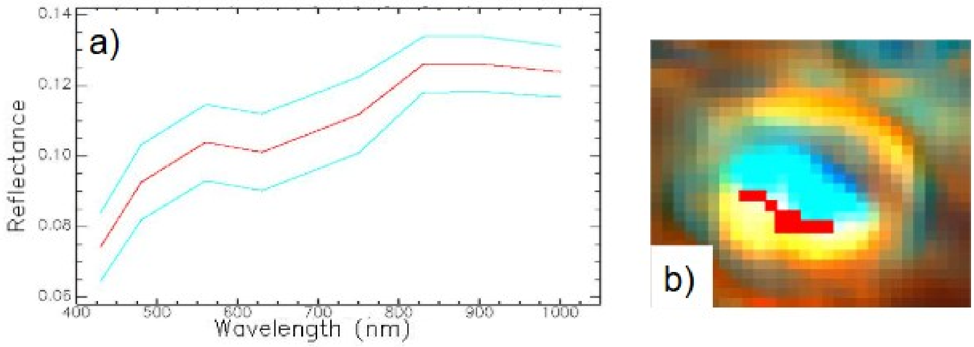

Fig. 51: ROI's mean for the selected pixels that host hollows of Fig. 47 (a) between standard deviation (cyan); ROI's actual coverage (b) of the selected hollow cluster.

5) ROI of hollow cluster near crater wall and crater floor-smooth:

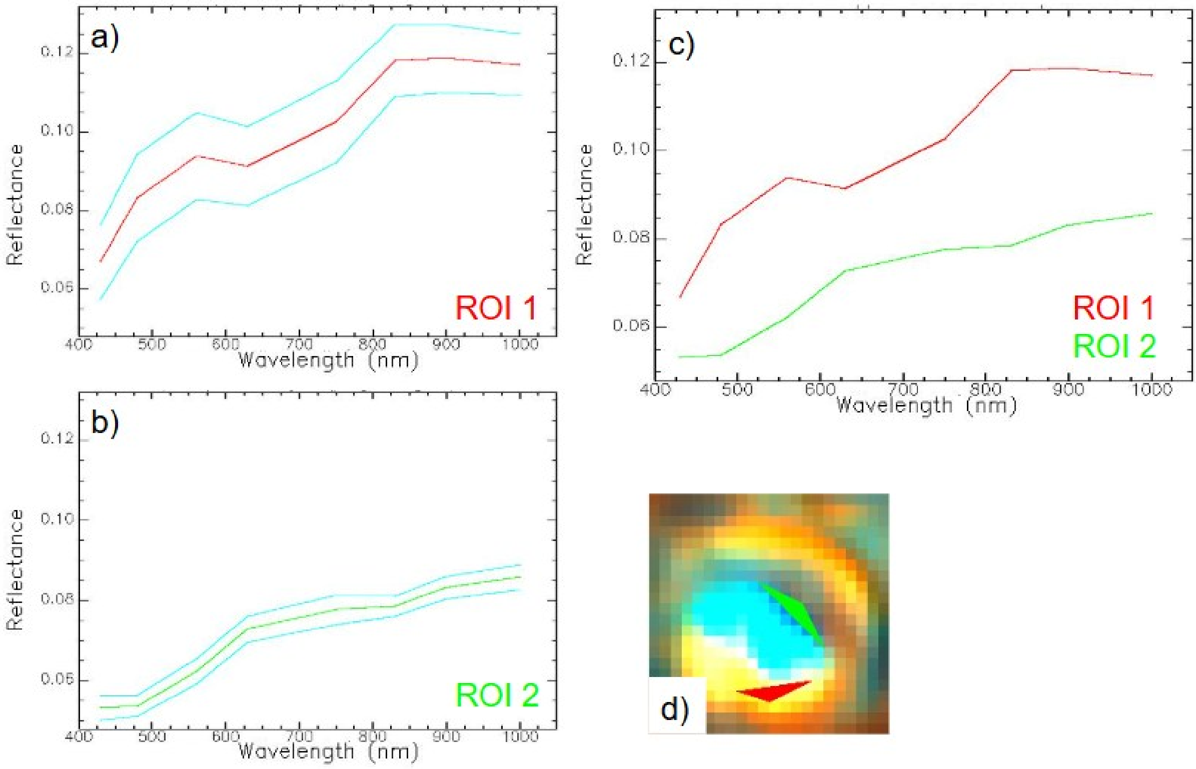

Fig.52: ROI's mean for the site a (red), b (green), between standard deviation (cyan); ROIs comparison (c) and the (d) ROI's actual coverage of the selected hollow cluster.

6) ROI of proximal ejecta:

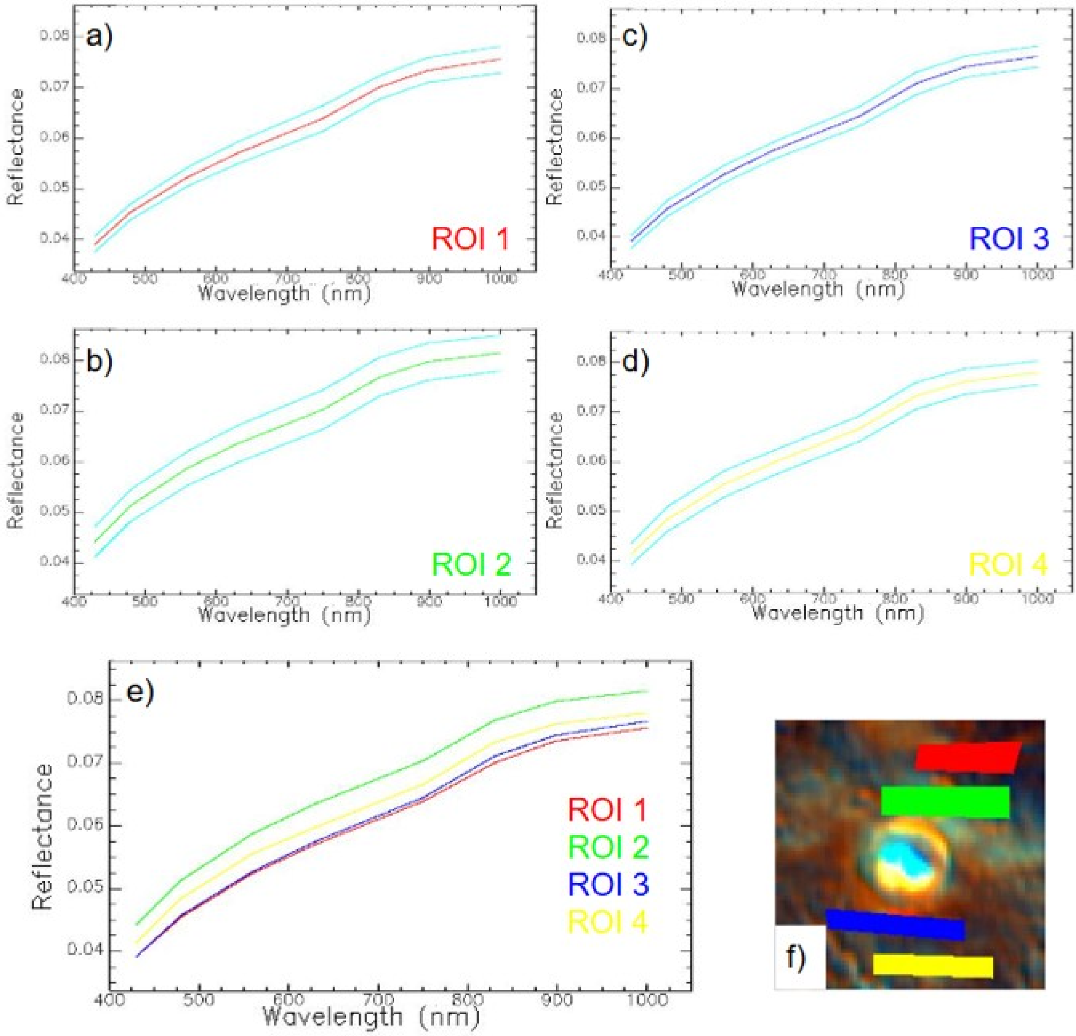

Fig. 53: ROI's mean for the site a (red), b (green), c (blue), d (yellow) between standard deviation (cyan); ROIs comparison (e) and the (f) ROI's actual coverage of the selected hollow cluster. The areas selected were considered to evaluate the reflectance of the surroundings of the Hopper crater.

3.2.3 Spectral analysis of Eminescu crater

Eminescu crater spectral analysis sites (Fig. 54) were also studied following the approach described in Warhol crater 3.2.1 section. Here we investigated (Fig. 54a) 3 hollow clusters through spectra analysis. Then we considered the area (4) where we collected some spectra for, from west to east, hollow cluster, hollow field, hummocky deposit, crater floor, crater wall and proximal ejecta. ROIs of all the above locations of hollow clusters were taken (Fig. 54b) and, moreover, other ROIs were selected to study the proximal ejecta, the transition from hollow cluster, hummocky deposit, crater wall and proximal ejecta. Finally, a comparison ROIs (Fig. 63) has been made to have all the terrain data (inner and outer) of the Eminescu crater.

These chosen areas were guided by a systematic comparison among the images in Figure 56).

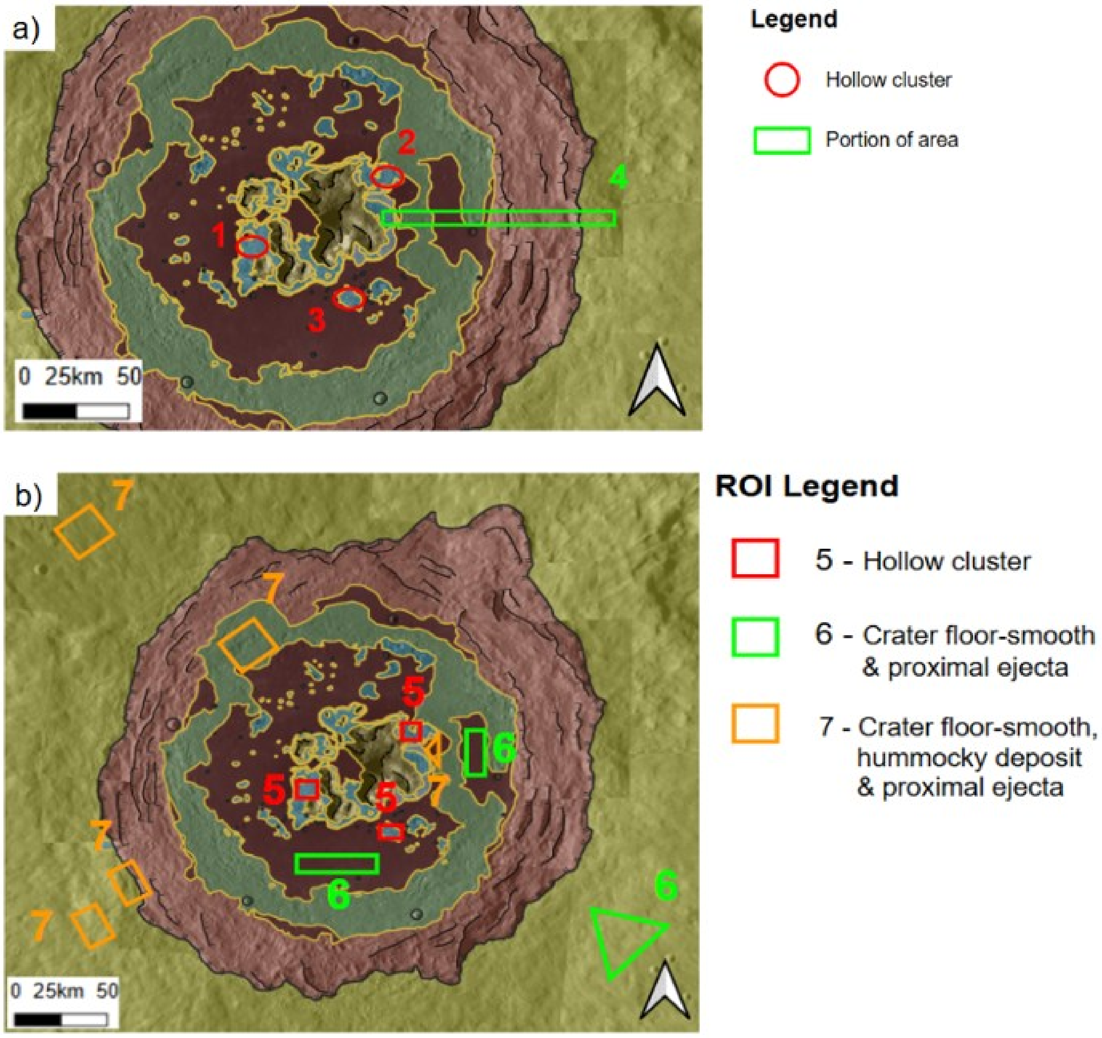

Fig. 54: a) Modified after figure 25, which implemented the site where spectral acquisition was detailed, done and discussed in the following figures.
b) Modified after figure 25, with only where the ROIs were taken for a more clean visualization.

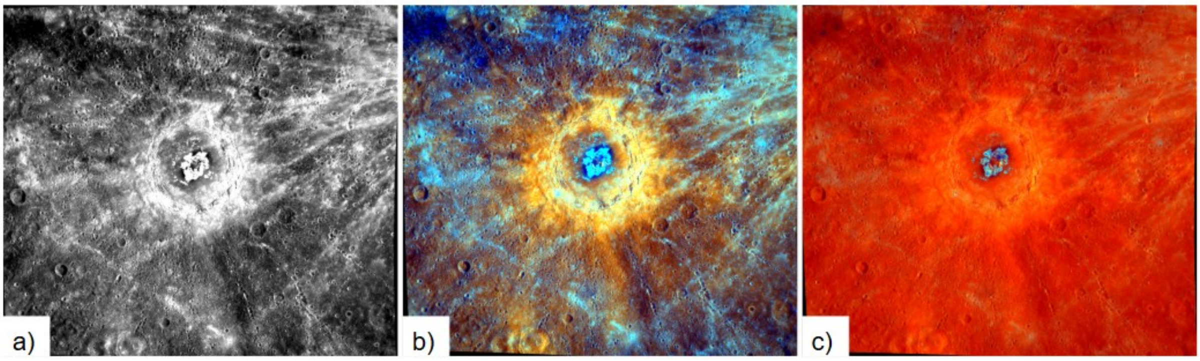

Fig. 55: Respectively, a) image in grey scale of the band 4 at 630 nm, b) enhanced color mosaic obtained on a high resolution cube based on PC2, PC1, 430/1000 with RGB stretch

values of 0.042, 0.063 for R; 0.192, 0.301 for G; 0.440, 0.560 for B; and c) the same RGB within a stretch on the Hollows dominated region on Warhol crater with RGB stretch values of 0.018, 0.058 for R; 0.199, 0.445 for G; 0.495, 0.822 for B. The color mosaic for Eminescu crater has been produced at 460 m/px.

Hollows:

For the hollows the differences in coloration on enhanced colour images were applied for collected spectra from a lighter cyan coloration to a darker cyan, which in our case is always indicating the west-to-east sampling and from the inner to outer of the crater.
The selected hollows cluster reported in Fig. 56, 57 and 58 show always the same spectra signature with a slight variegation in reflectance level and with a possible trend from the "inner" region (cyan spectra) vs the "external" regions closer to the central peak (dark-cyan to blue spectra). Nevertheless, all the investigated cases (Fig.56-58) show the presence of a relative bluer slope with respect other regions, due to a relative higher visible reflectance with respect to the near-infrared, a general high reflectance for Mercury, whereas a higher variability on absorption with respect to the previous cases are shown.
These higher variability of the spectral properties are evident in the single pixel transects shown in the following Fig. 56-58 as well as in the ROIs averages spectra of Fig. 60 where pixels of certain hollows were collected. The hollows reflectance ranges from 0.15 (Fig. 57) to 0.17 (Fig. 58), compatible with the high albedo of this fresh material, but not all of them show peculiar absorption on the same position seen for Warhol and Hopper crater.
In particular, few spectra of the inner side of the cluster 1 (Fig.56) show the 630-750 nm absorption whereas a 900nm weak absorption seems to be the persistent feature. The other spectra do not show a peculiar absorption which results in the automatic ENVI ® continuum removed in possible weak absorptions at 550 and 750 (with the second one not considered reliable, see Denevi et al. 2018). The blue spectra, which are closer to the hollow field region next to the central peak, show instead a deeper distinctive absorption at 830 nm coupled with the 550 nm. The collected spectra are more heterogeneous in part due to a higher difficulty to separate the region of the hollow cluster with respect to the hollow field. Nevertheless, could be indicative of a higher mineralogical heterogeneity of the terrains. In cluster 2 and 3 (Fig.57 and 58) the situation is even clear, in fact the spectral variability among the hollows cluster reveals also a large absorption incorporating also the 550 nm band. This large absorption with shoulders from 500 up to 830 nm is always coupled with an absorption at 900 nm. In general, the cyan spectra, closer to the inner portion of the investigated clusters have a minimum closer to the 630 nm (particularly evident for the cluster 3).
In Fig. 59, instead we explored the variability from part of a hollow cluster moving out-side the crater (see site 4 in Fig.41a). The spectra colours go to cyan to a darker cyan proceeding to East for hollows, whereas orange is used for the crater wall and becomes darker on the proximal ejecta. The hollows spectra have a higher reflectance with the wide absorption band with a minimum at 630 nm, coupled with a 900 nm; nevertheless, few spectra are highlighting a weak absorption around 830 nm coupled with the 550 nm. Proceeding to the outer of the crater, the hummocky deposit and crater floor-smooth start to differ from the hollow's spectra. The most significant absorptions are around 550 nm and 830 nm. This information indicates that probably some pixel mapped as a hollow cluster could instead be related to other material from the surrounding.

It emerged that the hollows of Eminescu crater could have different mineralogical evidence, indeed, the surrounding terrain of the crater has a higher reflectance value to the others craters and it's clearly visible from the enhanced mosaic map.

1) *Hollow cluster 1:*

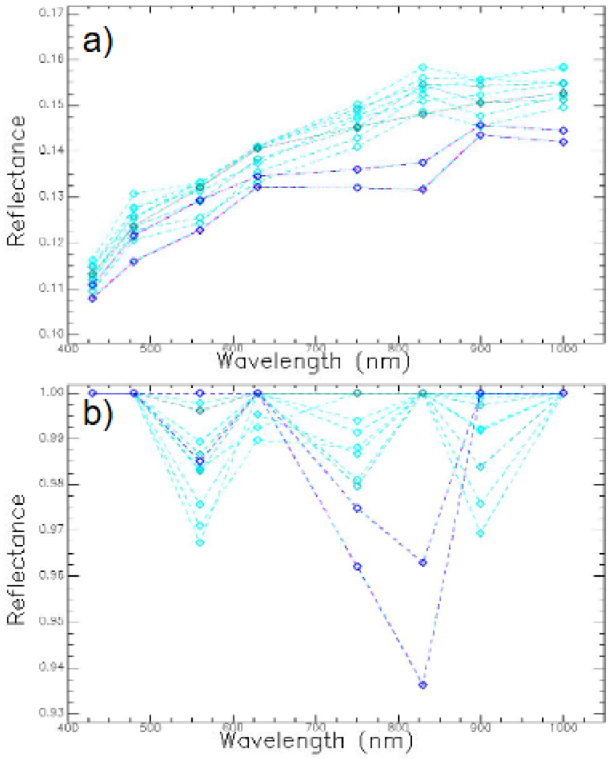

Fig. 56: Spectral analysis of the hollow cluster 1 (a) with continuum removed (b). The reflectance reaches its maximum value around 0.16 with a weak absorption at 630 nm wavelength and stronger absorption around 550 nm, 750 nm and 900 nm.

2) Hollow cluster 2:

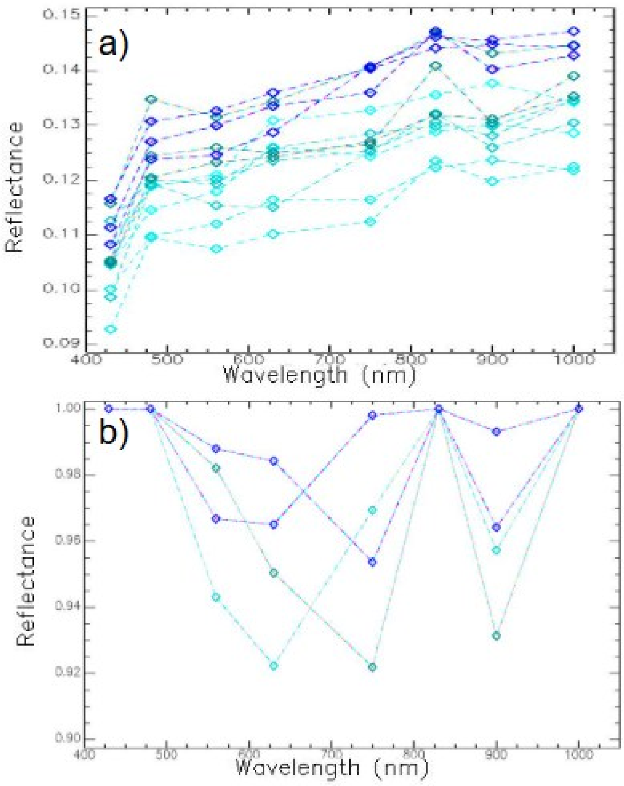

Fig. 57: Spectral analysis of the hollow cluster 2 (a) with continuum removed (b) of the most significative spectra.

3) hollow cluster 3:

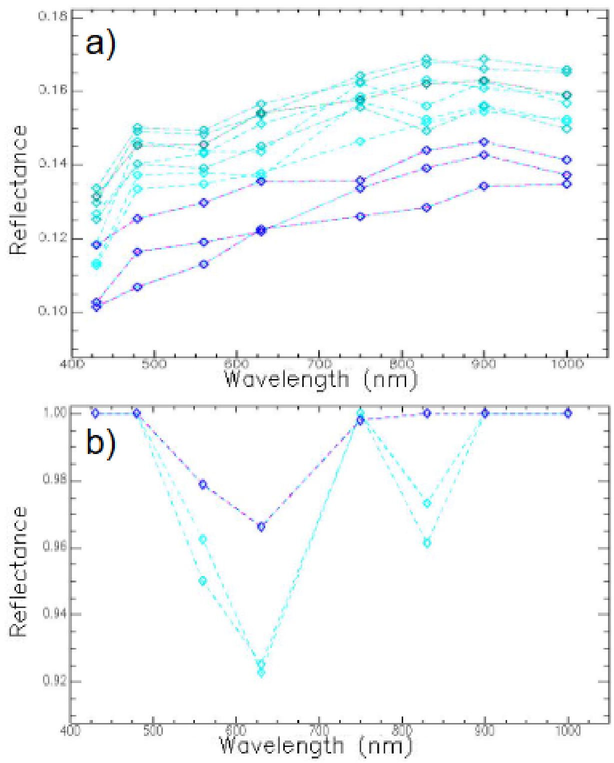

Fig. 58: Spectral analysis of the hollow cluster 2 (a) with continuum removed (b) of the most significative spectra. The reflectance value is globally higher than the others hollow clusters, reaching maximum value of almost 0.17.

4) *portion of area from hollow cluster to proximal ejecta:*

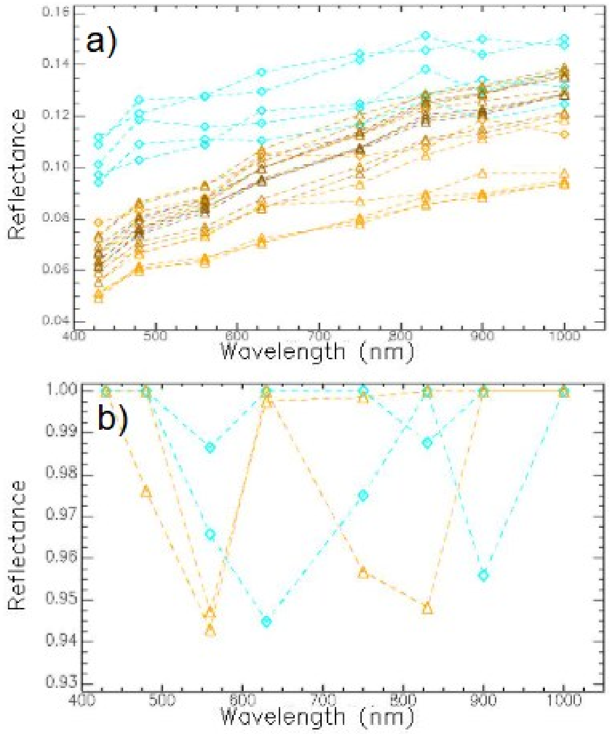

Fig. 59: Spectral analysis of the portion of area that goes (West to East) from hollow cluster, hollow field, hummocky deposit, crater floor-smooth, crater wall to proximal ejecta (a) with continuum removed (b) of the most significative spectra. Hollows are coloured with cyan and the orange, brighter to darker shades proceeding towards East, is used for hummocky deposit, crater floor-smooth, crater wall and proximal ejecta.

<u>ROIs:</u>

As well as for the other cases, we investigate the spectral variability due to the different terrains external to the Hollows.

In Fig. 60 we produced some ROI for different hollow clusters, the average spectra with respect to the one shown for Warhol and Hopper crater do not show the peculiar information described above for several of the pixel spectra as well as the standard deviation are broader. This suggests a higher pixel to pixel heterogeneity with respect to the other craters studied. Higher variability is even seen from a ROI to another in terms of reflectance and slopes with respect to the previous investigated cases.

In Fig. 61 and in Fig. 62 we investigated the differences between crater floor-smooth and the outer terrains; they in general show similar trend with lower reflectance and slightly redder shape than the hollows cluster, with the material inside the crater or crater wall slightly brighter (Fig. 63) than those seen outside with not peculiar evidence of specific absorptions

5) *ROI of hollow clusters:*

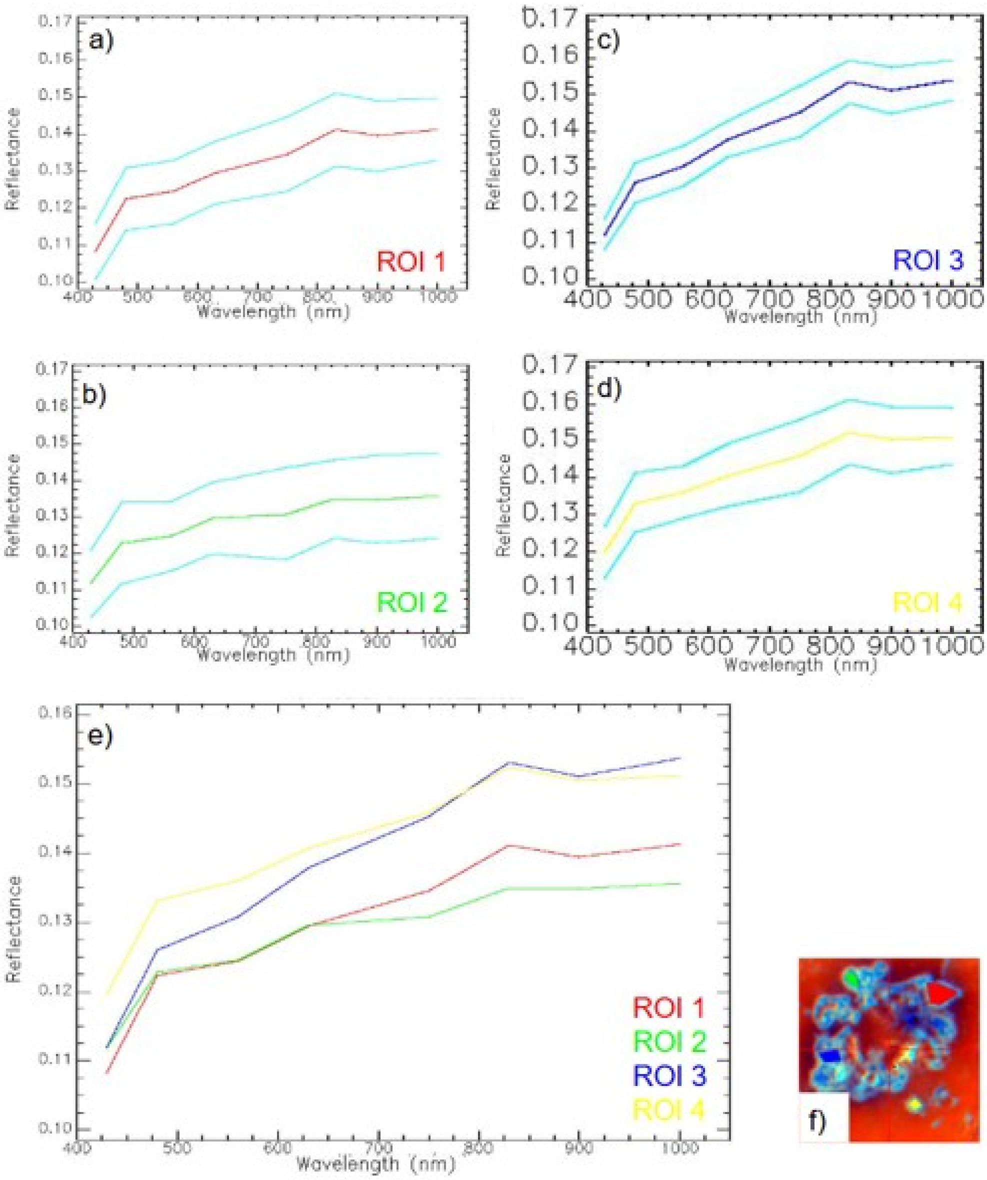

Fig. 60: ROI’s mean for the area a (red), b (green), c (blue), d (yellow), between standard deviation (cyan); ROIs comparison (e) and the (f) ROI’s actual coverage of the selected hollow clusters. All the hollow clusters areas are more heterogeneous between each other compared to the ones on the other craters studied. An important difference in reflectance values is clearly visible. The yellow area (d) and slightly the blue area (c), highlight a globally higher reflectance due to the distancing from the centre of the crater. The heterogeneity within the clusters made the single spectra collection impracticable for a representative sampling.

6) ROI of crater floor-smooth and proximal ejecta:

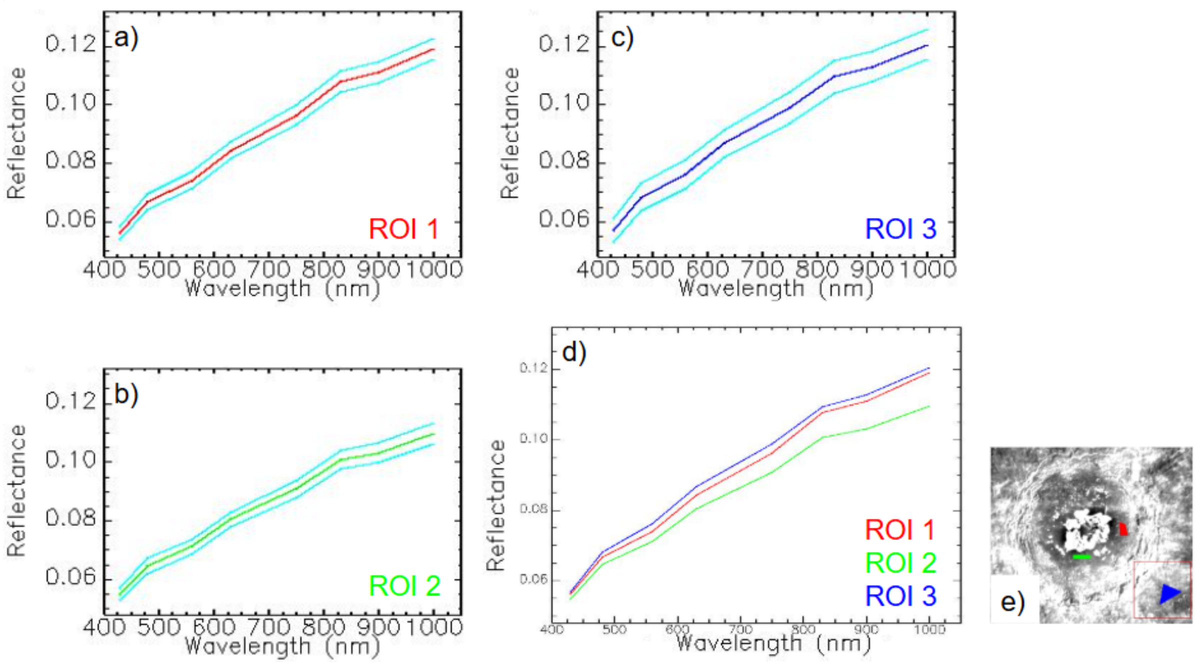

Fig. 61: ROI's mean for the area a (red), b (green), c (blue), between standard deviation (cyan); ROIs comparison (d) and the (e) ROI's actual coverage of the selected crater floor-smooth and proximal ejecta.

7) ROI of crater floor-smooth, hummocky deposit and proximal ejecta:

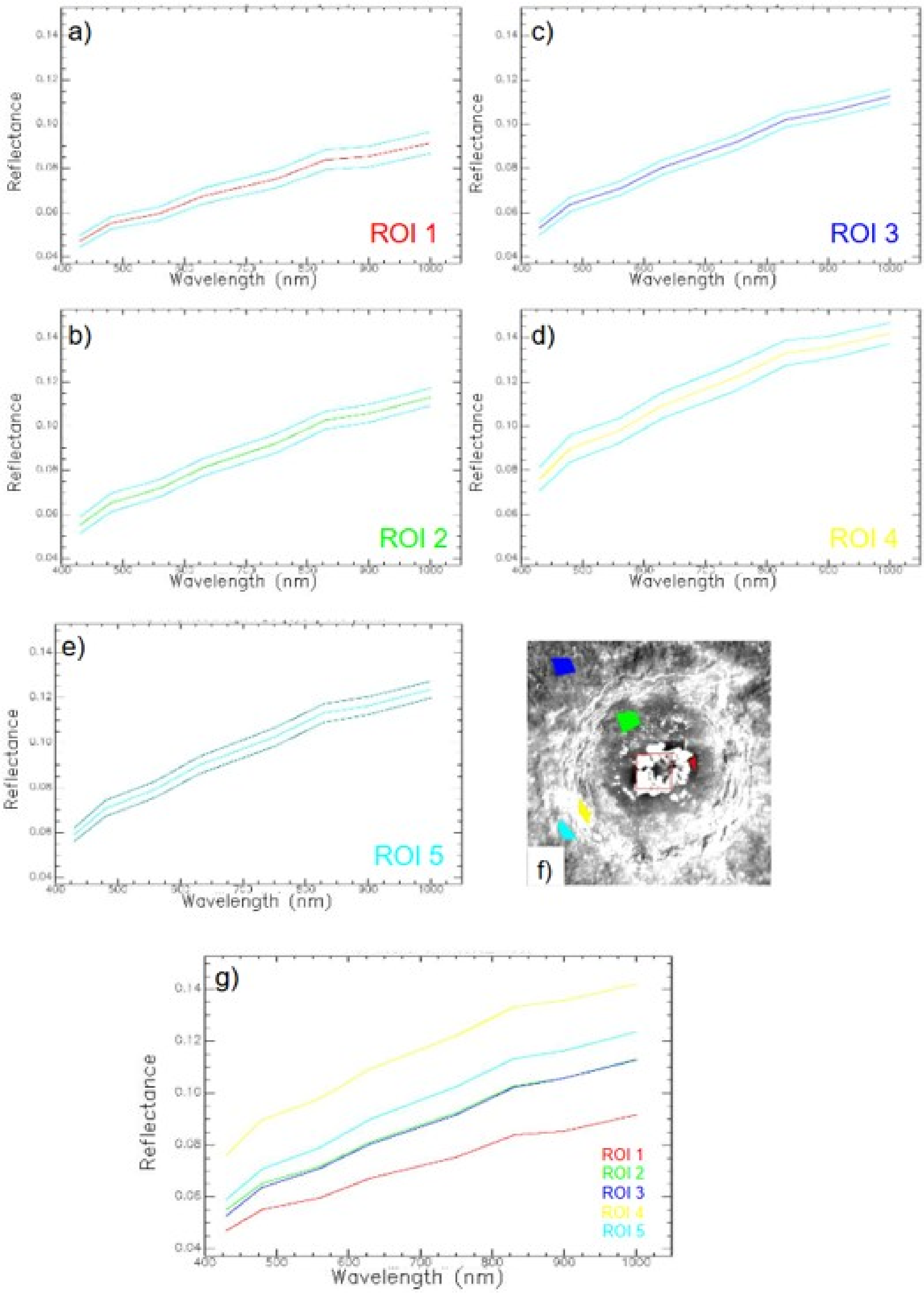

Fig. 62: ROI's mean for the area a (red), b (green), c (blue), d (yellow), e (cyan), between standard deviation (cyan); ROI's actual coverage of the crater (f) and ROIs comparison (g) between all the features.

8) Comparison of ROIs 7 and 6:

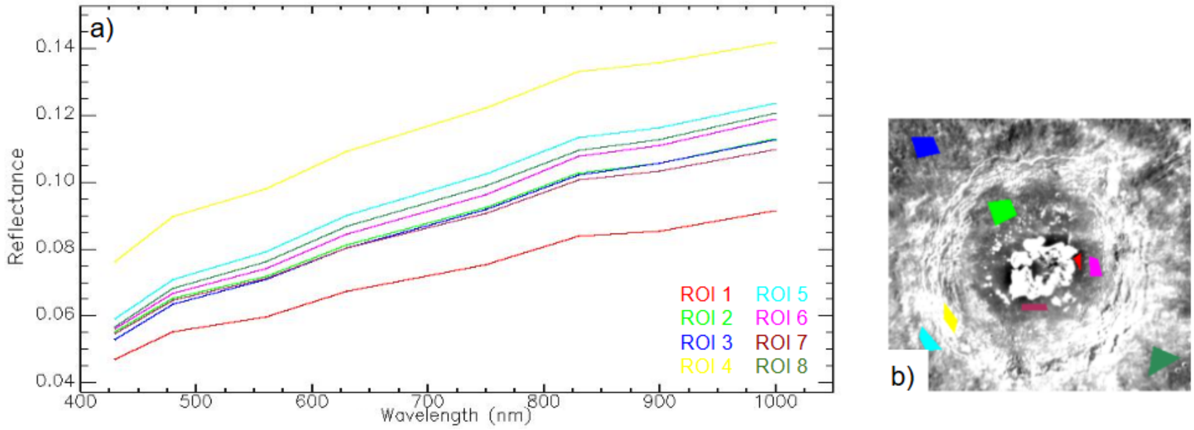

Fig. 63: Comparison of the already seen ROIs of the terrain features (fig. 61 and fig. 62).

3.2.4 Spectral analysis of Sander crater

Sander crater spectral analysis sites (Fig. 64) were studied following the approach described in Warhol crater 3.2.1 section. Here we investigated (Fig 64a) 2 regions of hollow clusters where a spectral analysis was performed with the continuum removed (Fig. 66, 67): a spectral analysis for the portion of area number 3 and 4 to investigate hollow cluster within the talus cone (Fig. 68), and the transition from hollow cluster to the crater wall (Fig. 69), with ROI of the latter (Fig. 64b), to observe the hollow cluster in comparison with the crater wall. Finally, ROI's analysis for the hollow clusters (5) (Fig. 70); for yellowish hollow cluster portion more visible in the stretched map (6) (Fig. 71) and for crater floor-smooth with proximal ejecta (7) (Fig. 72). Other than that, one more ROI were collected by picking only selected pixels with a clear spectral signature of hollow, as a detail of the hollow cluster's ROI (5). These chosen areas were guided by a systematic comparison among the images in Figure 65).

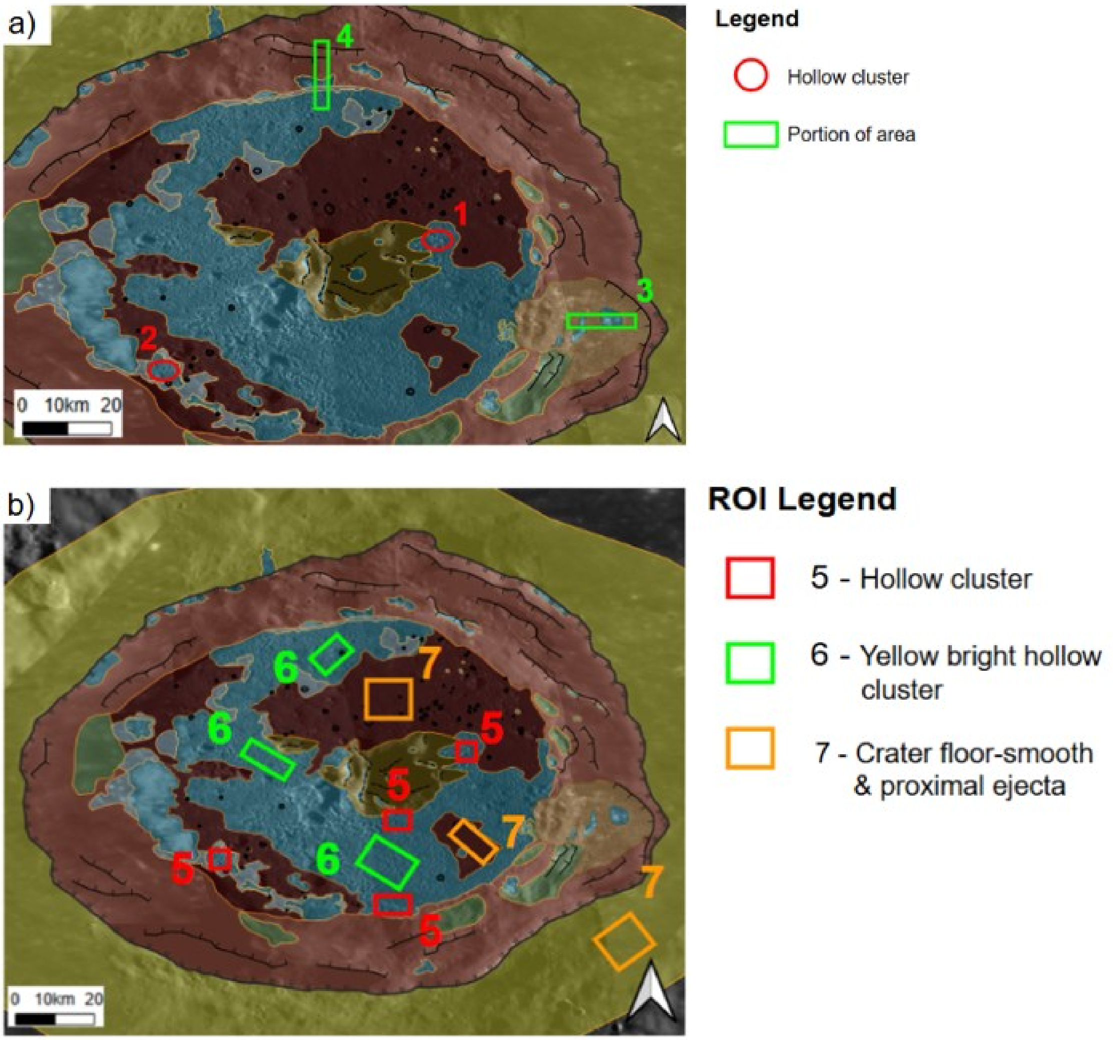

Fig. 64: a) Modified after figure 29, which implemented the site where spectral acquisition was detailed, done and discussed in the following figures.
b) Modified after figure 29 with only where the ROIs were taken for a more clean visualization.

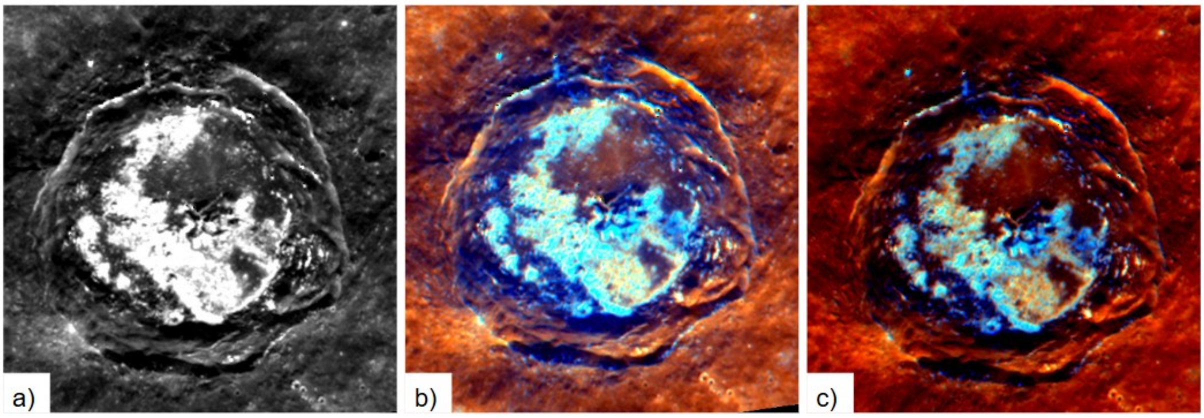

Fig. 65: Respectively, a) image in grey scale of the band 4 at 630 nm, b) enhanced color mosaic obtained on a high resolution cube based on PC2, PC1, 430/1000 with RGB stretch values of 0.029, 0.052 for R; 0.133, 0.309 for G; 0.433, 0.649 for B; and c) the same RGB within a stretch on the Hollows dominated region on Warhol crater with RGB stretch values of

0.030, 0.056 for R; 0.162, 0.374 for G; 0.493, 0.709 for B. The color mosaic for Sander crater has been produced at 133 m/px.

Hollows:

For the hollows the differences in coloration on enhanced colour images were applied for collected spectra from a lighter cyan coloration to a darker cyan, which in our case is always indicating the west-to-east sampling and from the inner to outer of the crater.
The selected hollows cluster in Fig. 66, 67, always show spectra signatures with a relative bluer slope, relative high reflectance, a putative absorption around wavelengths 630-750 nm and an inflation towards the longer wavelengths (900-1000 nm), among which sometimes the 900 nm is superimposed to the inflection (see Fig. 66b). The ROI shown for the cluster 1 highlight as for several pixels, despite a difference in reflectance the spectral properties are consistent with those seen already for Warhol crater and Hopper crater.
The hollows reflectance ranges from 0.13 (Fig. 66) to 0.14 (Fig. 67) at wavelengths of 900 nm. The spectral signature of Fig. 66 shows overall lower reflectance values than the other crater's hollows with less heterogeneity.

These spectral properties are evident in the transects shown in the following Fig. 68-69. In particular, Fig. 68 shows the variability from part of a hollows cluster within the talus cone on the crater wall moving towards the outer's crater (see site 3 in Fig. 64a). The spectra colours go to cyan to a darker cyan proceeding to East for hollows, whereas orange is used for the crater wall and becomes darker proceeding to east. The hollows spectra are brighter (Fig. 68a) and they have a wide absorption band incorporating not only the 630-750 nm wavelengths but even 580 and 830 nm (Fig. 68b). The spectra of the crater wall that surround the hollows are darker (Fig. 68a) in the talus cone shows an intense similar to the previous described from 500 nm up to 830 nm, with few pixels, the more external do not show peculiar absorption but just a low reflectance (a part the possible artifact at 750 nm, Fig. 68b).
The Fig. 69 analyse a portion of area that covers hollow cluster and crater wall and compared to the Fig. 68, it's clear the reflectance difference between the two areas, supporting the idea of the talus spectra "contamination". The hollows spectra have a much higher reflectance values with absorption band at 630 nm, 830 nm and 900 nm wavelength. The absorption band for the crater wall are visible at 550 nm, from 750 to 830 nm wavelength.

1) Hollow cluster 1:

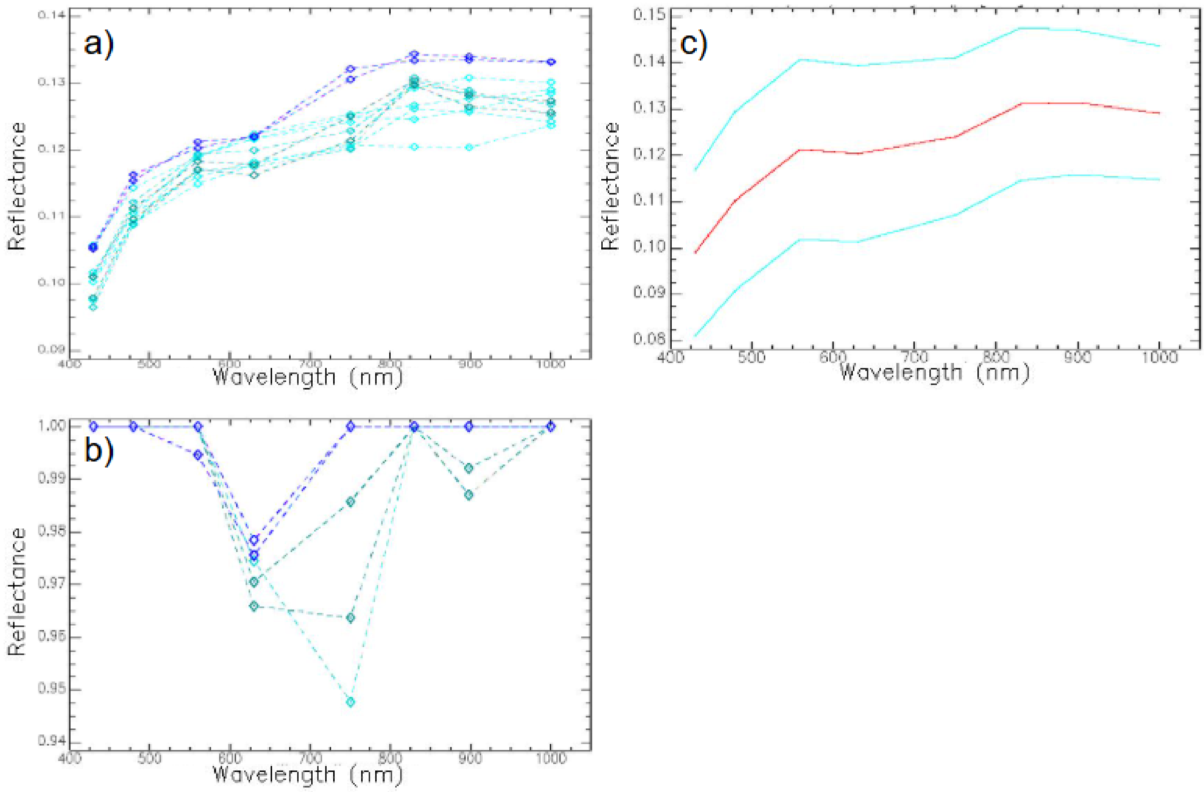

Fig. 66: Spectral analysis of the hollow cluster 1 (a) with continuum removed of the more indicative spectra(b). ROI of few selected pixels within hollow clusters that showed a recognizable hollow's spectral signature (c).

2) Hollow cluster 2:

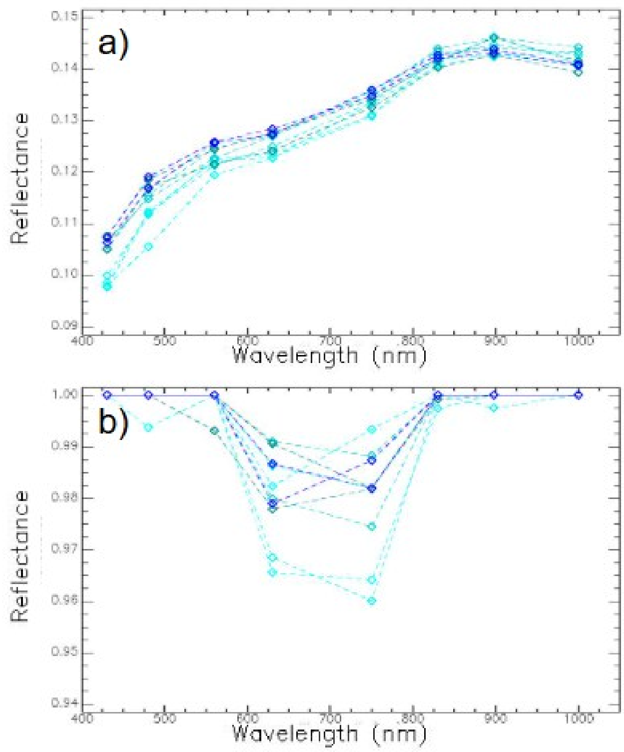

Fig. 67: Spectral analysis of the hollow cluster 1 (a) with continuum removed of the more indicative spectra(b).

3) Portion of area showing hollow cluster in the talus cone:

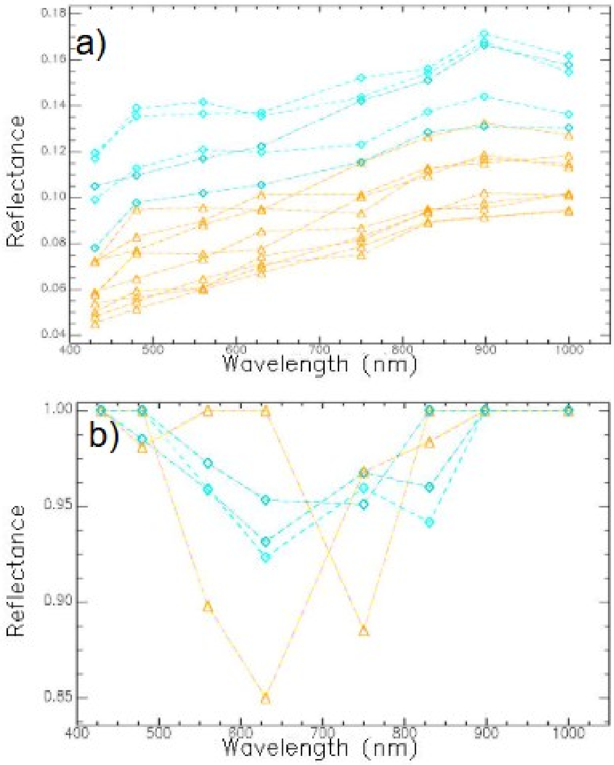

Fig. 68: Spectral analysis of the portion of area (West to East) in the talus cone on the crater wall, passing through hollow clusters (a) with a continuum removed of the more indicative spectra (b). Cyan shades were used for hollows and orange shades for talus cone material (brighter to darker according to the West-East sampling.

4) Portion of area from hollow cluster to crater wall:

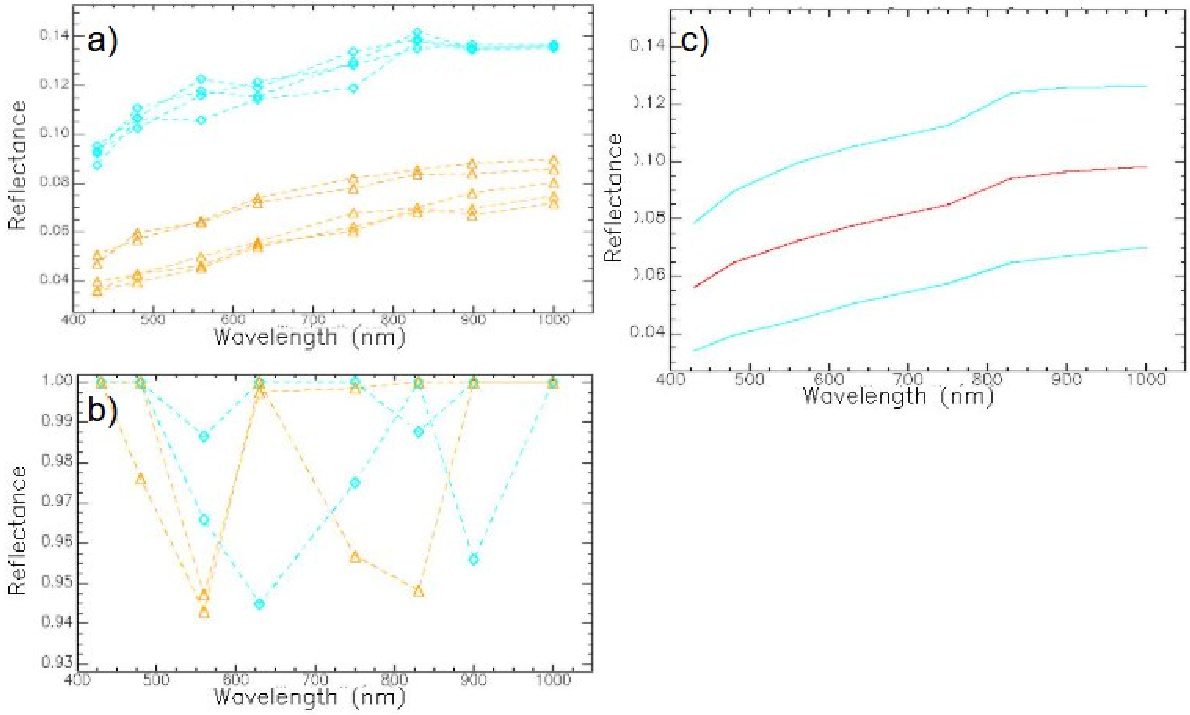

Fig. 69: Spectral analysis of the portion of area 4 that goes from hollow cluster (cyan) to crater wall (orange) (a) with a continuum removed of the more indicative spectra (b).

<u>ROIs:</u>

The ROI of Fig. 70 clearly shows that all the hollow cluster areas are more heterogeneous resembling the ones of Eminescu crater (Fig. 60) studied. An important difference in reflectance values is clearly visible. The green area (Fig. 70b) and the blue area (Fig. 70c), highlight a globally higher reflectance. The heterogeneity within the clusters made the single spectra collection impracticable for a representative sampling. All the spectra show a reflectance peak at 550 nm and 830 nm (Fig. 70e) and, for the ROI2 (green) there is a steeper inflection near 1000 nm.

In Fig. 71 we investigated 3 areas that show a bright yellow coloration in the stretched enhanced map within hollow clusters, and we observe that all the sites show a very similar trend with a little variation in reflectance.

As well as for the other cases, we investigate the spectral variability due to the different terrains external to the Hollows. In Fig. 72 areas of the crater floor-smooth and of the proximal ejecta were investigated. The material present in those terrains looks very similar in the enhanced color images (see Fig. 65b, c) suggesting similitude in compositions. This similitude is confirmed by the spectral comparison of the ROIs, in fact we noted that the crater floor-smooth (Fig. 72a and b) and proximal ejecta (Fig. 72c) areas exhibit a very similar trend, showing featureless, relative red slope, and even no inflection at 1000 nm. Looking at the reflectance compared to the one of Eminescu (Fig. 63), the low values of Sander crater could be explained by a less bright terrain as it is for Eminescu crater's terrains.

5) ROI of hollow clusters:

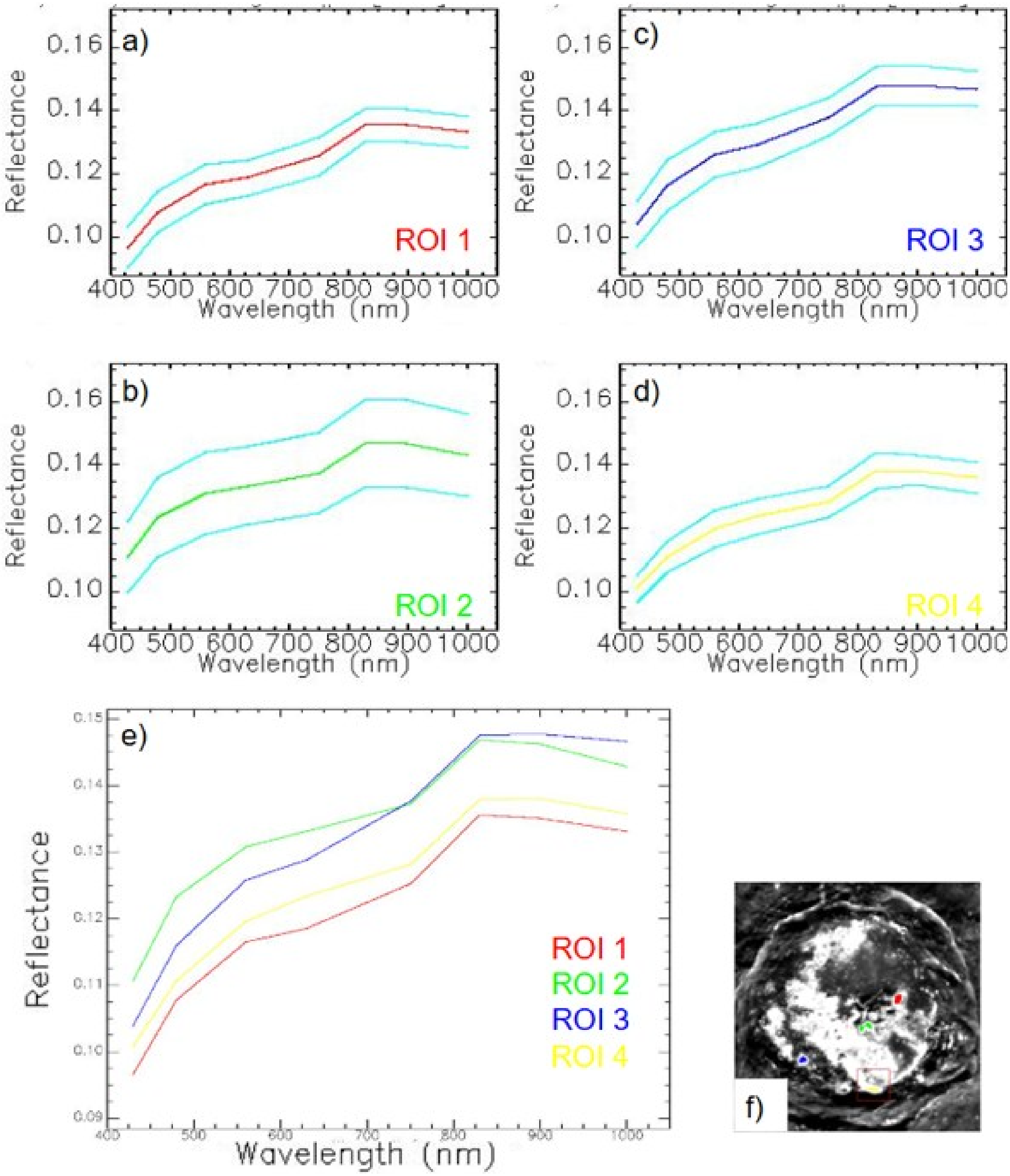

Fig. 70: ROI's mean for the site a (red), b (green), c (blue), d (yellow) between standard deviation (cyan); ROIs comparison (e) and the (f) ROI's actual coverage of the selected hollow cluster.

6) ROI of yellow areas in the hollow clusters:

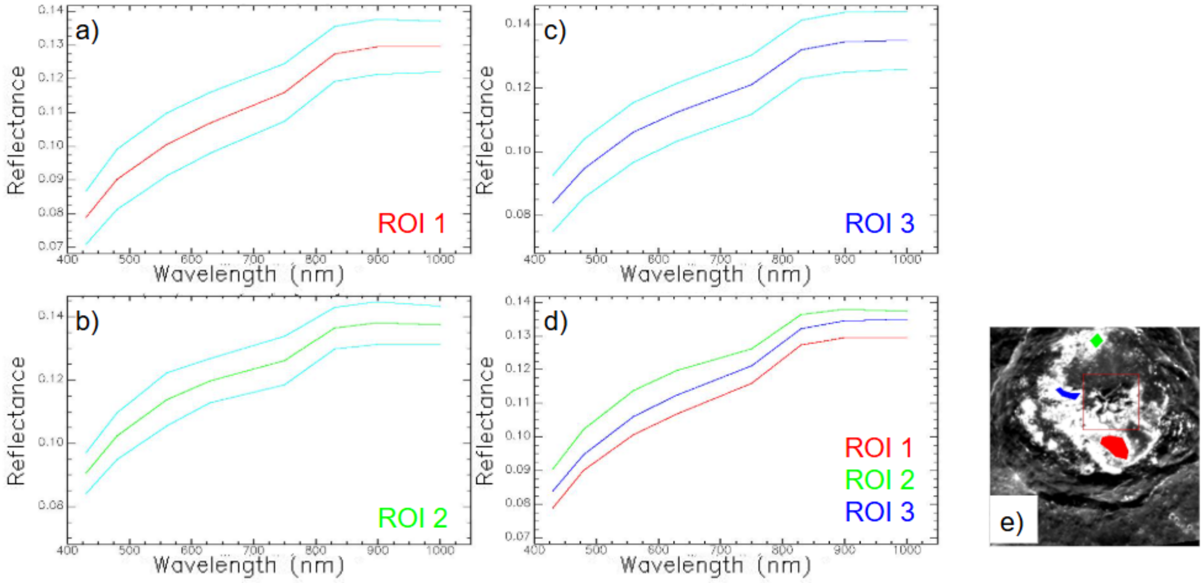

Fig. 71: ROI's mean for the site a (red), b (green), c (blue), between standard deviation (cyan); ROIs comparison (d) and the (e) ROI's actual coverage of the selected hollow cluster that shows a bright yellow coloration in the stretched enhanced map.

7) ROI of crater floor-smooth and proximal ejecta:

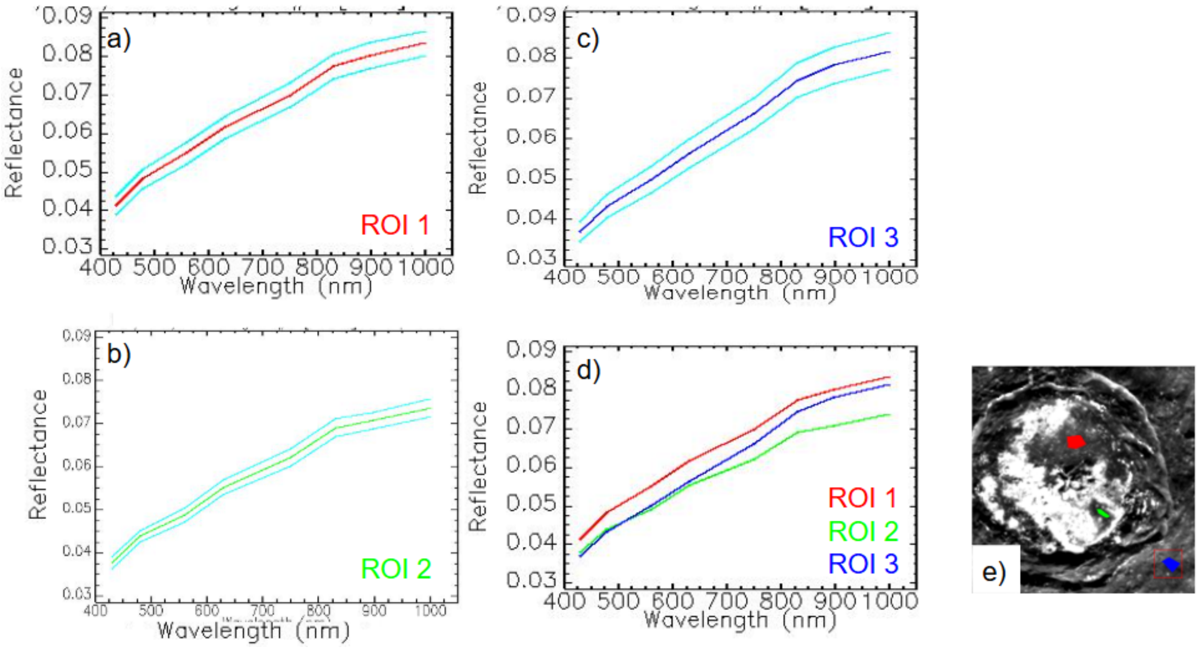

Fig. 72: ROI's mean for the site a (red), b (green), c (blue) between standard deviation (cyan); ROIs comparison (d) and the (e) ROI's actual coverage of the selected crater floor-smooth and proximal ejecta.

4. Discussion

In the literature, the hollows have been studied deeply within Dominici crater, in the Kuiper quadrangle (H-04), that hosts many of these features.
They are characterized by shallow, irregular, rimless depressions with high-reflectance interiors (Blewett et al., 2013) (Fig. 3-5). These features are interpreted to form through the loss of volatile-bearing materials and are among the youngest landforms on Mercury (Blewett et al., 2016; Xiao et al., 2013). Studies based on MESSENGER mission data has revealed important aspects of their composition and evolution.
Early work by Villas et al. (2016) identified, for the first time, distinct spectral absorption associated with hollows at Dominici crater. Notably, the different absorption features dependant on the location of the hollows within the crater; absorption band at 630 nm for the ones situated in the southern of the crater wall, and absorption band at 830 nm for the ones situated in the central part of the crater (see their fig. 2). Moreover, the spectral behaviour suggests the presence of low-density magnesium sulfide (MgS), probably inherited from the background substrate (Villas et al., 2016).
These observations were supported by later studies by Lucchetti et al. (2018), who used spectral clustering and high-resolution geomorphological mapping to investigate hollows in several craters, including Dominici. The results highlighted a broad absorption band between the maxima at 550 nm and 830 nm observed in all the analysed hollows; the spectral shape could not be fully explained by sulfides alone, instead, it likely involves a combination of sulfides (such as CaS, MgS) and pyroxenes containing transition elements like Cr, Ti and Ni. All these findings led to the conclusion that hollow material is a mixture of degassed remnants and original crustal (bedrock) material, suggesting a dual origin for their spectral signature (Lucchetti et al., 2018).
A more recent study by Emran and Stack (2025), using a machine learning approach, helped to differentiate hollows at different stages of development within Dominici. In particular, the authors found that active hollow on the crater rim is dominated by silicate materials (primarily augite and albite) with minor contributions from graphite and CaS; the hollow in the centre of the crater contains slightly higher amounts of sulfides (MgS and CaS) and graphite, but lower silicate content; the surrounding Low Reflectance Material (LRM) is supposed to be rich in graphite and sulfides. Emran and Stack (2025) conclude that hollow formation likely begins through thermal decomposition of MgS and CaS, possibly with graphite depletion and, as a secondary effect, the volatile loss progresses and slows leaving residual silicates as remnants, stabilizing the surface and preventing further growth (Emran and Stack, 2025).

Dominici shows the most peculiar spectral features as reported in Vilas et al (2016; see Fig. 73), and the meaning of those spectral features are discussed also in Lucchetti et al. (2018) and recently in Emran & Stacks (2025). The attribution of the peculiar absorption is still under debate, with a tentative to address them, and in particular the absorption around 630 nm, to peculiar “relatively volatile” minerals such as CaS or MgS (Helbert et al. 2013; Vilas et al. 2016). Further works try to explore even the spectral properties of other mineral phases such as Lucchetti et al. (2021) were also possible attribution to some chloride has been proposed. Conversely, mafic iron-free minerals but bearing other transitional elements could suggest the presence of similar absorption at 630-750 nm coupled with potential absorption (for iron at very low content) around 900-1000 nm (e.g. Lucchetti et al. 2018; Landi et al. 2025 and reference there in).

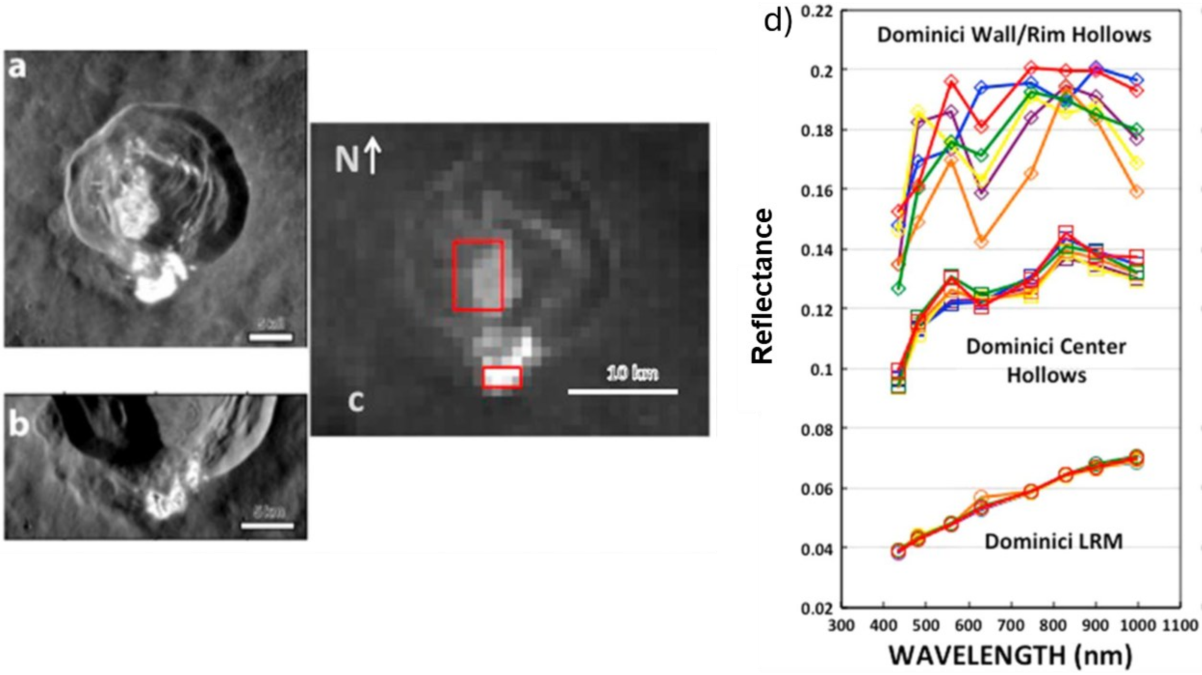

Fig. 73: Modified after Fig.1 and 2 in Vilas et al. (2016) showing the selected hollows fields (a-c) and the respective features properties, in d), in comparison to the surrounding terrains.

We investigated four different craters, where the morpho stratigraphic maps shows clearly similar characteristics, with the presence of areas within the typical define hollow fields with higher hollows concentrations, called here hollow clusters in similitude to the high-resolution maps produced in Lucchetti et al. (2018). The hollows cluster are mainly characterizing the crater floor, around the central peak and sometimes closer to the border among the floor and the wall. Another remarkable point is that all of this crater shows a smooth infilling that probably is correlated with the post impact activity, due to a “secondary volcanism” attributable to the energy of the impact.
Investigating the hollow clusters superimposed to the smooth-floor material, in this work we noted that Warhol crater shows the best hollows-like spectra (Fig. 34-37) as described so far from previous work (Vilas et al. 2016; Lucchetti et al. 2018; Emran and Stack, 2025) similar to the main characteristics of Dominici crater. Hopper crater shows similar spectral properties for part of the hollow clusters (Fig. 45-47), despite the lower spatial resolution, nevertheless it is possible to recognize, closer to the central peak a portion of the hollow clusters dominated by a weak spectra signature around 830 nm, no absorption at 650-700 nm, and a potential absorption towards 500nm (Fig. 45). This type of spectra was already shown, but not discussed, on the spectra of Dominici (see figure 73), whereas recently Galiano et al. (2024) shown for pixel closer to the hollows, on the edge of hollows and bright gullies within Praxiteles basin, the presence of the same spectral type. In their case they suggest a possible evolution of the Hollows field from material more mature (where a 630-700 nm absorption is found) or more pristine for the Hollows showing 830 nm.
In addition, Hopper crater shows the same spectral type (830 nm-like) in a ROI that should be attributed to the smooth-floor infilling material (Fig. 50), which indicates that or the low spatial

resolution due not permit to evidence morphologies attributable to hollows in these terrains, or this spectral type has to be attributed to material closer but outside the hollow fields/clusters. It is of interest to note that all of these two first cases as well as Dominici are coming from the same quadrangle (Kuiper, H-06). Despite the relatively high distances from the three craters (from Hopper to the west, there are 1015 km to Dominici and others 1298 km to reach Warhol to the east of the quadrangle) there could be a possible regional control from a composition point of view.
Instead, Eminescu and Sander, show a higher variability of the spectral properties among the hollow cluster. This can be due to the higher spatial resolution of the multispectral cube (460 mn/px and 133 m/px, respectively) that permit to highlight a higher heterogeneity in mineralogy.
In fact, the hollows cluster shows portion, relatively reduced, in particular in Eminescu (Fig. 56-58), where the spectral properties are closer to the terrains investigated in Dominici (from literature), Warhol and Hopper craters, showing relative high reflectance, the absorption at 630-750 nm, the inflation towards 1000 nm. Conversely, in some portions of hollow clusters are seen spectra with the presence of the 830 nm (Fig. 56, 58) as reported in Hopper crater in this work or in Praxiteles (Galiano et al. 2024). In addition, we also have seen spectra inside the hollow's clusters with a weak absorption at circa 900 nm which is in general coupled with the typical absorption around 630-750 nm (Fig. 56, 57, 66). In Eminescu this peculiar absorption is enlarged towards a shorter wavelength since the maxima is moved at 480 nm.
These two craters are coming from different regional contests. Eminescu crater is among the Eminescu (H-09), in general attributable to terrains that at global enhanced scale show more yellow colors, so less presence of LRM, and bluer terrains, as shown in the case from the Kuiper Quadrangle (H-06). Sander crater instead is in the Raditladi H-04 Quadrangle, and in particular within the regional control of the Caloris Basin, the biggest basin on Mercury, which is characterized by a different and peculiar geochemical composition from X-ray orbital data as referred to by Wider et al. (2016).

<u>Mineralogic Hypothesis:</u>

For the mineralogic composition, based on the work of Lucchetti et al. (2021) (see their figures 14, 15, 16 and 17), in which they analysed troilite samples and other possible terrestrial analogue rocks that resembles the spectra signature of the hollows with opportune heat alteration that should occur on the Mercury's surface. In addiction the analysis on samples of fluorapatite, fluorite and basaltic glass, led to the conclusion that hollows can be represented by a combination of Cl-compounds minerals, while the pyroclastic deposit by S-bearing minerals. For the absorption band at 900 nm wavelength, recent studies highlight that this could be caused by the absence of Fe, similarly to what we can see in the aubrites. This could mean that, this specific type of hollows, could have been formed from a terrain rich in mafic minerals (Landi et al., 2025).
More in depth, comparing our results with the ones of Lucchetti et al., (2021) (Fig. 74), we can observe some similarities like in Fig. 74a, the absorption band at 630 nm could be associated with sulphurs, supported even in Villas et al., (2016), without explanation for the inflection at 1000 nm, that can be explain in Fig. 74b by a possible mafic mineralogy with low Fe in Olivine, with the addiction of the absorption at 640-750 nm explained by the presence of others transition elements discussed in Lucchetti et al., (2018).

In Fig. 74c the absorption at 830 nm, possibly correlated with the one at 500 nm, could be attributed to a phases like oxides, pointing out how, in a first phase of hollow's evolution, there could be locally generated more oxidant conditions discussed in Galiano et al., 2024 and personal communication.

In Fig. 74d, the absorption at 900 nm can be explained by a higher concentration of low-Ca pyroxene, almost iron-free, that resembles the work of Landi et al., (2025) for Rantilla, but can't explain the absorption at 630-750 nm, even though the transition elements are near the detection limit and could be in higher percentage on Mercury; or even that this absorption could be the results of mixing of more phases, like for examples, mafic minerals that explain the region from 900 to 1000 nm wavelength.

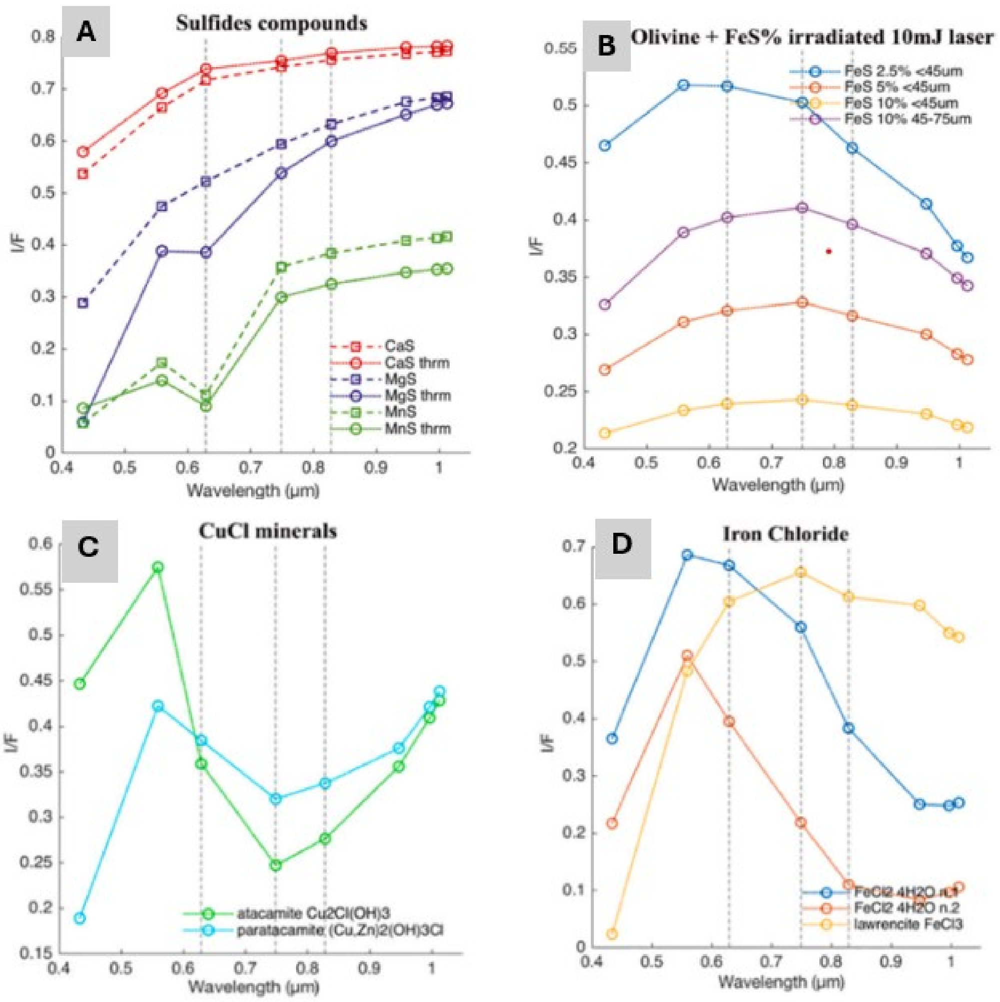

Fig. 74: Modified after figures 14 and 15 of Lucchetti et al., (2021).

Hollow cluster vs hollow field:

Within the units associated with the presence of hollows we can clearly see that in Warhol crater the main spectral features attributable to the hollows are present in the clusters whereas they show fewer peculiar spectra moving within the surrounding hollows field. A direct comparison of that can be seen in Fig.75: Warhol hollows differ from cluster to field (Fig. 75) especially for a distinctive absorption band at 630 nm and inflection at 1000 nm (a); where is not the case for the hollow field (b) and they show a lower reflectance value. This seems to indicate that the material dominating the hollow inside is different from the halo external to the hollow itself.

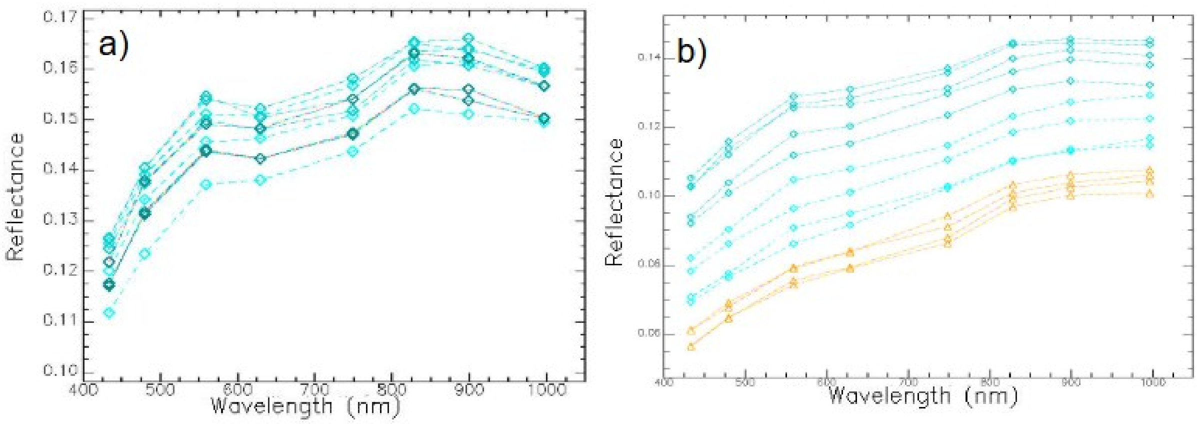

Fig. 75: Modified by Fig. 37 and Fig. 42. Comparison between hollow cluster and hollow field in Warhol crater.

Hopper hollows differ from cluster to field (Fig. 76), as for Warhol, for a distinctive absorption band at 630-750 nm and inflection at 1000 nm (a) seen in the clusters, whereas the field spectra (the darker cyan spectra) are almost featureless, darker and red in all the spectral range.

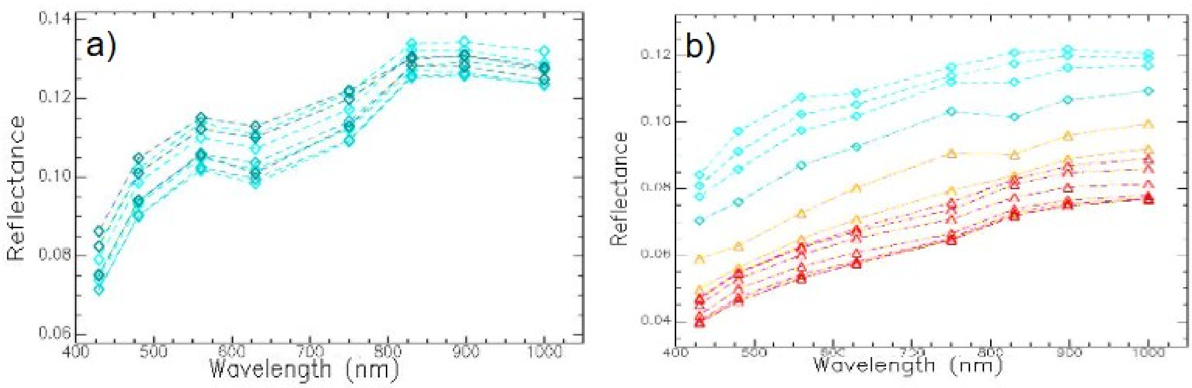

Fig. 76: Modified by Fig. 47 and Fig. 48. Comparison between hollow cluster and hollow field in Hopper crater.

Eminescu hollows are the most peculiar, showing a larger spectral variability than those observed in the other investigated cases, nevertheless even here we can see a difference from cluster to field (Fig. 77). In fig. 77a we can clearly see as some clusters are showing a more visible absorption at 830 nm whereas other are constrained by a minimum at 900 nm. In fig.77b instead other hollow clusters are characterized by a large absorption from 500 nm up to 830 nm with a second feature at 900 nm. In fig. 77c instead we can appreciate as the spectra outside the clusters are characterized by darker and featureless spectra.

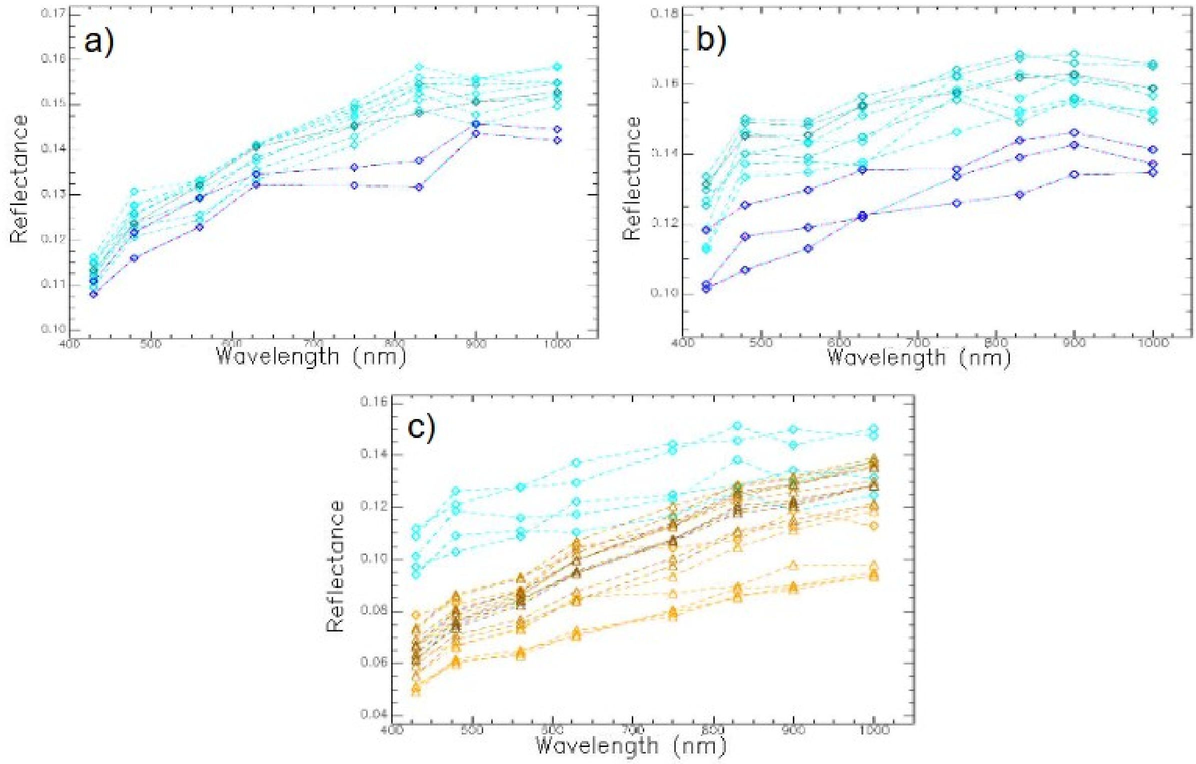

Fig. 77: Modified by Fig. 56 and Fig. 59. Comparison between hollow cluster and hollow field in Eminescu crater.

Sander hollows differ from cluster to field (Fig. 78) for a distinctive absorption band at 630-750 nm and inflection at 1000 nm present in the cluster (a and b, in this second the cyan spectra), with some cases showing a putative absorption centred at wavelength longer than 1000 nm and in other at 900nm. Hollow field (yellow spectra in b)) has a lower reflectance value compared to the hollow cluster. The high spectral discrepancy here with respect to previous cases suggests that the hollow field unit is probably less extended and it is probably influenced by “contamination” with crater floor material (see Fig. 59).

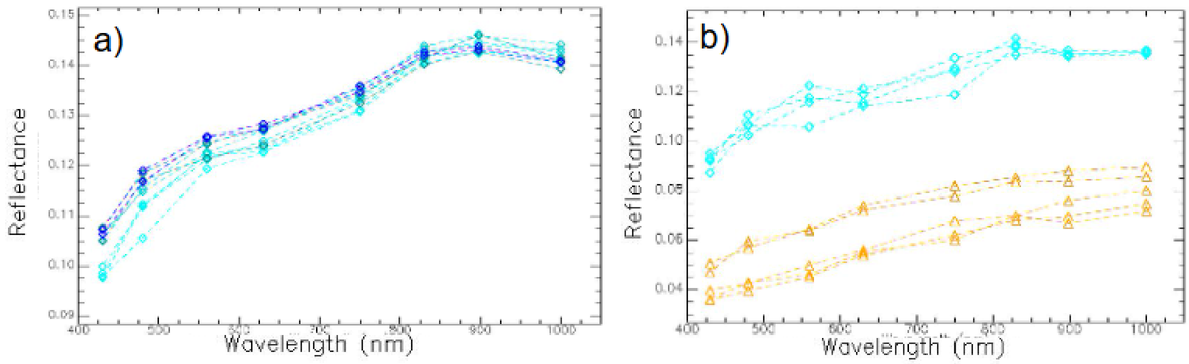

Fig. 78: Modified by Fig. 67 and Fig. 69. Comparison between hollow cluster and hollow field in Sander crater.

Craters terrain comparison:

The analysis on the crater terrains of all the sites shown in Fig. 79, makes clear that Eminescu has a more brighter ground, compared to the other craters with a more heterogeneous reflectance, and in general brighter with respect the other three cases (c); the Warhol crater has an almost homogeneous terrain except for the ROI2 that seems darker at higher wavelength, very similar to the Sander's terrains (d); Hopper terrains (b) are very homogeneous with a low range in reflectance variability.
By comparison, the sites of Warhol, Hopper, that have very similar terrains spectra, show a very similar spectra for hollow clusters too; the highly brighter terrain of Eminescu exhibits a more heterogeneous hollow clusters spectrum. Sander's, instead, although have spectra of the terrains similar to Warhol and Hopper, shows a higher heterogeneity within the hollow clusters' spectra like Eminescu's.

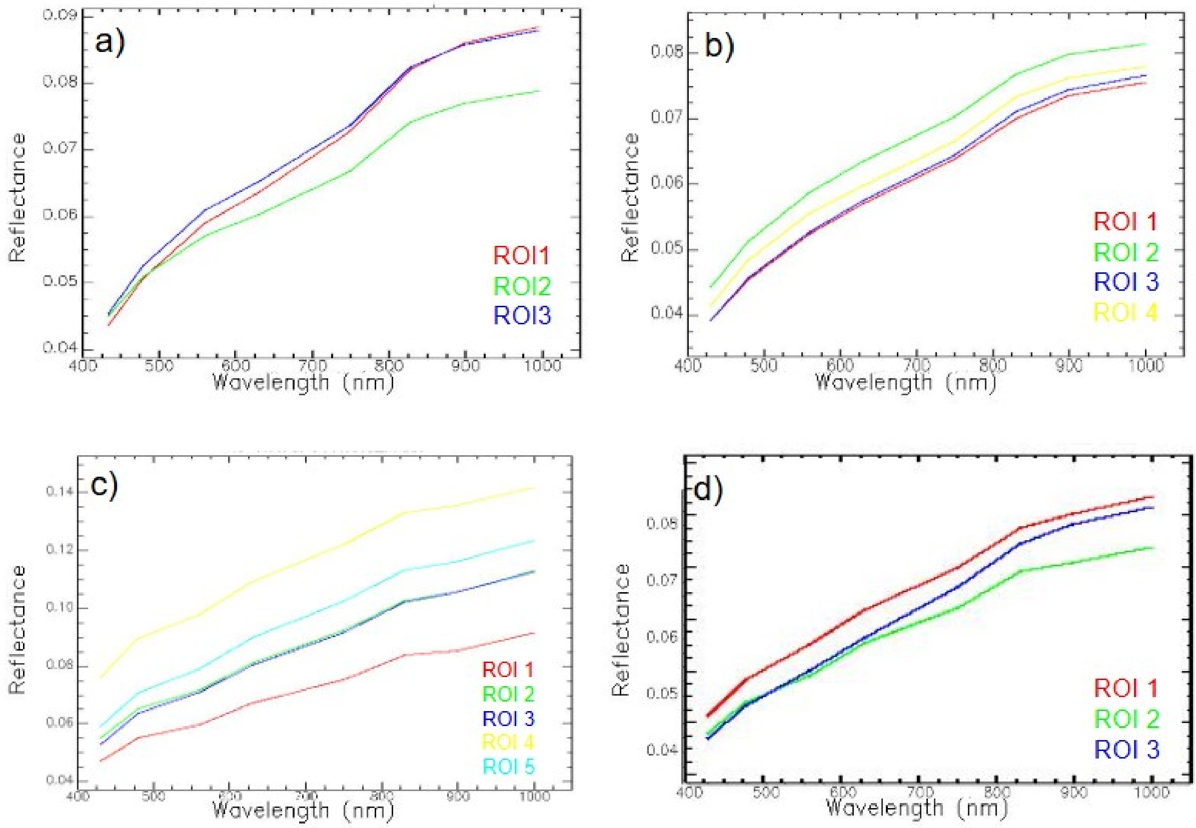

Fig. 79: Modified after Fig. 42, Fig. 51, Fig. 62, Fig. 72. Comparison between ROIs terrains of the Warhol (a), Hopper (b), Eminescu (c) and Sander (d) crater.

<u>Implication for Hollows formation and evolution:</u>

The results of this work could have implications on the formation and evolution of hollows compared to the one proposed by Blewett et al., (2013).

In our study we highlight that the region with a denser distribution of hollows (denominated as clusters) clearly shows peculiar spectral properties even with respect to the surrounding hollow fields (lower number of hollows and mainly characterized by the halo, bright cyan in global enhanced images). but with some differences.

Warhol and Hopper mainly have spectral properties closer to those highlighted in Dominici, they are thousands of km distance but still in the same regional control, in regions where terrains are often characterized by relative LRM. In Hopper part of the cluster as well part of the floor shows spectra with instead the typical properties an absorption at 830 nm coupled with a possible absorption at 500 nm, as already seen in Galiano et al. (2024).

Sander crater again shows very similar spectral properties of the previous two craters, but the inflation at longer wavelength since to indicate a weak absorption at 900 nm, similar to what have been seen in Landi et al. (2025) for a portion of Rantila with very low iron content in orthopyroxene ($En_{98.6}$).

Eminescu is the most peculiar, the hollow cluster shows a high variability, almost pixel by pixel, showing spectra with the presence of the 830 nm absorption as well as other spectra where the diagnostic absorption is larger than the previous cases and coupled with a 900 nm weak band.

This results since to suggest the main mineral phases attributed to the mercury surfaces like low and high- Ca pyroxene, and olivine could have an impact on the absorption at longer wavelength with a shift from 900 nm up to longer wavelength. The absorption at lower wavelength since more difficult to attribute to specific phase and both mafic minerals with the presence of few amounts of Ti, Cr, Ni could concur with possible alteration phases attributable to degassing processes and mainly to CaS and MgS as already suggested in the literature (Vilas et al. 2016; Luchetti et al. 2018). The case of Hopper in particular shows a possible presence of more oxidized material that was suggested as a possible precursor of Hollows formation by Galiano et al. (2014).
If we take into account, these results on the hypothesis of Hollows formation done by Blewett et al. (2013):

Hollows association with tectonic and impact-related features suggests that structural weaknesses may act as channels for volatile migration or as loci for mechanical breakdown of unstable mineral phases (Blewett et al., 2013) (Fig. 3). In this scenario all the craters studied here, with mainly hollows formed on the crater floor, could be possible suggesting that the material seen in the hollows cluster could be mainly characterized by the pertinent mafic mineralogy of the units behind the cap rock with possible interaction in the time with the volatile reach layer. The differences in spectral signature in particular for Eminescu with respect to the others could indicate a clear different composition of the original lava's rock.
It's not possible to exclude also the hypothesis of hollow formation by contact metamorphism (Fig. 4, in the introduction) because in every studied crater, it can be observed that they have some isolated (and sometimes even small cluster) hollows on central peak, and for some of them, Warhol in particular, on the contact between walls and crater floor. Moreover, for Hopper and probably for Eminescu, the hollows showing the spectra with the absorptions at 830 and 500 nm are closer to the central peak, suggesting, as done by Galiano at al. (2024), that this could be a relatively more active stage, with respect the hollows showing the absorption around 630 nm and an inflation towards longer wavelengths in the infrared.
The hollow formation by solar heating or space weathering (Fig. 5) could be the responsible for the hollows formation from a morphological point of view, even if in our cases, despite very small isolated recognized hollows on peak and on wall, all the clusters are within the crater floor which make this process less reliable In fact since both cluster and field of hollows are present and insist on the same floor unit we should expect more similar spectral signature between them, if they should reflect the alteration done by heating and weathering from the environment, whereas they are different.

5. Conclusions

In this work we focused on the investigation of four important craters with a wide distribution of hollows in particular in the crater floor. Those craters are placed in different areas of Mercury, with two of them relatively closer (2000 km circa from Hopper to Warhol) around the equators, whereas Eminescu and Sander are northern and further west.

The studied crater showed a spectral variance between hollows making them depend on the terrain in which they are situated and so it's not possible to regroup hollows to a referred and unique spectral signature as suggested before. Especially, Warhol and Hopper show spectra very similar to each other and to the Dominici crater well discussed in literature. Dominici, Warhol and Hopper belong to the same quadrangle (H-06), and a similar regional contest with association to the LRM. Eminescu and Sander exhibit different absorption bands that, in this work, it's attributed to a different terrain, since they show different spectral signature and color variation, and since they belong to different regional contests (belonging to quadrangles H-09 and H-04 respectively).
Nevertheless, we identify how the spectral signature in each location can be attributed to the hollows that are present only where hollows show a high density, here indicated, from a geomorphological point of view, as hollow clusters. This suggests that not all the material present in terrains belonging to the more generic hollow fields concur to identification of the hollows, differentiating the material within them and the relative surrounding halo.
The attribution of the spectral properties to specific mineralogy is not straight forward but we could suggest that some of the identify features, like the behaviour around 900-1000 nm can suggest the presence of mafic mineralogy with very low iron, which can be either low-Ca pyroxene or high-Ca pyroxene/olivine. Often this feature is associated to a putative absorption around 630-750 nm or even larger with a left shoulder at lower wavelengths (in Eminescu in particular) which could be attributed to mafic minerals with a relative abundance of other transitional elements and some sulphides, like CaS and MgS, as already suggested by literature. In Hopper and also in Eminescu was identified also the presence of a putative absorption at 830 nm, often coupled with an absorption at 500 nm which could indicate locally more oxidizing condition during degassing effects the formed the hollows, since the closest identification are some iron oxides.
The results from this work suggest that even if the three mechanisms of formation already proposed are all valid, at least for cases where the hollows cluster are formed in a smoothed re-filled floor the hypothesis of tectonic and impact-related and formation by contact metamorphism are favoured since from this phenomena we could expect, as seems from our results, that the hollows peculiar features should be present inside the hollows and not in the halo, and that the spectral signature could be influenced by both the original rock forming mineralogy and the alteration of the same by the volatile elements responsible of the hollow formation.

Further studies on other craters in different quadrangles and located more in other portions of the respective craters could contribute to support the interpretation of hollows' peculiar composition and genesis. Moreover, the better resolution for both morphology and spectroscopy awaited from the Bepi-Colombo ESA-JAXA mission from the beginning of 2027 will permit to definitively answer to this open question about the mineralogy of hollows and the interaction with the not waiting high volatile content of Mercury.

6. References

1. Anderson, J. D., Colombo, G., Esposito, P. B., Lau, P. B., & Trager, G. B. (1987). The mass, gravity field and ephemeris of Mercury. Icarus, 71(2), 337–349.
2. Anderson, J. D., Jurgens, R. F., Lau, E. L., Slade, M. A., & Schubert, G. (1996). Shape and orientation of Mercury from radar ranging data. Icarus, 124(2), 690–697.
3. Asphaug, E., & Reufer, A. (2014). Mercury and other iron-rich planetary bodies as relics of inefficient accretion. Nature Geoscience, 7(8), 564–568.
4. Barraud, O., Besse, S., Lucchetti, A., Zambon, F., Rothery, D. A., & Cremonese, G. (2020). Near-ultraviolet to near-infrared spectral properties of hollows on Mercury: Implications for their formation process. *Journal of Geophysical Research: Planets, 125*(10), e2020JE006471. https://doi.org/10.1029/2020JE006471.
5. Benkhoff, J., van Casteren, J., Hayakawa, H., Fujimoto, M., Laakso, H., Novara, M., ... & Ziethe, R. (2010). BepiColombo—Comprehensive exploration of Mercury: Mission overview and science goals. Planetary and Space Science, 58(1–2), 2–20.
6. Benz, W., Slattery, W. L., & Cameron, A. G. W. (1988). Collisional stripping of Mercury's mantle. Icarus, 74(3), 516–528.
7. Bickel, V. T., Deutsch, A. N., & Blewett, D. T. (2025). Hollows on Mercury: Creation and analysis of a global reference catalog with deep learning. Journal of Geophysical Research: Machine Learning and Computation, 2, e2024JH000431. https://doi.org/10.1029/2024JH000431.
8. Blewett, D. T., Denevi, B. W., Robinson, M. S., Klima, R. L., Gillis-Davis, J. J., Domingue, D. L., ... & Solomon, S. C. (2013). Mercury's hollows: Constraints on formation and composition from analysis of geological setting and spectral reflectance. Journal of Geophysical Research: Planets, 118(5), 1013–1032.
9. Blewett, D. T., Klima, R. L., Denevi, B. W., Ernst, C. M., Helbert, J., Izenberg, N. R., ... & Solomon, S. C. (2016). Analysis of MESSENGER high-resolution images of Mercury's hollows and implications for hollow formation. Journal of Geophysical Research: Planets, 121(10), 1798–1813. https://doi.org/10.1002/2016JE005070.
10. Blewett, D. T., Robinson, M. S., Denevi, B. W., Domingue, D. L., Gillis-Davis, J. J., Gaskell, R. W., ... & Solomon, S. C. (2011). Hollows on Mercury: MESSENGER evidence for geologically recent volatile-related activity. Science, 333(6051), 1856–1859.
11. Burbine, T. H., McCoy, T. J., Nittler, L. R., et al. (2002). Spectra of extremely reduced assemblages: Implications for Mercury. Meteoritics & Planetary Science, 37(8), 1233–1244.
12. Byrne, P. K., Klimczak, C., Şengör, A. M. C., Solomon, S. C., Watters, T. R., & Hauck, S. A. (2014). Tectonic landforms on Mercury: Evidence for global contraction. Nature Geoscience, 7(4), 301–307.
13. Cameron, A. G. W. (1985). The partial volatilization of Mercury. Icarus, 64(2), 285–294.
14. Cameron, A. G. W., Fegley, B. Jr., Benz, W., & Slattery, W. L. (1988). The strange density of Mercury: Theoretical considerations. In F. Vilas, C. R. Chapman, & M. S. Matthews (Eds.), Mercury (pp. 692–708). University of Arizona Press.

15. De Toffoli, B., Lucchetti, A., Galluzzi, V., et al. (2024). Hollows on Mercury: A comprehensive analysis of spatial patterns and their relationship to craters and structures. Earth and Space Science, 11(5), e2024EA003854.
16. Denevi, B. W., Chabot, N. L., Murchie, S. L., Becker, K. J., Blewett, D. T., Domingue, D. L., ... & Solomon, S. C. (2018). Calibration, projection, and final image products of MESSENGER's Mercury Dual Imaging System. *Space Science Reviews, 214*, 2. https://doi.org/10.1007/s11214-017-0440-y.
17. Denevi, B. W., Ernst, C. M., Robinson, M. S., et al. (2018). Global and regional variations in Mercury's color from MESSENGER observations. Journal of Geophysical Research: Planets, 123(5), 1232–1247.
18. Denevi, B. W., Solomon, S. C., Watters, T. R., et al. (2009). The evolution of Mercury's crust: A global perspective from MESSENGER. Science, 324(5927), 613–618.
19. Deutsch, A. N., Bickel, V. T., & Blewett, D. T. (2025). Hollows on Mercury: Global classification of degradation states and insight into hollow evolution. Journal of Geophysical Research: Planets, 130, e2024JE008747. https://doi.org/10.1029/2024JE008747.
20. Drake, M. J., & Righter, K. (2002). Determining the composition of the Earth. Nature, 416(6876), 39–44.
21. Dzurisin, D. (1978). The tectonic and volcanic history of Mercury. Journal of Geophysical Research, 83(B10), 4883–4906.
22. Emran, A., & Stack, K. M. (2025). Understanding compositional evolution of hollows at Dominici crater, Mercury. Icarus, 435, 116576.
23. Fegley, B. Jr., & Cameron, A. G. W. (1987). A vaporization model for iron/silicate fractionation in the Mercury protoplanet. Earth and Planetary Science Letters, 82(1–2), 207–222.
24. Galiano, A., Lucchetti, A., Besse, S., Rothery, D. A., Zambon, F., Galluzzi, V., ... & Cremonese, G. (2024). Quantitative spectral mapping of hollows and surroundings at Hopper crater on Mercury. *European Planetary Science Congress (EPSC) 2024*, Abstract EPSC2024-220. https://doi.org/10.5194/epsc2024-220.
25. Giacomini, L., Galluzzi, V., Massironi, M., Ferranti, L., & Palumbo, P. (2022). Geology of the Kuiper quadrangle (H06), Mercury. Journal of Maps, 18(1), 10–25.
26. Gladman, B., Burns, J. A., Duncan, M., Lee, P., & Levison, H. F. (1996). The exchange of impact ejecta between terrestrial planets. Science, 271(5254), 1387–1392.
27. Goettel, K. A. (1988). Mercury's density and composition: Constraints from thermal evolution models. In F. Vilas, C. R. Chapman, & M. S. Matthews (Eds.), Mercury (pp. 613–621). University of Arizona Press.
28. Grossman, J. N., Rubin, A. E., & MacPherson, G. J. (1988). Antarctic meteorites and the origin of Mercury. In F. Vilas, C. R. Chapman, & M. S. Matthews (Eds.), Mercury (pp. 619–653). University of Arizona Press.
29. Head, J. W., Chapman, C. R., Strom, R. G., et al. (2008). Volcanism on Mercury: Evidence from the first MESSENGER flyby. Science, 321(5885), 69–72.
30. Kerber, L., Head, J. W., & Wilson, L. (2009). Explosive volcanic eruptions on Mercury: Eruption conditions, magma volatile content, and implications for interior volatile abundances. Earth and Planetary Science Letters, 285(3–4), 263–271.
31. Kerber, L., Head, J. W., & Wilson, L. (2011). Pyroclastic volcanism on Mercury: An explosive past. Planetary and Space Science, 59(15), 1895–1909.

32. Klima, R. L., Denevi, B. W., Ernst, C. M., et al. (2018). Low-reflectance material and its implications for Mercury's crust: Evidence for carbon. Geophysical Research Letters, 45(7), 2945–2953.
33. Krot, A. N., Scott, E. R. D., & Zolensky, M. E. (2001). High-temperature components in chondritic meteorites. Meteoritics & Planetary Science, 36(9), 1189–1216.
34. Landi A.I.,Gaft M., Carli C., Insights into the mineralogy of the Rantila aubrite: A luminescence and VNIR reflectance spectroscopy study, Icarus (2025), https://doi.org/10.1016/j.icarus.2025.116725
35. Le Feuvre, M., & Wieczorek, M. A. (2011). Nonuniform cratering of the Moon and a revised crater chronology of the inner Solar System. Icarus, 214(1), 1–20.
36. Lewis, J. S. (1972). Metal/silicate fractionation in the solar system. Earth and Planetary Science Letters, 15(3), 286–290.
37. Lewis, J. S. (1974). The role of giant impacts in the evolution of Mercury. Science, 186(4167), 440–443.
38. Lucchetti, A., Besse, S., Rothery, D. A., Pajola, M., Zambon, F., Galluzzi, V., ... & Cremonese, G. (2021). A geological and spectral study of the Tyagaraja crater on Mercury: Hollow and pyroclastic deposit relationships. *Icarus, 355*, 114111.
39. Lucchetti, A., Cremonese, G., Galluzzi, V., Rothery, D. A., Massironi, M., Guzzetta, L., ... & Palumbo, P. (2018). Mercury hollows as remnants of original bedrock materials and devolatilization processes: A spectral clustering and geomorphological analysis. Journal of Geophysical Research: Planets, 123(9), 2365–2379.
40. Marchi, S., Chapman, C. R., Fassett, C. I., et al. (2013). Global resurfacing of Mercury 3.9–3.6 Ga by heavy bombardment and volcanic activity. Nature, 499(7456), 59–61.
41. Margot, J. L., Peale, S. J., Solomon, S. C., Hauck, S. A., Ghigo, F. D., Jurgens, R. F., ... & Giorgini, J. D. (2007). Large longitude libration of Mercury reveals a molten core. Science, 316(5825), 710–714.
42. McCoy, T. J., & Nittler, L. R. (2014). Mercury. In H. D. Holland & K. K. Turekian (Eds.), Treatise on Geochemistry (2nd ed., Vol. 2, pp. 119–142). Elsevier.
43. McCubbin, F. M., Boyce, J. W., Gillis-Davis, J. J., Vander Kaaden, K. E., Tartèse, R., & McCoy, T. J. (2012). Is Mercury volatile-rich? *Geophysical Research Letters, 39*(9), L09202. https://doi.org/10.1029/2012GL051711.
44. Morgan, J. W., & Anders, E. (1980). Chemical composition of Earth, Venus and Mercury. Proceedings of the National Academy of Sciences, 77(12), 6973–6977.
45. Murray, B. C. (1975). Surface geology of Mercury: A post-Mariner 10 view. Icarus, 25(3), 315–326.
46. Neukum, G., Ivanov, B. A., & Hartmann, W. K. (2001). Cratering records in the inner solar system in relation to the lunar reference system. Space Science Reviews, 96(1), 55–86.
47. Pajola, M., Lucchetti, A., Cremonese, G., Ferranti, L., Penasa, L., Massironi, M., ... & Zambon, F. (2021). Hollow and pyroclastic deposit relationship inside Lermontov crater on Mercury. *Planetary and Space Science, 204*, 105275. https://doi.org/10.1016/j.pss.2021.105275.
48. Peplowski, P. N., Evans, L. G., Hauck, S. A., et al. (2011). Radioactive elements on Mercury's surface from MESSENGER: Implications for the planet's formation and evolution. Science, 333(6051), 1850–1852.

49. Phillips, M. S., Ernst, C. M., Blewett, D. T., et al. (2021). The lifecycle of hollows on Mercury: An evaluation of candidate volatile phases and a novel model of formation. Icarus, 359, 114306.
50. Scott, E. R. D. (1988). Chondrites and the bulk composition of Mercury. In F. Vilas, C. R. Chapman, & M. S. Matthews (Eds.), Mercury (pp. 712–725). University of Arizona Press.
51. Smith, D. E., Zuber, M. T., Phillips, R. J., et al. (2012). Gravity field and internal structure of Mercury from MESSENGER. Science, 336(6078), 214–217.
52. Solomon, S. C., McNutt, R. L., Gold, R. E., & Domingue, D. L. (2001). The MESSENGER mission to Mercury: Scientific objectives and implementation. Planetary and Space Science, 49(14–15), 1445–1465.
53. Stockstill-Cahill, K. R., McCoy, T. J., Blewett, D. T., et al. (2012). Compositional constraints on Mercury's crust derived from MESSENGER data. Journal of Geophysical Research: Planets, 117(E12).
54. Strom, R. G., & Sprague, A. L. (2003). Exploring Mercury: The iron planet. Springer.
55. Taylor, G. J., & Scott, E. R. D. (2023). Mercury's origin revisited: Planetary differentiation and volatile inventories. Annual Review of Earth and Planetary Sciences, 51, 137–160.
56. Thomas, R. J., Rothery, D. A., Conway, S. J., Anand, M., & Balme, M. R. (2014). Hollows on Mercury: Materials and mechanisms involved in their formation. Icarus, 229, 221–235.
57. Vander Kaaden, K. E., & McCubbin, F. M. (2015). Exotic crust formation on Mercury: Consequences of a graphite flotation crust and FeS exsolution. Journal of Geophysical Research: Planets, 120(11), 1956–1974.
58. Vilas, F., Keller, J. M., Lucey, P. G., Denevi, B. W., & Blewett, D. T. (2016). Mineralogical indicators of Mercury's hollows composition in MESSENGER color observations. Geophysical Research Letters, 43(3), 1450–1456.
59. Wang, Y., Blewett, D. T., Denevi, B. W., Jozwiak, L. M., Ernst, C. M., & Klimczak, C. (2020). Lost volatiles during the formation of hollows on Mercury. Journal of Geophysical Research: Planets, 125(9), e2020JE006559.
60. Wasson, J. T. (1988). The building stones of planets: Mercury and enstatite chondrites. In F. Vilas, C. R. Chapman, & M. S. Matthews (Eds.), Mercury (pp. 622–650). University of Arizona Press.
61. Watters, T. R., Solomon, S. C., Robinson, M. S., et al. (2009). The tectonics of Mercury: Insights into lithospheric evolution. Earth and Planetary Science Letters, 285(3–4), 283–296.
62. Weider, S. Z., Nittler, L. R., Starr, R. D., et al. (2016). Evidence for geochemical terranes on Mercury: Global mapping of major elements with MESSENGER's X-Ray Spectrometer. Geophysical Research Letters, 43(8), 3652–3660.
63. Weisberg, M. K., Prinz, M., & Nehru, C. E. (1993). Petrology and origin of Bencubbin-like (CB) chondrites. Geochimica et Cosmochimica Acta, 57(7), 1567–1586.
64. Weisberg, M. K., Prinz, M., Clayton, R. N., & Mayeda, T. K. (1995). The CR chondrite Renazzo: Multiple parent bodies. Geochimica et Cosmochimica Acta, 59(4), 1567–1586.
65. Wetherill, G. W. (1988). Accumulation of Mercury and the other terrestrial planets. In F. Vilas, C. R. Chapman, & M. S. Matthews (Eds.), Mercury (pp. 670–691). University of Arizona Press.

66. Xiao, Z., Strom, R. G., Blewett, D. T., Byrne, P. K., Murchie, S. L., Denevi, B. W., ... & Solomon, S. C. (2013). Dark spots on Mercury: A distinctive low-reflectance material and its relation to hollows. Journal of Geophysical Research: Planets, 118(9), 1752–1765. https://doi.org/10.1002/jgre.20115.